Computational Depth-resolved Imaging and Metrology

Mengqi Du

2021

Computational Depth-resolved Imaging and Metrology

Mengqi Du

Computational Depth-resolved Imaging and Metrology

Printed by ProefschriftMaken

Ph.D. thesis Vrije Universiteit van Amsterdam, 2021
Computational Depth-resolved Optical Imaging and Metrology
Mengqi Du

ISBN: 978-94-92323-53-8
A digital version of this thesis is available at: https://research.vu.nl/

Cover design: The front cover shows a collection of raw data (diffraction patterns and interferograms) used to obtain image reconstructions presented in this thesis. The back cover shows a ptychographic reconstruction of a finger print.

VRIJE UNIVERSITEIT

Computational Depth-resolved Imaging and Metrology

ACADEMISCH PROEFSCHRIFT

ter verkrijging van de graad Doctor of Philosophy
aan de Vrije Universiteit Amsterdam,
op gezag van de rector magnificus
prof.dr. V. Subramaniam,
in het openbaar te verdedigen
ten overstaan van de promotiecommissie
van de Faculteit der Bètawetenschappen
op woensdag 9 juni 2021 om 9.45 uur
in de aula van de universiteit,
De Boelelaan 1105

door

Mengqi Du

geboren te Hebei, China

promotoren: dr. S.M. Witte
prof.dr. K.S.E. Eikema

This thesis was approved by the members of the reviewing committee:

prof. dr. J.F. de Boer	Vrije Universiteit Amsterdam
prof. dr. A.F. Koenderink	Universiteit van Amsterdam
prof. dr. O. Cohen	Israel Institute of Technology
dr. L. Amitonova	Vrije Universiteit Amsterdam
dr. S.F. Pereira	Technische Universiteit Delft

The work described in this thesis was carried out at the Advanced Research Center for Nanolithography (ARCNL), a public-private partnership between the University of Amsterdam (UvA), Vrije Universiteit Amsterdam (VU Amsterdam), the Netherlands Organisation for Scientific Research (NWO), and the semiconductor equipment manufacturer ASML.

CONTENTS

1 INTRODUCTION 1
1.1 Microscopy and computational imaging . . . 1
1.2 Outline of the thesis . . . 3
2 PTYCHOGRAPHY AND OPTICAL COHERENCE TOMOGRAPHY 5
2.1 Scalar wave propagation . . . 6
2.1.1 Angular spectrum propagation . . . 6
2.1.2 Fresnel and Fraunhofer propagation . . . 7
2.1.3 Practical considerations . . . 10
2.1.4 Lens transformation . . . 11
2.2 The phase problem . . . 13
2.2.1 Holography . . . 13
2.2.2 Coherent diffractive imaging . . . 14
2.3 Ptychography . . . 17
2.3.1 The forward model . . . 18
2.3.2 PIE family algorithms . . . 19
2.3.3 Update rules . . . 21
2.3.4 Adapted forward model for samples on transparent substrates in reflection ptychography . . . 23
2.4 Optical coherence tomography . . . 25
2.4.1 Depth sectioning in OCT . . . 26

I 3D COMPUTATIONAL IMAGING

3 COMPUTATIONAL-IMAGING-BASED OPTICAL COHERENCE TOMOGRAPHY IN TIME- AND FREQUENCY-DOMAIN 31
3.1 Computational imaging in optical coherence tomography . . . 32
3.2 Principles of computational OCT . . . 33
3.2.1 Computational TDOCT . . . 33
3.2.2 Computational SSOCT . . . 35
3.3 Experimental setups and performance characterization . . . 35
3.3.1 Setup . . . 35
3.3.2 Transverse resolution . . . 37
3.3.3 Axial resolution . . . 38
3.4 Experimental results on computational 3D imaging . . . 40
3.5 Inverse scattering point of view of OCT . . . 44
4 PTYCHOGRAPHIC OPTICAL COHERENCE TOMOGRAPHY 49
4.1 Introduction . . . 50
4.2 Experiment and methods . . . 51
4.3 Results and Discussion . . . 53
4.3.1 Two-layer sample reconstruction . . . 53
4.3.2 Mouse brain sample reconstruction . . . 57
4.4 Conclusion . . . 61
5 TOWARDS 3D PTYCHOGRAPHY 63
5.1 Ewald's sphere . . . 64

5.2 First Born approximation . . . 67
5.3 The 3D forward model . . . 68
5.4 Simulation results . . . 70

II COMPUTATIONAL-IMAGING-BASED METROLOGY

6 MEASURING LASER BEAM QUALITY, WAVEFRONTS, AND LENS ABERRATIONS USING PTYCHOGRAPHY 75
6.1 Introduction . . . 76
6.2 Quantitative laser beam quality characterization . . . 77
6.2.1 Wigner distribution and beam matrix . . . 77
6.2.2 Beam propagation ratio M^2 . . . 80
6.2.3 General calculation for BPR and IAF . . . 81
6.2.4 Zernike decomposition of aberrated wavefronts and transmission functions . . . 83
6.2.5 Experimental setup . . . 84
6.3 Results . . . 85
6.3.1 Spectrally-resolved beam parameters (BPR and IAF) . . . 85
6.3.2 Characterization of aberrated wavefronts . . . 86
6.3.3 Aberration characterization of a microlens array . . . 89
6.4 Discussion . . . 90
6.5 Conclusion . . . 91
7 CHARACTERIZATION OF ROUGH SURFACES 93
7.1 Introduction . . . 94
7.2 Surface roughness parameters . . . 95
7.3 Rough surface characterization using computational imaging techniques . . . 95
7.3.1 Rough surface imaging using ptychography . . . 96
7.3.2 Computational OCT for rough surfaces . . . 98
7.4 Polychromatic speckle contrast . . . 99
7.4.1 Speckle contrast . . . 99
7.4.2 Preliminary results on speckle contrast measurement . . . 101

III APPENDIX

H APPENDIX 109
H.1 Lens transformation . . . 109
H.2 Practical considerations for ptychography . . . 111
H.3 Sample fabrication . . . 113
H.4 Tilt correction . . . 115

BIBLIOGRAPHY 117
LIST OF PUBLICATIONS 131
SUMMARY 133
SAMENVATTING 135
ACKNOWLEDGMENTS 139

1

INTRODUCTION

1.1 MICROSCOPY AND COMPUTATIONAL IMAGING

Curiosity has driven people to see beyond what is visible to the naked eye. From the invention of single-lens magnifying glasses to compound optical microscopes, the door to the microscopic world has been knocked open. Ever since, the development of imaging techniques have advanced people's understanding in life and materials science.

As pointed out by Ernst Abbe in 1873 [1], due to diffraction effects, the lateral resolution limit for a microscope is given by $\Delta x = \frac{\lambda}{2\mathrm{NA}}$, and the axial resolution limit is given by $\Delta z = \frac{2\lambda}{\mathrm{NA}^2}$. In these expressions, λ is the wavelength of light and $\mathrm{NA} = n \sin\theta$ is called the numerical aperture, where n is the refractive index of the imaging medium and θ is the maximum scattering angle. Thus, one way to achieve a high imaging resolution in all three dimensions is to increase the NA. Modern optics have achieved an NA value of above 1.5 using high-refractive-index immersion oils. This pushes the resolving power of an optical microscope down to 100-200 nm in the lateral dimension and 500-600 nm in the axial dimension. Given by the diffraction limit, the axial resolution is always lower than the lateral resolution. In the late 1980s and beginning 1990s, a 3D image modality called optical coherence tomography (OCT) [2, 3] was developed, which successfully decouples the lateral and axial imaging resolution by taking advantage of short temporal coherence of broadband light sources. OCT has been a prominent micrometer-scale 3D imaging technique with successful clinical applications in for example ophthalmology, dermatology, and angiography [4–7]. In the past five decades, super-resolution fluorescence microscopy methods [8–11] have been developed to overcome the diffraction limit, further pushing the 3D imaging resolution to below 50 nm [12–15]. Super-resolution fluorescence microscopy has been applied to image living cells and even living organisms, leading to numerous discoveries in biomedical studies [16–18]. However, an intrinsic disadvantage of these techniques is the requirement of invasive fluorescence labeling, which involves complex sample preparation and measurement control, and introduces the risk of disturbing the imaging samples.

According to the diffraction limit, the other way to improve 3D imaging resolution is to utilize shorter wavelengths. Soft and hard x-rays with a wavelength range from 10 nm down to 0.01 nm potentially allow nanoscale imaging. Moreover, x-rays offer large penetration depth and element-specific imaging. However, compared to visible and near-infrared wavelengths, one of the main difficulties of using shorter wavelengths is the limited availability of high-quality optics. This

has motivated and driven the development of computational imaging techniques. X-ray computed tomography (CT) [19], as an important medical radiography tool, enables cross-sectional image reconstructions from attenuation measurements. In CT, an x-ray beam is scanning over a specimen and due to its absorption variation, a 3D attenuation map can be created combining all measured directions. Commercial CT scanners often provide a 3D resolution of hundreds of micrometers with a centimeter-scale image range. By utilizing diffraction effects, the imaging resolution can be drastically improved as in diffraction tomography [20], which is computationally more demanding than CT. Apart from x-rays, electrons (having a wavelength in the range of picometers) have also been used for imaging applications, and the first electron microscope was developed in 1931. Also due to the lack of high quality lenses, the electron microscopy community sought for computational imaging methods to improve the imaging resolution and reach the diffraction limit [21, 22]. Therefore, diffraction-based measurements appeared, where instead of relying on optics to form an 'equivalent' image of a specimen, diffraction patterns of the specimen are measured from which the specimen is numerically reconstructed. Early diffraction studies started with periodically structured crystals, which produce discrete Bragg peaks in far-field diffraction patterns. X-ray and electron crystallography [23] have been developed to reveal the internal molecular/atomic arrangements of crystals. Later, coherent diffractive imaging (CDI) [24, 25] branched off from crystallography, extending to reconstruction of non-periodic objects from diffraction patterns with continuous features. The main task of CDI is to solve the so-called 'phase problem' [26]. When measuring a diffraction pattern with a camera, only the intensity of the complex electric field is recorded and the phase information is lost. In order to invert the measured data and reconstruct the object, numerical algorithms together with diffraction measurement schemes are developed to perform phase retrieval [24, 27–29]. In the past two decades, benefiting from rapid development of computer technologies, computational imaging techniques have become more powerful and mature. Among various phase retrieval methods, ptychography [30, 31] stands out as it enables simultaneous reconstruction of the illumination probe and the specimen.

Although originally designed for x-ray and electron microscopy, computational imaging techniques turn out to be beneficial in the optical regime as well. Replacing imaging optics by algorithms simplifies the hardware of a microscope, lowers the cost, reduces aberrations and deformations induced by imperfect optics and/or misalignment of optics, and enables diffraction-limited resolution. It has been shown that incorporating computational methods into existing imaging modalities can drastically improve the imaging capability. Fourier ptychographic microscopy [32] solves the tradeoff between resolution and field-of-view of a conventional optical microscope, enabling gigapixel high-resolution color imaging by simply adding a low-cost light-emitting diode matrix module and utilizing computational power. Similarly, the tradeoff between transverse resolution and depth-of-field in conventional OCT has been circumvented by utilizing model-based computational aids [33]. Moreover, computational imaging methods can provide quantitative information of a specimen. Recent work has demonstrated spatially resolved refractive index imaging by combining computational tomog-

raphy with conventional OCT [34]. Also compared to traditional phase-contrast microscopy [35], ptychography offers quantitative phase reconstruction [36, 37].

1.2 OUTLINE OF THE THESIS

In this thesis, we explore the benefits of computational imaging methods in the direction of depth-resolved imaging and rough surface characterization using visible and near-infrared light. More specifically, we start by introducing two existing imaging techniques: OCT and ptychography in Chapter 2, and we lay down the fundamentals of both methods. The rest of the thesis is divided into two parts. The first part aims at depth-resolved imaging, where OCT and ptychography are extended and combined. In Chapter 3, we present a computational OCT system and demonstrate 3D reconstruction with micrometer-scale resolutions. In Chapter 4, we introduce a new optical imaging concept that combines ptychography with OCT, and we demonstrate 3D micrometer-scale resolution with both nanolithographic and biological specimens. In Chapter 5, we work towards 3D ptychography, where simulations are performed on weakly scattering samples. The second part of the thesis investigates computational imaging methods as a metrology tool. In Chapter 6, we show that ptychography can be used as a wavefront sensing tool for beam quality, wavefront and lens aberration characterization. In Chapter 7, we apply computational imaging techniques to study rough surfaces.

2

PTYCHOGRAPHY AND OPTICAL COHERENCE TOMOGRAPHY

ABSTRACT

This chapter introduces two imaging techniques, known as ptychography and optical coherence tomography (OCT). We start with the scalar diffraction theory, where we focus on numerical propagators which serve as indispensable tools for performing computational imaging. The development of coherent diffractive imaging (CDI) is revisited, where we discuss the phase problem, uniqueness of the 2D phase retrieval and the oversampling requirement in conventional CDI. Then, as an unconventional CDI technique, ptychography is introduced. We explain the 2D forward model and algorithms in the ptychographic iterative engine (PIE) family. We also show implementation of an adapted forward model in reflection ptychography with experimental data. Finally, we introduce OCT and explain its depth sectioning principle.

2.1 SCALAR WAVE PROPAGATION

We start from considering a monochromatic scalar electric field at the optical frequency f propagating in a homogeneous and isotropic dielectric medium with a refractive index n. If we drop the time dependence, the complex amplitude of the electric field obeys the Helmholtz equation[1]:

$$(\nabla^2 + k^2)E = 0, \tag{2.1}$$

where $k = \frac{2\pi}{\lambda}$ is the wavenumber, and $\lambda = \frac{c}{nf}$ is the wavelength.

2.1.1 *Angular spectrum propagation*

A 2D Fourier transform decomposes a complex electric field into a collection of plane waves:

$$\tilde{E}(k_x, k_y; z) = \iint_{-\infty}^{\infty} E(x, y, z) e^{-i(k_x x + k_y y)} dx dy, \tag{2.2}$$

where the exponential function $e^{-i(k_x x + k_y y)}$ represents a plane wave with a wavevector $\mathbf{k} = (k_x, k_y, k_z) = (k\cos\alpha, k\cos\beta, k\cos\gamma)$ as shown in Fig. 2.1. The complex amplitude $\tilde{E}(k_x, k_y; z)$ is called the angular spectrum of the field $E(x, y, z)$.

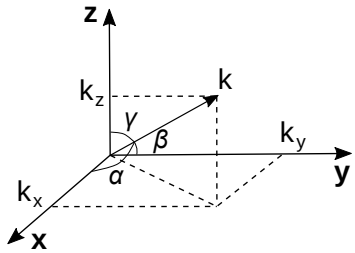

Figure 2.1: A wavevector $\mathbf{k}$.

The field $E(x, y, z)$ can be written as an inverse Fourier transform:

$$E(x, y, z) = \iint_{-\infty}^{\infty} \tilde{E}(k_x, k_y; z) e^{i(k_x x + k_y y)} dk_x dk_y, \tag{2.3}$$

and it must obey the Helmholtz equation. By inserting Eq. 2.3 into the Helmholtz equation (Eq. 2.1) and rearranging, we obtain:

$$\frac{d^2}{dz^2}\tilde{E}(k_x, k_y; z) + (k^2 - k_x^2 - k_y^2)\tilde{E}(k_x, k_y, z) = 0. \tag{2.4}$$

1 see [38] chapter 3 for derivation from Maxwell's equations for vector fields to Helmholtz equation for scalar fields.

An elementary solution for the above equation can be written as:

$$\tilde{E}(k_x, k_y; z) = \tilde{E}(k_x, k_y; 0) e^{iz\sqrt{k^2 - k_x^2 - k_y^2}}, \tag{2.5}$$

where $\tilde{E}(k_x, k_y; 0) = \iint_{-\infty}^{\infty} E(x, y, 0) e^{-i(k_x x + k_y y)} dxdy$ is the angular spectrum of the electric field at $z = 0$ plane. Thus the electric field $E(x, y, z)$ can be reformulated into:

$$E(x, y, z) = \mathcal{F}^{-1}\{\mathcal{F}\{E(x, y, 0)\} H(k_x, k_y, z)\}, \tag{2.6}$$

where $\mathcal{F}$ and $\mathcal{F}^{-1}$ denote forward and inverse 2D Fourier transform, and $H(k_x, k_y, z)$ is the transfer function of the optical system:

$$H(k_x, k_y, z) = e^{iz\sqrt{k^2 - k_x^2 - k_y^2}} = e^{izk_z} \quad (k_z = \sqrt{k^2 - k_x^2 - k_y^2}), \tag{2.7}$$

which is essentially a spherical spatial phase dispersion term as shown in Fig. 2.2(a), where low spatial frequency components experience relatively less phase shift compared to high spatial frequency components. As we often can observe in diffraction experiments, small features defocus faster than big features upon propagation.

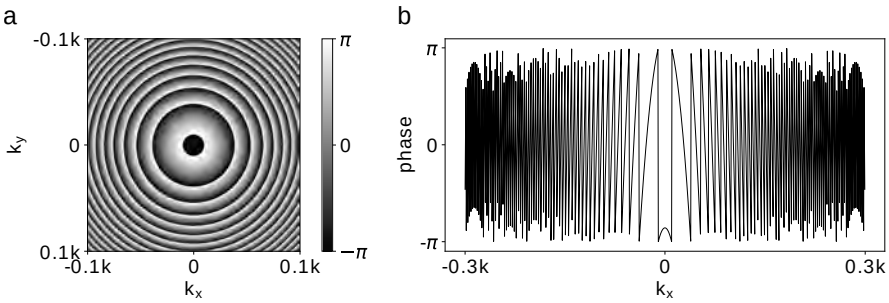

Figure 2.2: Calculated phase of the transfer function using $\lambda = 700\,\text{nm}$ and $z = 1\,\text{mm}$ (a) 2D spherical map. (b) 1D plot at $k_y = 0$, where aliasing can be observed at higher spatial frequencies.

Equation 2.6 is referred to as the angular spectrum propagator (AS propagator) that describes how an electric field propagates from one plane to any other parallel plane over a distance z. The angular spectrum propagation is derived directly from the scalar diffraction theory without approximation (contrary to the Fresnel or Fraunhofer propagation introduced in the following section).

2.1.2 *Fresnel and Fraunhofer propagation*

In this section we introduce Fresnel and Fraunhofer propagators to calculate wave propagation between parallel planes. As shown in Fig. 2.3, $E(x', y', 0)$ is the complex wavefield distribution across the source plane $z = 0$, and after

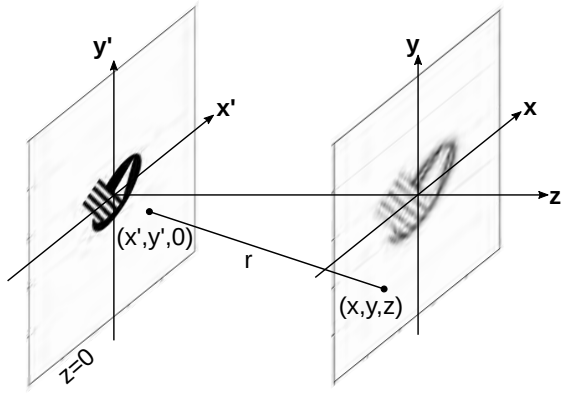

Figure 2.3: Wavefield propagation through parallel planes: z is the propagation direction, (x', y') at $z = 0$ are the source plane coordinates, (x, y) are the parallel plane coordinates after propagation.

propagation $E(x, y, z)$ is the complex wavefield across a parallel observing plane. r is the distance between a source and an observing point:

$$r = \sqrt{(x - x')^2 + (y - y')^2 + z^2} \tag{2.8}$$

By assuming that all distances r are much larger than the wavelength λ:

$$r \gg \lambda, \tag{2.9}$$

the planar wavefield propagation over distance z is described by the Huygens-Fresnel principle[2]:

$$E(x, y, z) = \frac{1}{i\lambda} \iint_{-\infty}^{\infty} E(x', y', 0) \frac{e^{ikr}}{r} cos\theta dx' dy', \tag{2.10}$$

where the observing field is considered as a superposition of spherical waves from secondary sources at the starting plane. θ is the angle between the normal of the source plane and the observation direction. In the case of parallel planes, $cos\theta = \frac{z}{r}$, thus the Huygens-Fresnel principle can be written as:

$$E(x, y, z) = \frac{z}{i\lambda} \iint_{-\infty}^{\infty} E(x', y', 0) \frac{e^{ikr}}{r^2} dx' dy'. \tag{2.11}$$

Below additional approximations are applied to Eq. 2.11 to simplify the calculation, namely the Fresnel approximation and Fraunhofer approximation.

2 see [38] chapter 3 for details of the Huygens-Fresnel principle.

The Fresnel approximation

The Fresnel approximation, which is equivalent to the paraxial approximation, replaces the spherical waves by quadratic waves in Eq. 2.11 by applying binomial expansions to the distance r:

$$\begin{aligned} r &= z\sqrt{1+(\frac{x-x^{'}}{z})^2+(\frac{y-y^{'}}{z})^2} \\ &\approx z[1+\frac{1}{2}(\frac{x-x^{'}}{z})^2+\frac{1}{2}(\frac{y-y^{'}}{z})^2]. \end{aligned} \tag{2.12}$$

Using this approximation, Eq. 2.11 becomes:

$$E(x,y,z) = \frac{e^{ikz}}{i\lambda z}\iint_{-\infty}^{\infty} E(x^{'},y^{'},0)e^{i\frac{k}{2z}[(x-x^{'})^2+(y-y^{'})^2]}dx^{'}dy^{'}. \tag{2.13}$$

There are two approaches to rearrange Eq. 2.13:

- Approach 1: Fresnel diffraction integral

$$\begin{aligned} E(x,y,z) =& \frac{e^{ikz}}{i\lambda z}e^{i\frac{k}{2z}(x^2+y^2)} \\ & \iint_{-\infty}^{\infty}\{E(x^{'},y^{'},0)e^{i\frac{k}{2z}(x^{'2}+y^{'2})}\}e^{-i\frac{k}{z}(xx^{'}+yy^{'})}dx^{'}dy^{'} \end{aligned} \tag{2.14}$$

The integral can be seen as a Fourier transform of the product between the source field and a quadratic phase term evaluated at frequencies:

$$k_x = k\frac{x}{z},\quad k_y = k\frac{y}{z}. \tag{2.15}$$

Equation 2.14 is referred to as the Fresnel integral propagator in this thesis.

- Approach 2: Fresnel convolution

$$E(x,y,z) = \iint_{-\infty}^{\infty} E(x^{'},y^{'},0)h(x-x^{'},y-y^{'},z)dx^{'}dy^{'} \tag{2.16}$$

$$= \mathcal{F}^{-1}\{\mathcal{F}\{E(x^{'},y^{'},0)\mathcal{F}\{h(x,y,z)\}\}\}, \tag{2.17}$$

where:

$$h(x,y,z) = \frac{e^{ikz}}{i\lambda z}e^{i\frac{k}{2z}(x^2+y^2)}, \tag{2.18}$$

and its Fourier transform is:

$$H(k_x,k_y,z) = e^{ikz}e^{-i\frac{z}{2k}(k_x^2+k_y^2)}. \tag{2.19}$$

This is the transfer function for Fresnel diffraction. It can also be obtained by applying the Fresnel approximation directly onto the transfer function of the angular spectrum propagation (see Eq. 2.7), where the spherical spatial phase dispersion e^{izk_z} is approximated by a quadratic phase dispersion $e^{-i\frac{z}{2k}(k_x^2+k_y^2)}$ times a global phase delay e^{ikz} through the transformation below:

$$k_z = k\sqrt{1-(\frac{k_x}{k})^2-(\frac{k_y}{k})^2} \approx k[1-\frac{1}{2}(\frac{k_x}{k})^2-\frac{1}{2}(\frac{k_y}{k})^2]. \tag{2.20}$$

The $\max(\frac{k_x}{k})$ and $\max(\frac{k_y}{k})$ represents the numerical aperture (NA) of the system in two directions. As mentioned before, the Fresnel approximation is equivalent to the paraxial approximation (small-angle approximation), here we can see that Eq. 2.20 is only valid if $\frac{k_x}{k}$ and $\frac{k_y}{k}$ are both much smaller than 1. Equation 2.16 is referred to as the Fresnel Convolution propagator in this thesis.

Fraunhofer approximation

The Fraunhofer approximation is a special case of the Fresnel approximation. When the distance z is large enough such that the quadratic phase term $e^{i\frac{k}{2z}(x'^2+y'^2)}$ in the Fresnel integral Eq. 2.14 can be approximated as flat over the object area:

$$\frac{k}{2z}(x'^2+y'^2) = \frac{\pi}{\lambda z}(x'^2+y'^2) << 1, \tag{2.21}$$

then we arrive at the far-field Fraunhofer diffraction formula:

$$E(x,y,z) = \frac{e^{ikz}}{i\lambda z} e^{i\frac{k}{2z}(x^2+y^2)} \iint_{-\infty}^{\infty} \{E(x',y',0)\} e^{-i\frac{k}{z}(xx'+yy')} dx'dy', \tag{2.22}$$

which is a phase factor times a direct Fourier transform of the source field with the corresponding frequencies:

$$k_x = k\frac{x}{z}, \quad k_y = k\frac{y}{z}. \tag{2.23}$$

Equation 2.22 is referred to as the Fraunhofer propagator in this thesis.

2.1.3 *Practical considerations*

We have introduced four propagators for numerical propagation, i.e. the AS propagator (Eq. 2.6), Fresnel integral propagator (Eq. 2.14), Fresnel convolution propagator (Eq 2.16), and Fraunhofer propagator (Eq. 2.22). Here we compare different propagators and address practical issues when using them.

Accuracy

The AS propagator is directly derived from the scalar diffraction theory without additional approximations. In principle, it should be suitable for general propagation cases with different propagation distances or diffraction regimes (near- or far-field). However, numerical errors may arise from ill-sampling of the transfer function. As shown in Fig. 2.2(b), the oscillation frequency of the phase of the transfer function (Eq. 2.7) increases as a function of the angular spatial frequency k_x, and the propagation distance z. When the oscillation is faster than the sampling rate, aliasing errors appear. We adopt the solution proposed in [39] to solve this problem by using band-limited transfer functions. Firstly, we calculate the local frequency of the oscillation:

$$f_{k_x} = \frac{\partial\phi}{\partial k_x} = \frac{k_x z}{\sqrt{k^2-k_x^2-k_y^2}}, \qquad f_{k_y} = \frac{\partial\phi}{\partial k_y} = \frac{k_y z}{\sqrt{k^2-k_x^2-k_y^2}}. \tag{2.24}$$

Then according to the Nyquist theorem, the sampling interval should be smaller than half the oscillation period:

$$\Delta k_x \leq |\frac{1}{2f_{k_x}}|, \qquad \Delta k_y \leq |\frac{1}{2f_{k_y}}|. \tag{2.25}$$

From this, we can calculate the cut-off frequencies in both directions:

$$|k_x| \leq \sqrt{\frac{k^2 - k_y^2}{1 + 4(\Delta k_x)^2 z^2}}, \quad |k_y| \leq \sqrt{\frac{k^2 - k_x^2}{1 + 4(\Delta k_y)^2 z^2}}, \tag{2.26}$$

The values of the transfer function above the cut-off frequencies are set to zero. The AS propagator used in the rest of this thesis is referred to as the band-limited angular spectrum propagator. Since the Fresnel convolution propagator is a special case of the AS propagator, a similar band-limit approach can be used in the transfer function to avoid aliasing problems.

Efficiency

The AS and Fresnel Convolution propagators both require two times 2D Fourier transforms, while the Fresnel integral and Fraunhofer propagators only require a single 2D Fourier transform, which are more advantageous in terms of calculation efficiency and speed.

Sampling

In the AS and Fresnel Convolution propagators, the sampling window and intervals remain the same upon propagation. More specifically, they do not depend on the wavelength or the propagation distance. In contrast, for the Fresnel integral and Fraunhofer propagators, the sampling window and intervals are a function of wavelength and propagation distance as shown in Eq. 2.15 and in Eq. 2.23 respectively. In practice, a 2D detector is often used to sample a wavefield. When using the AS or Fresnel Convolution propagators, the lower bound of the imaging resolution is mainly determined by the camera pixel size. However, in the Fresnel integral and Fraunhofer propagators, the camera pixel size is not necessarily a limitation, and the imaging resolution can be smaller than the pixel size by tuning the propagation distance.

In this thesis, we only discuss propagation between parallel planes. For non-parallel planes, readers are referred to [40–42].

2.1.4 *Lens transformation*

In the previous sections we have shown how wavefields propagate in free space. We now proceed to discuss how wavefields propagate through lenses. We start with the phase transformation of a thin lens in the paraxial approximation [38]:

$$t_l(x, y) = e^{ikn\Delta_0} e^{-i\frac{k}{2f}(x^2+y^2)}, \tag{2.27}$$

where $k = \frac{2\pi}{\lambda}$ is the wavenumber, n is the refractive index, Δ_0 is the maximum thickness of the lens, and f is the focal length, which is defined by

$$f = \frac{1}{(n-1)(\frac{1}{R_1} - \frac{1}{R_2})}, \tag{2.28}$$

where R_1 and R_2 are the radii of curvature of the front and the back surface of the lens. Within the paraxial approximation, spherical aberration is induced by applying a quadratic approximation to a spherical surface curvature. In practice, the aberration can be corrected by making the surface of lenses aspherical.

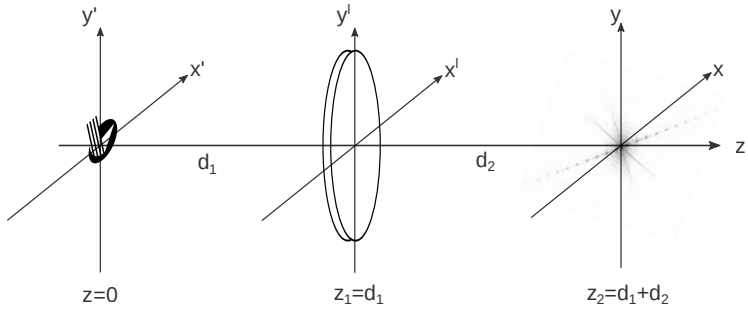

Figure 2.4: Wavefield propagation through parallel planes: z is the propagation direction, (x', y') at $z = 0$ are the source plane coordinates, (x, y) are the parallel plane coordinates after propagation.

Consider the situation shown in Fig. 2.4, in which an object, represented by $E(x', y', 0)$, is placed in front of a lens at a distance d_1, and a detector is behind the lens at a distance d_2. To find the field distribution at the detector plane $E(x, y, z_2)$, we first calculate the field distribution $E_{l1}(x^l, y^l, z_1)$ at the front plane of the lens using the Fresnel integral propagator, then we calculate the field distribution at the back plane of the lens by applying the lens transformation (Eq. 2.27), thus $E_{l2}(x^l, y^l, z_1) = E_{l1}(x^l, y^l, z_1)t_l(x^l, y^l)$. Finally, we propagate $E_{l2}(x^l, y^l, z_1)$ over a distance of d_s to the detector plane to obtain $E(x, y, z_2)$. The derivation is included in Appx. h.1. The final wavefield at the detector plane is expressed as

$$E(x, y, z_2) = A \iint_{-\infty}^{\infty} E(x', y', 0) e^{ikB(x'^2 + y'^2)} e^{\frac{-ikf}{d_1 d_2 - f d_1 - f d_2}(xx' + yy')} dx' dy', \tag{2.29}$$

where A represents a constant phase term that is often neglected, as in many cases only the intensity of a wavefield is of interest. The expression of A can be found in Appx. h.1. B is a factor determined by the distances d_1, d_2, and focal length of the lens f:

$$B = \frac{1}{2d_1} - \frac{f d_2}{2d_1(f d_1 + f d_2 - d_1 d_2)}. \tag{2.30}$$

From this general expression, we find that as long as the detector is placed at the back focal plane of the lens ($d_2 = f$), the factor B becomes 0 and the quadratic phase term $e^{ikB(x'^2 + y'^2)}$ in Eq. 2.29 vanishes. Thus the detector plane directly

becomes the reciprocal plane of the object, where the wavefield at the detector plane is simply a Fourier transform of the object wavefield. In a lensless diffraction geometry, the object and camera distance need to be large enough to be in the far-field regime, which often leads to a very low NA that limits the imaging resolution. The relation given in Eq. 2.29 indicates that a lens can be used to achieve far-field diffraction while maintaining an NA that is determined by the lens.

2.2 THE PHASE PROBLEM

In the previous section (Sec. 2.1), we have discussed how to numerically calculate the propagation of a complex-valued scalar wavefield in free space or through thin lenses. In practice, detectors based on photoelectric effects are often used to measure an electric field, where only the intensity[3] of the electric field can be directly recorded, and the phase information is lost. The term 'the phase problem' originally came from crystallography [23], where the lost phase of the far-field diffraction pattern of a crystal needs to be retrieved in order to invert its 3D structure [43]. The same problem applies for diffraction imaging of non-periodic structures. In fact, regardless of whether a measurement is performed at a diffraction plane or directly at an image plane of an object, half of the wavefield information is lost. For quantitative imaging that aims at obtaining physical quantities of an object, as opposed to contrast-only imaging, solving the phase problem is often equally important. There are generally two main approaches towards imaging complex wavefields, one is holography [44] and the other is coherent diffractive imaging (CDI) [24, 25].

2.2.1 *Holography*

Holography was proposed by Gabor in 1948 [44] as a new lensless imaging principle in electron microscopy. In the original idea of Gabor [44], a weakly scattering object is illuminated by a divergent spherical wave, where the unscattered part functions as a reference that interferes with the scattered part of the wave. The total intensity can be expressed as:

$$I = |O + R|^2 = |O|^2 + |R|^2 + OR^* + O^*R, \tag{2.31}$$

where O and R represent the scattered object field and the reference field respectively. The intensity pattern is regarded as a hologram, which used to be recorded on a photographic film. Once the hologram is generated, an identical copy of the spherical wave is used to illuminate the hologram, resulting in a 3D virtual image of the object behind. By multiplying an identical reference wave to the recorded hologram in Eq. 2.31:

$$RI = R|O|^2 + R|R|^2 + O|R|^2 + O^*RR, \tag{2.32}$$

we can see the object wavefield appears in the third term of Eq. 2.32. Gabor's measurement arrangement later has been referred to as in-line holography, where

3 Note that throughout the paper, the term 'intensity' denotes the optical intensity as it is commonly defined in laser physics, i.e. the detected optical power per unit area.

the object wave and the reference wave propagate colinearly, and all four terms in Eq. 2.32 overlap in the hologram. Phase shifting methods [45, 46] can be used to separate the object term from the rest. Off-axis holography [47] was later introduced, which uses a separate reference at an angle with respect to the object wave. This modification offers direct spatial separation between the object wave and the other terms, and it also relaxes the weak scattering requirement of the object.

Benefiting from the development of computer technology, digital holography became mature in the 1990s [48], where holograms are recorded digitally by a camera, and reconstructions are numerically performed on computers. Until now, digital holography still remains popular as a lensless imaging technique [46, 49]. In the short-wavelength regime, where the generation of a separate reference wave is more challenging, Fourier transform holography (FTH) [50] was developed, in which a reference aperture is placed next to the imaging object to produce a spherical reference wave. The imaging resolution of FTH is limited by the size of the reference aperture, which can be improved by deconvolution methods. A technique called HERALDO (holography with extended reference by autocorrelation linear differential operation) was demonstrated to improve the imaging resolution in FTH using an extended reference and a paired differential operator [51–53]. Despite the development and modifications of the technique, the core of holography is to record the full information of a coherent wavefield, both the amplitude and phase, by interfering it with a known reference wave. This concept has been applied in Chap. 3, combined with broadband illumination for depth-resolved computational imaging.

2.2.2 *Coherent diffractive imaging*

Coherent diffractive imaging (CDI) is a computational imaging technique that reconstructs an object from its diffraction intensity patterns using iterative phase retrieval algorithms. The evolution of CDI techniques has been inseparably related to the development of phase retrieval algorithms. In the early 1970s, Gerchberg and Saxton [22] introduced an algorithm for solving the phase problem of a general object from intensity measurements in both image and diffraction planes. The Gerchberg-Saxton (GS) algorithm is also referred to as the error-reduction algorithm since the defined error function is guaranteed to either decrease or remain constant [22]. The algorithm starts with a random phase guess for the object wave, which is propagated back and forth between the object and the camera plane, and at each plane, the calculated wavefield is updated with the measured intensity. Although the method was initially intended for improving the resolution in electron microscopy, the authors predicted that it is possible to extend it for broader applications such as x-ray crystallography and optical imaging due to its generality.

Further developments were realized in the optics community aimed at imaging space objects, where Fienup modified the error-reduction algorithm and introduced the input-output type of algorithms [27, 54] with improved convergence speed, which also allow errors to go up temporarily to escape local minima. Also other types of algorithms developed in the same period were discussed

and compared by Fienup [27]. However, although simulated results convincingly suggested the success of phase retrieval algorithms, by the end of 1970s it still remained unclear if unique solutions to general 2D Fourier phase problems exist. In the meantime in the x-ray community, Sayre suggested (in 1980) that crystallography may be potentially extended to image non-periodic objects that have continuous diffraction structures instead of discrete Bragg peaks [55]. Finally in 1982, Bates mathematically demonstrated that the 2D Fourier phase problems have unique solutions [26], more specifically he showed that it is possible to reconstruct a localized 2D complex-valued object from its oversampled far-field diffraction pattern. The first proof-of-principle experiment was carried out in the optical regime using a laser in 1988 [56]. Yet, more than a decade later, the first x-ray experimental reconstruction of a non-crystalline object was successfully demonstrated in 1999 [24] reaching an imaging resolution of 75 nm, which drew considerable attention. Ever since, many successful CDI experiments and reconstructions using various radiation sources have followed [25, 28, 57]. Before going further with the development of CDI, we emphasize two important aspects in the conventional CDI methods that followed Bates's original idea: uniqueness and oversampling.

Ambiguities and uniqueness

Bates pointed out that three kinds of inherent ambiguities exist in CDI when only the Fourier modulus of a 2D object is measured [26, 58]:

$$\sqrt{I(u,v)} = F(u,v) = |\mathcal{F}\{f(x,y)\}|^2, \tag{2.33}$$

where $I(u,v)$ is the measured intensity of the diffracted field $F(u,v)$, and $f(x,y)$ is the object wavefield. The absolute position or orientation of the object can not be determined because $f(x-x_0, y-y_0)$ would result in the same diffraction intensity. The complex conjugate or twin image $f^*(-x-x_0, -y-y_0)$ with arbitrary translations would also produce the same diffraction pattern. The third case is the phase ambiguity where the absolute phase of the object can not be determined since $f(x,y)e^{i(\phi(x-x_0,y-y_0)+\phi_c)}$ with a constant phase factor, and/or an arbitrary linear phase ramp would lead to the same diffraction intensity measurements. However, as Bates suggested, these ambiguities are often trivial in imaging applications where the shape of an object is concerned. Thus, phase retrieval methods are considered to provide unique solutions to the phase problem within the tolerance of these inherent ambiguities.

Oversampling

According to the Nyquist-Shannon sampling theorem [59], a localized object is required to guarantee that the far-field diffraction is band-limited, to ensure that it can be properly sampled in a diffraction measurement [26]. In the error reduction algorithm, Gerchberg and Saxton stated that at both the image and the diffraction plane, the Nyquist-Shannon sampling condition needs to be satisfied [22]. However, if only a single diffraction intensity is available, the phase retrieval problem is under-determined by a factor of two [60]: For a 2D N by N image with complex

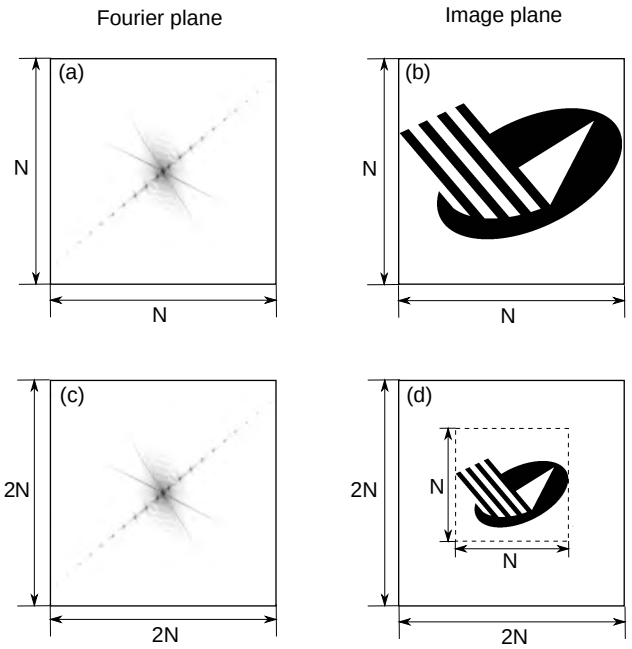

Figure 2.5: Oversampling. (a) A Fourier plane image sampled by N points in each dimension, and (b) the corresponding real space image. (c) A Fourier plane image sampled by 2N points in each dimension, and (d) the corresponding real space image.

values, the total number of unknowns is $2N^2$. From a single diffraction measurement, the total number of equations is N^2. To solve the problem, oversampling becomes necessary [26, 60, 61]. An oversampling factor can be defines as [60]:

$$\sigma = \frac{N_t}{N_u}, \tag{2.34}$$

where N_t is the total pixel number and N_u is the number of unknown-valued pixels. As shown in Fig. 2.5, by oversampling the diffraction pattern in the Reciprocal space, effectively the object in the real space is padded with known pixel values (zeros). When the oversampling factor $\sigma > 2$, the phase problem is not underdetermined anymore and unique solutions should exist.

Fienup's hybrid input-output algorithm [27] (HIO) is one of the most popular phase retrieval algorithms used in CDI, in which waves are numerically propagated back and forth between a diffraction and image plane. At the diffraction plane the Fourier modulus constraint is applied, and at the image plane, various support constraints based on a priori knowledge of the sample can be applied [62–65]. Support constrains essentially decrease the total number of unknowns to help solve the phase problem. However, these unknowns can be sample-specific, and might not be available in every case. A general method that needs no a priori knowledge of the sample is introduced in 2003 [66], which only requires that the

object is sufficiently small to satisfy the oversampling criterion. This method uses a 'shrink-wrap' algorithm to iteratively determine a support constraint together with the object from a diffraction intensity measurement alone.

Another way to solve the phase problem without a priori information is to take multiple diffraction measurements. Originally, CDI measures the diffraction pattern in the far-field, where the relation between the diffracted wave and the object wave is described by a Fourier transform. As can be seen in the Fraunhofer propagator in Eq. 2.22, the intensity measured in the far-field simply scales with the propagation distance. However, in the near-field regime, the diffraction intensity evolves along propagation as can be seen in Eq. 2.14. Thus multiple diffraction intensities in the near-field regime can be measured by translating the detector, and with known propagation distances, the object can be reconstructed successfully [67, 68]. Similarly, since the wavelength and the propagation distance appear as a product in the Fresnel propagator (Eq. 2.14), multiple diffraction patterns measured at different wavelengths in the near-field can deliver the same result under the condition that dispersion effects can be neglected. Using wavelength diversity offers the advantage of avoiding moving part in the setup, which potentially improves the measurement speed [69–72]. In the optical regime, a compact setup consisting of laser diodes and a RGB camera can be used to record multiple diffraction patterns in a single shot, which enables high-speed phase imaging [72]. In addition, wavefront modulation has also been used to generate multiple diffraction patterns in CDI [73, 74].

The shape of the illumination beam plays an important role in CDI. Originally, plane-wave illumination was required to satisfy the Fourier transform relation between the scattered field and directly the object field. A beam stop is necessary to block the unscattered light on the detector. In this configuration, it requires an isolated object to satisfy the Nyquist-Shannon sampling condition. In the 2000s, curved wavefronts were explored for illumination and Fresnel CDI was introduced [75, 76], where it is necessary to recover the illumination in order to obtain quantitative phase information of the object. It has also been shown that structured illumination improves the reconstruction resolution [77]. In 2008, a method called keyhole CDI [28] was introduced, which takes advantage of a localized illumination to release the localization requirement for the object itself in order to satisfy the oversampling requirement. This improvement enabled CDI for extended objects.

We refer the aforementioned CDI methods as conventional CDI. In the following section (Sec. 2.3), a transverse scanning CDI technique called ptychography [31] is introduced. Similar to keyhole CDI, ptychography enables extended object reconstructions by using a localized illumination, which shifts the oversampling requirement from the object to the probe. What also distinguishes ptychography from conventional CDI is that it provides simultaneous quantitative reconstruction of the illumination and the object [78].

2.3 PTYCHOGRAPHY

The concept of ptychography was first introduced in the early 1970's to solve the phase problem in X-ray or electron crystallography [21], which was originally

a non-iterative approach based on convolution theory. With its development, especially in the past two decades, modern ptychography is often referred to as an iterative phase retrieval technique for imaging both periodic and non-periodic objects. In addition, the non-iterative ptychographic method, namely the Wigner distribution deconvolution (WDD), has been revisited recently [79, 80], which provides a deeper understanding of the inversion problem ([31], Sec.17.10). The historic evolution, theories, experimental configurations, various algorithms, and the state of art of ptychography have been summarized by Rodenburg and Maiden [31].

Ptychography scans a localized illumination beam across an object with spatial overlaps, and collects the diffraction pattern at each scan position. With redundant information, ptychographic algorithms are able to deconvolve the illumination from the object and deliver quantitative reconstructions of both [78]. Mathematically, ptychography solves two functions related by a convolution. This concept has been exploited in other variations such as Fourier ptychography [32, 81, 82] and time-domain ptychography [83]. The former synthesizes a high numerical aperture by scanning the illumination angles, which results in a high-resolution image with a large field of view. The latter scans a probe pulse to retrieve a time-varying signal from multiple convolution spectrum measurements.

Compared to conventional CDI methods, ptychography offers a superior alternative for imaging applications using short wavelengths, e.g. EUV, X-ray and electrons [78, 84–87], for which manufacturing of high-quality optics still remains challenging. For imaging with visible or near-infrared lights, ptychography offers label-free, speckle-free, aberration-free, quantitative imaging [36, 37, 88]. Recently, ptychography has also been extended for 3D computational imaging using a multi-slice approach [89, 90], as well as tomographic imaging combined with computed tomography and diffraction tomography [20, 91]. Below we explain the fundamentals of 2D ptychography.

2.3.1 *The forward model*

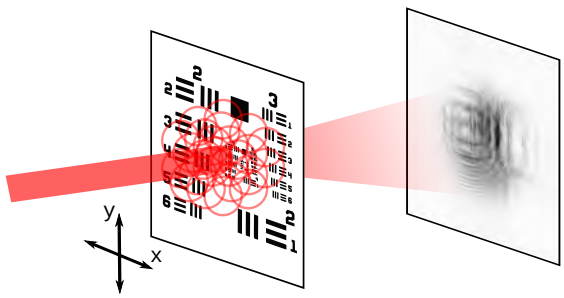

Figure 2.6: Schematic of a transmission ptychography setup. An object is translated with respect to the probe beam. At each position (denoted by circles), a diffraction intensity is recorded.

A schematic of a ptychography setup in a transmission geometry is shown in Fig. 2.6. An incident beam, often referred to as the probe, scans transversely across the object, sequentially illuminating partially overlapping areas. A 2D detector is used to record the diffracted intensities as a function of scan position. An essential assumption in ptychography is that the interaction between the probe and the object can be described by a multiplication:

$$\psi_j(\mathbf{r}) = P(\mathbf{r})O(\mathbf{r} - \mathbf{R}_j), \tag{2.35}$$

where $\mathbf{r}$ is the real-space coordinate, and $\mathbf{R}_j$ is the translation vector (j = 1,2,...N, where N is the amount of scan positions). $P(\mathbf{r})$ represents the complex illumination function, $O(\mathbf{r})$ represents the complex transmission function of an object, and $\psi_j(\mathbf{r})$ is the exit wave. [92]. The multiplicative relation holds for thin objects with a depth extent smaller than the depth of field (DoF) of the imaging system:

$$Z \leq \frac{\lambda}{1 - cos(\theta_{max})}, \tag{2.36}$$

where θ_{max} is the maximum scattering angle captured by the detector. Derivations can be found in the supplementary material of [78]. For thick objects, a multi-slice approach has been introduced to divide the object into thin slices such that each slice satisfies the multiplicative relation [89, 90]. In this thesis, we develop different 3D ptychographic approaches, which are discussed in Chap. 4 and Chap. 5.

Here we continue for the case of a 2D object. The exit wave $\psi_j(\mathbf{r})$ further propagates to the detector plane as:

$$\tilde{\psi}_j(\mathbf{q}) = \mathcal{P}_z\{\psi_j(\mathbf{r})\}. \tag{2.37}$$

The diffracted waves are denoted by $\tilde{\psi}_j(\mathbf{q})$, where $\mathbf{q}$ is the detector coordinate. $\mathcal{P}_z$ represents propagation over distance z. As discussed in Sec. 2.1, depending on the diffraction conditions, different propagators can be chosen for numerical calculations. At the detector plane, only the intensity of the field is recorded:

$$I_j(\mathbf{q}) = |\tilde{\psi}_j(\mathbf{q})|^2 = |\mathcal{P}_z\{\psi_j(\mathbf{r})\}|^2. \tag{2.38}$$

Thus there are two constraints in a ptychography dataset:

- constraint 1: translation constraint in the object plane.
- constraint 2: intensity constraint in the detector plane.

It has been proven that these two constraints in ptychography provide a powerful way to condition the inversion problem, which results in relatively robust reconstruction algorithms [81].

2.3.2 *PIE family algorithms*

Inversion from diffraction intensity measurements is a nonlinear problem. A variety of nonlinear optimization approaches have been successfully applied to ptychography. The first iterative algorithm developed for ptychography is called

the ptychographical iterative engine (PIE) [30], where the object is reconstructed under the condition that the probe is known accurately. Based on the first version of PIE, a modified algorithm that is able to simultaneously reconstruct probe and object has been developed, which is called ePIE (short for extended ptychographic iterative engine) [93]. Later, further improvements have been made by introducing a machine learning concept called 'momentum', which resulted in the mPIE (momentum-accelerated PIE) algorithm [94].

All algorithms in the PIE family follow the same workflow as shown in Fig. 2.7, and the only difference is how the object patch and the probe functions are updated (in yellow boxes). The PIE family is naturally a sequential approach where the object and probe are updated at each scan position j after each update of the exit wave. Comparisons to parallel approaches [78, 95], where the probe and the object functions are updated after a parallel update of all exit waves at all scan positions, have been investigated [31, 96]. In this thesis, we used ePIE and mPIE for experimental data reconstructions.

Figure 2.7 shows the workflow of the PIE family algorithms: we start with an initial guess for the object $O_j(\mathbf{x})$ and probe $P_j(\mathbf{r})$ respectively. Note that the calculation window for the full object is larger than the probe, and each object patch has the same dimensions as the probe. Thus we use different spatial coordinates $\mathbf{x}$ and $\mathbf{r}$ to distinguish a complete object from an object patch. Then we select an object patch $O_j(\mathbf{r})$ often following a random order, and multiply with the probe to form the exit wave $\psi_j(\mathbf{r})$. By using a suitable propagator, the exit wave is numerically propagated to the detector plane, where we apply the intensity constraint:

$$\tilde{\psi}_j^{'}(\mathbf{q}) = \frac{\sqrt{I_j(\mathbf{q})}}{|\tilde{\psi}_j(\mathbf{q})| + \alpha}\tilde{\psi}_j(\mathbf{q}), \tag{2.39}$$

α is a small number to avoid zero divisions. After replacing the amplitude of the diffracted waves by the measured amplitude, we back-propagate to the object plane to form the updated exit wave $\psi_j^{'}(\mathbf{r})$. Up until this step, all the PIE family algorithms are the same. The next step is to update the object patch and the probe, where different approaches are taken in different algorithms (highlighted in yellow in Fig. 2.7). After updating the object patch $O_j^{'}(\mathbf{r})$ and the probe $P_j^{'}(\mathbf{r})$, we update the full object $O_j^{'}(\mathbf{x})$ by inserting the updated object patch. Then we move to the next scan position $j+1$ and repeat the same steps from the top. Once we go through all the scan positions ($j = 1, 2, ..., N$) often in a random order, one full iteration is complete. The error metric is calculated after each iteration to monitor the convergence behavior of the algorithm:

$$Error = \sum_j \frac{\sum_{\mathbf{q}} |I_j(\mathbf{q}) - |\tilde{\psi}_j(\mathbf{q})|^2|}{\sum_{\mathbf{q}} I_j(\mathbf{q})} \tag{2.40}$$

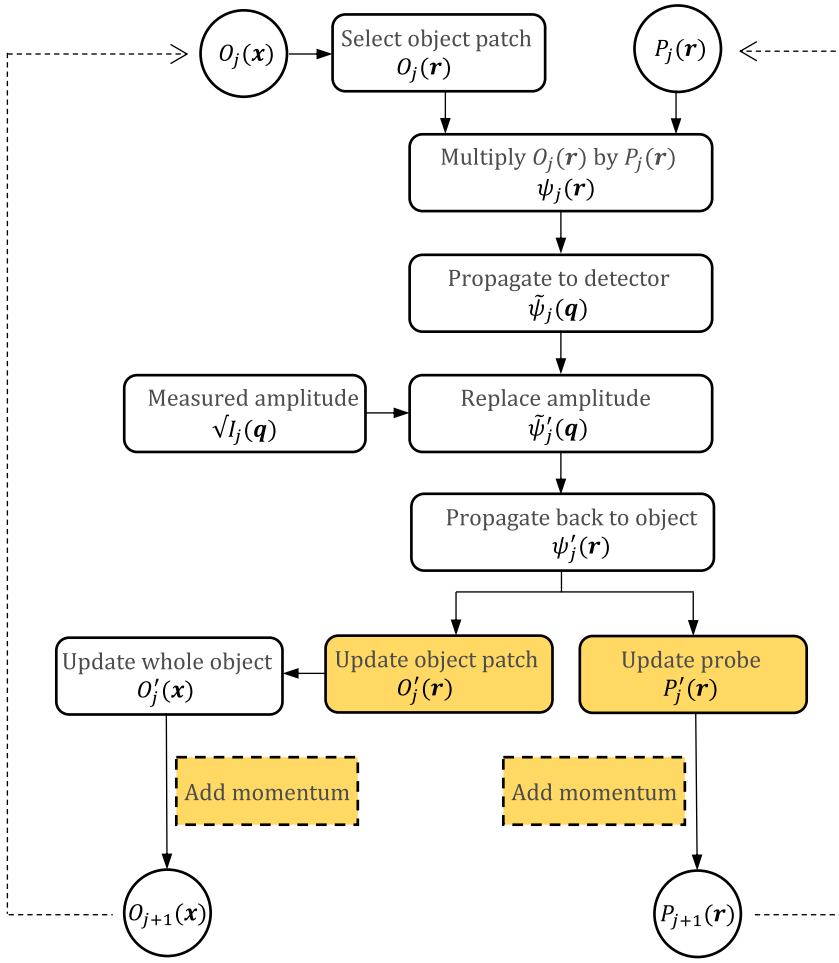

Figure 2.7: Workflow chart of PIE family algorithms (modified from Fig.1 in [94]). The white boxes show common procedures in all algorithms of the PIE family, and the yellow boxes highlight the steps where different approaches are taken in different algorithms. The dashed boxes show momentum-acceleration options. The subscript $j = 1, 2, ..., N$ denotes the scan positions. One full iteration covers all the scan positions.

2.3.3 *Update rules*

Different update rules are used in PIE, ePIE and mPIE. To derive such update functions for the object and the probe from the exit wave, we first write down the cost function:

$$L = |\psi - PO|^2 = (\psi - PO)(\psi^* - P^*O^*). \tag{2.41}$$

To minimize the cost function, the first-order derivative needs to vanish. For a real-valued cost function, we can take the derivative with respect to the complex-conjugate P^* and O^* respectively and set to zeros [97]:

$$\frac{\partial L}{\partial P^*} = 0 \;\rightarrow\; O^*(\psi - PO) = 0 \;\rightarrow\; P_j^{'}(\mathbf{r}) = \frac{O_j^*(\mathbf{r})}{|O_j(\mathbf{r})|^2 + \alpha}\psi_j^{'}(\mathbf{r}), \tag{2.42}$$

$$\frac{\partial L}{\partial O^*} = 0 \;\rightarrow\; P^*(\psi - PO) = 0 \;\rightarrow\; O_j^{'}(\mathbf{r}) = \frac{P_j^*(\mathbf{r})}{|P_j(\mathbf{r})|^2 + \alpha}\psi_j^{'}(\mathbf{r}), \tag{2.43}$$

where α is a small number to avoid zero divisions. Here we can see that P and O appear symmetric, thus they can be simultaneously updated in the same form. However, the update functions in Eq. 2.42 and 2.43 are both unstable. Taking the object update function Eq. 2.43 as an example, it is poorly conditioned in the region where the beam is dim, due to the probe intensity term in the denominator. Thus a spatially varying weighting function can be introduced such that the object update has more effect in the region where the beam is bright [94]:

$$\begin{aligned} O_j^{'}(\mathbf{r}) &= w_j(\mathbf{r})\frac{P_j^*(\mathbf{r})}{|P_j(\mathbf{r})|^2 + \alpha}\psi_j^{'}(\mathbf{r}) + (1 - w_j(\mathbf{r}))O_j(\mathbf{r}) \\ &= O_j(\mathbf{r}) + w_j(\mathbf{r})\frac{P_j^*(\mathbf{r})}{|P_j(\mathbf{r})|^2 + \alpha}(\psi_j^{'}(\mathbf{r}) - \psi_j(\mathbf{r})), \end{aligned} \tag{2.44}$$

where $w_j(\mathbf{r})$ is close to one in the region where the probe intensity is high, and close to zero where it is low.

The PIE algorithm uses the normalized probe amplitude as the weighting function:

$$w_j(\mathbf{r}) = \frac{|P_j(\mathbf{r})|}{max|P_j(\mathbf{r})|}, \tag{2.45}$$

which results in the PIE object update function [30]:

$$O_j^{'}(\mathbf{r}) = O_j(\mathbf{r}) + \beta\frac{|P_j(\mathbf{r})|}{max|P_j(\mathbf{r})|}\frac{P_j^*(\mathbf{r})}{|P_j(\mathbf{r})|^2 + \alpha}(\psi_j^{'}(\mathbf{r}) - \psi_j(\mathbf{r})), \tag{2.46}$$

where $0 < \beta < 1$ is added to control the step size of the object. Originally the probe in the first version of the PIE algorithm is pre-calibrated and not updated [30]. It was realized later that, due to the symmetry of the problem, the priory knowledge requirement of the probe can be removed.

The ePIE algorithm uses the normalized probe intensity as the weighting function:

$$w_j(\mathbf{r}) = \frac{|P_j(\mathbf{r})|^2}{max|P_j(\mathbf{r})|^2}, \tag{2.47}$$

which results in the ePIE object update function [93]:

$$O_j^{'}(\mathbf{r}) = O_j(\mathbf{r}) + \beta\frac{P_j^*(\mathbf{r})}{max|P_j(\mathbf{r})|^2}(\psi_j^{'}(\mathbf{r}) - \psi_j(\mathbf{r})), \tag{2.48}$$

where the small factor α can be waived because the intensity term in the denominator is canceled out.

A further improvement was made in [94] by introducing the concept of 'momentum', which helps to escape local minima. The momentum-acceleration step can be used as an add-on for existing PIE algorithms after the conventional update step for the object and probe as shown in Fig. 2.7. The frequency of applying momentum-acceleration can also be tuned by a parameter, often denoted by T. This implies that after every T position updates, the object is updated by adding a damped momentum term:

$$O_{(j+1)}(\mathbf{x}) = O_j^{'}(\mathbf{x}) + \eta v_j(\mathbf{x}), \tag{2.49}$$

where $0 < \eta < 1$ is called the friction term, and $v_j(\mathbf{x})$ is called the velocity map, which is calculated from:

$$v_j(\mathbf{x}) = \eta v_{j-T}(\mathbf{x}) + (O_j^{'}(\mathbf{x}) - O_{(j-T+1)}(\mathbf{x})) \tag{2.50}$$

where $v_0(\mathbf{x}) = 0$. The momentum-updated object $O_{(j+1)}(\mathbf{x})$ needs to be stored temporarily to calculate the next velocity map. In each algorithm, the probe can be updated in the same way as the object with its own tuning parameters. Figure 2.8 shows an example of the ptychographic reconstruction of a sample slice containing a finger print using the mPIE algorithm.

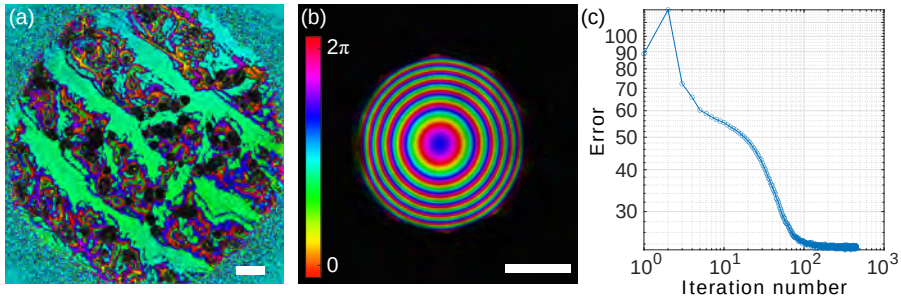

Figure 2.8: Reconstruction results using mPIE: (a) Reconstructed object, a finger print, (b) Reconstructed beam. The scalebars are 200 µm. The colorbar is shared between (a) and (b). The intensity is represented by the brightness and the phase is represented by the color. (c) Error evolution over 450 iterations.

2.3.4 *Adapted forward model for samples on transparent substrates in reflection ptychography*

In reflection ptychography when we measure semi-transparent specimens on glass substrates, the forward model (in Eq. 2.38) needs to be adjusted in order to better describe the scattering events, which in turn improves the reconstruction quality. To demonstrate, we measure a USAF resolution test target (Thorlabs R3L1S4P), which contains bar structures in chrome on a 1.5 mm thick soda lime glass substrate. The schematic of the measurement geometry is shown in Fig. 2.9.

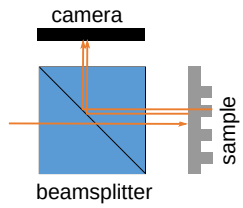

Figure 2.9: A schematic of measurement geometry in reflection ptychography.

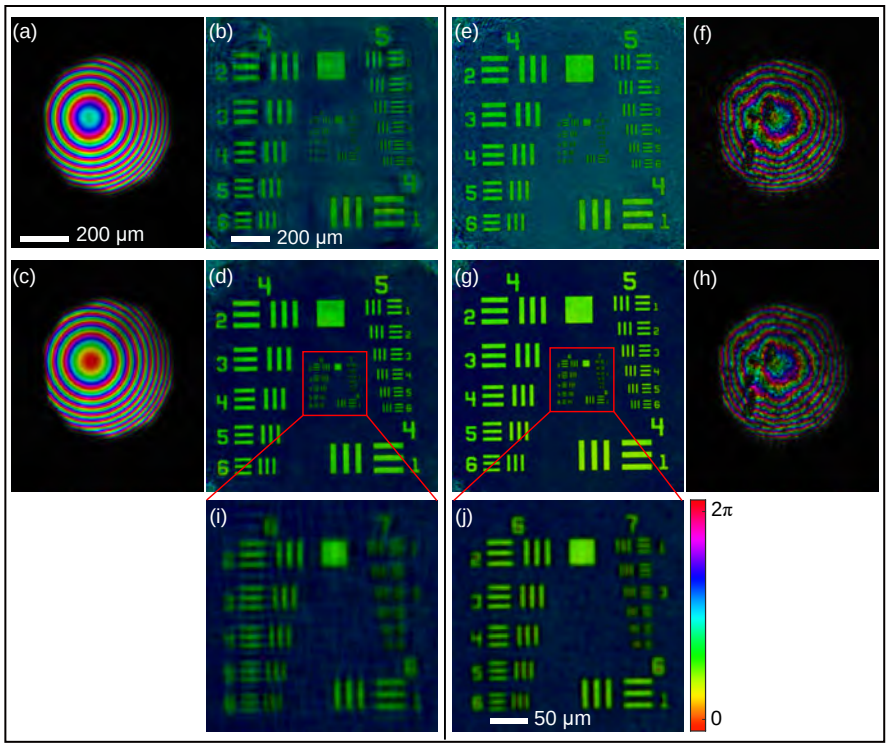

Figure 2.10: A comparison of ptychography reconstructions using the conventional and the adapted forward model. Left two columns are reconstructions of a dataset measured with a smooth beam, and right two columns are with a structured beam. (a,b,e,f) Probe and object reconstructions using the conventional forward model. (c,d,g,h) Probe and object reconstructions using the adapted forward model. The scale bar in (a) is shared among all the probe reconstructions, and the scale bar in (b) is shared among object reconstructions in (b,d,f,g). (i)(j) Zoomed in parts of (f) and (g). The colorbar is shared among all the reconstructions.

Reflections from both sides of the substrate contribute to the diffraction intensity, thus the sample can be considered having two layers. Since the separation of the

two layers is larger than the coherence length of the light, the light reflected from the flat glass air interface can be modeled as a constant signal across all scan positions. The adjusted forward model becomes:

$$\begin{aligned} I_j(\mathbf{q}) &= |\tilde{\psi}_j(\mathbf{q}) + \psi_c(\mathbf{q})|^2. \\ &= |\mathcal{P}_z\{P(\mathbf{r})O(\mathbf{r}-\mathbf{R}_j)\} + \psi_c(\mathbf{q})|^2, \end{aligned} \tag{2.51}$$

where $\psi_c(\mathbf{q})$ represents the constant signal at the camera plane that is reflected from the front flat side of the substrate, and $P(\mathbf{r})$ becomes the probe on the second interface after transmitting through the first one. Two sets of measurements are performed using a smooth and a structured beam respectively[4]. For each measurement, 100 diffraction patterns are recorded with an average overlap factor of 70%. All reconstructions are performed with mPIE [94]. For the dataset measured with a smooth beam, the reconstructed probe and the object using the conventional forward model are shown in Fig. 2.10(a) and (b) respectively. Artefacts can be observed in the object reconstruction (Fig. 2.10(b)), where even big structures appear blurred. Reconstructions using the adjusted forward model are shown in Fig. 2.10(c) and (d), where a clear improvement can be observed and most artefacts are successfully removed. The same conclusion can be drawn for the structured beam dataset, where Fig. 2.10(e) and (f) are reconstructed from the conventional forward model and Fig. 2.10(g) and (h) are from the adjusted model. In addition, comparing Fig. 2.10(i) and (j), we also observed that the structured beam leads to a higher resolution for the object. Intuitively the structured beam provides a higher illumination NA, thus leads to a higher imaging NA (a sum of illumination NA and detection NA). Further studies are necessary to give quantitative explanations.

2.4 OPTICAL COHERENCE TOMOGRAPHY

Optical coherence tomography is a 3D, micrometer-scale, non-invasive optical imaging technique which was first demonstrated in 1991 [2]. It has several notable advantages, including the ability for label-free imaging, background rejection in turbid media through coherence gating, and coherent amplification of weak sample beams from sensitive biological samples. As in all high-resolution volumetric imaging systems, OCT faces the challenge to achieve extended images at sufficiently high acquisition speed, which has led to successful applications in ophthalmology, angiography and other medical fields [4–7].

The principle of optical coherence tomography (OCT) [98] is low coherence interferometry, which measures optical echoes inside a semi-transparent object through interferometric comparison with a reference beam from a broadband light source. Since the first demonstration of point-scanning time-domain OCT (TDOCT) [2], various measurement schemes (summarized in Table 2.1) have been introduced, including full-field TDOCT, point-scanning spectral-domain OCT (SDOCT), point-scanning and full-field swept-source OCT (SSOCT) [98]. Depending on the applications, each variation has its own advantages. Generally, FDOCT offers a higher sensitivity over TDOCT [99–101]. Point scanning

4 Structured beams are created by inserting a piece of scotch tape in the beam path

		Point Scan	Full Field
TDOCT		✓	✓
FDOCT	SDOCT	✓	
	SSOCT	✓	✓

Table 2.1: Variations of OCT.

approaches, compared to full-field techniques, enable better rejection of multiple scattering. Nevertheless, one crucial advantage that all OCT variations share is the decoupling between the transverse and axial resolution, as the axial resolution is determined by the bandwidth of the light source rather than the imaging optics. Below we discuss the depth sectioning principles in OCT.

2.4.1 *Depth sectioning in OCT*

Time-domain OCT

In conventional TDOCT as shown in Fig. 2.11(a), a reference mirror is scanned axially and interferometric intensities are measured as a function of scan delay. The depth distribution is attained by taking the advantage of the low temporal coherence property of broadband light sources. Specifically, interference signals only appear when the optical path length difference between the reference and object is within the coherence length of the light source.

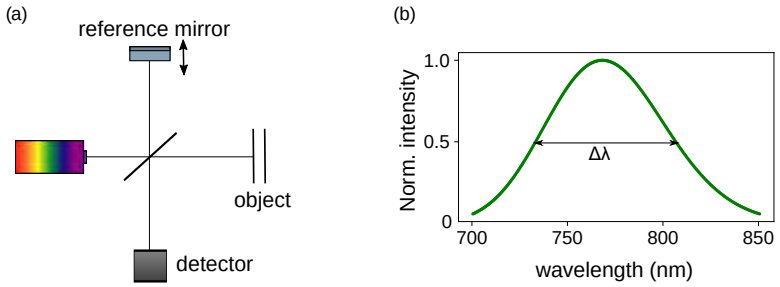

Figure 2.11: (a) Schematic of a simple OCT setup. (b) Simulated spectrum of the broadband light source in (a).

As shown in Fig. 2.11(a), a simulated object contains two flat layers. The simulated Gaussian-shaped spectrum of the light source is presented in Fig. 2.11(b). The total intensity of the back-scattered light from the object and the reference mirror as a function of time delay between them can be expressed in the form:

$$I(t) = \int \mid A_o(\omega)e^{i\varphi_o(\omega)} + A_r(\omega)e^{i(\varphi_r(\omega)+\omega t)} \mid^2 d\omega, \tag{2.52}$$

where $\omega = 2\pi f$ with f the frequency of the light. $A_o(\omega)e^{i\varphi_o(\omega)}$ represents the object wave field and $A_r(\omega)e^{i\varphi_r(\omega)}$ is the reference wave field at the detector plane.

These fields are also functions of the transverse spatial coordinates (x,y), which are omitted for clarity since only flat layers are considered in this analysis. The extra phase term ωt represents the time- and frequency-dependent phase delay between the reference and object signals. At a given time delay, the integration over the spectra results in the total intensity, which is shown in Fig. 2.12.

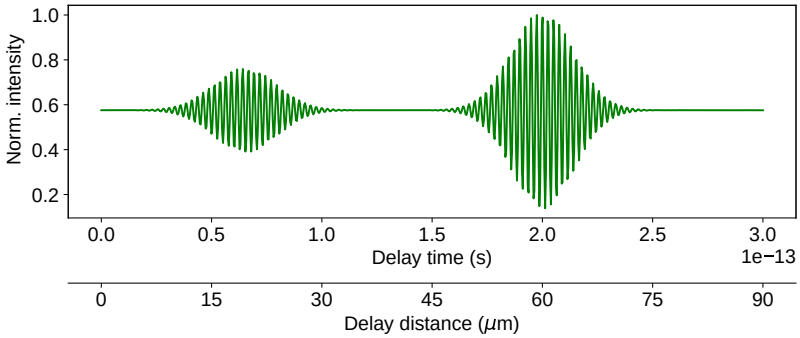

Figure 2.12: Simulated intensity (in TDOCT) as a function of time delay between the reference and object, where the simulated object consists of two layers with different reflection coefficients, which are separated by 20 µm in depth.

The depth separation of the two layers of the simulated object is 20 µm, which results in a 40 µm difference in the optical delay distance (Fig. 2.12) due to a double pass in the reflection geometry. The width of the interference fringes is determined by the coherence length of the light source. For a Gaussian spectrum, the coherence length is given by [102]: $l_c = \frac{4ln2}{\pi}\frac{{\lambda_0}^2}{\Delta\lambda}$, where λ_0 is the central wavelength and $\Delta\lambda$ is the full width at half maximum (FWHM) of the Gaussian spectrum. Taking into account the double pass and the refractive index n of the object, the depth resolution in OCT is given by:

$$\Delta z = \frac{2ln2}{\pi}\frac{{\lambda_0}^2}{n\Delta\lambda} \tag{2.53}$$

In conventional OCT, the final depth response is produced by using a combination of detection schemes and signal processing methods [98], which rejects the DC offset and produces the envelope of the interferometric signal.

SSOCT

SSOCT collects equivalent data as TDOCT with improved speed by avoiding time-delay scans. In SSOCT, the reference mirror remains stationary, and the data acquisition is performed in the frequency domain, as interference signals are recorded as a function of optical wavelength or frequency:

$$I(\omega) = \mid E_o(\omega) + E_r(\omega)e^{-i\omega t_z} \mid^2, \tag{2.54}$$

where $t_z = z/c$ denotes the fixed time delay between the reference and the object, which can be tuned by adjusting the position of the reference mirror. A simulated spectral interference signal is shown in Fig. 2.13(a).

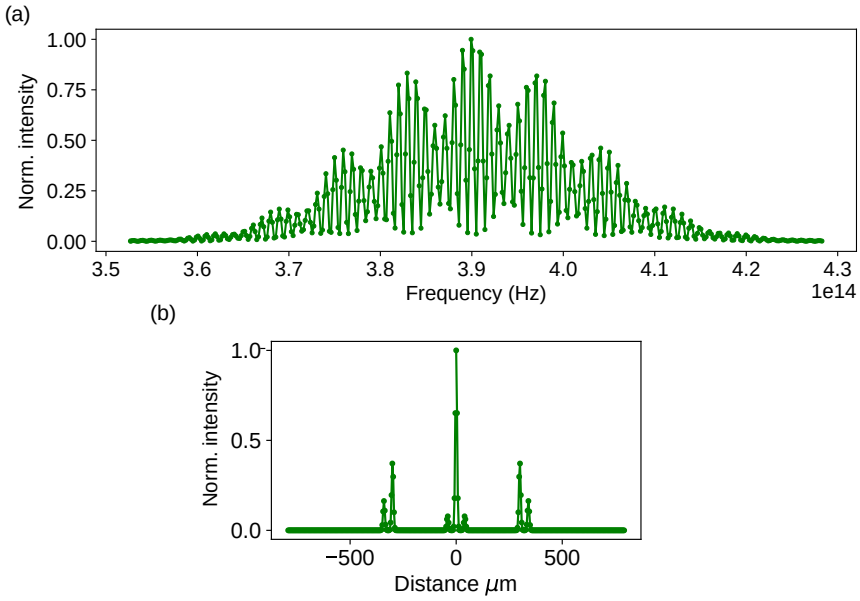

Figure 2.13: (a) Simulated intensity measurement as a function of frequency on a two-layer object in SSOCT. (b) The inverse Fourier transform of the spectral interferogram in (a).

A inverse Fourier transform can be applied to the spectral interference signal (Eq. 2.54) to reveal the depth information. When the spectral signal is not sampled evenly in optical frequency, an interpolation step is necessary. Taking the inverse Fourier transform of Eq. 2.54 results in three terms in the time domain given by the following equation:

$$I(t) = \mathcal{F}_t\{I(\omega)\} = \overline{I}\delta(0) + \mathcal{F}_t\{E_o(\omega)E_r^*(\omega)\} \circledast \delta(t - t_z) + \mathcal{F}_t\{E_o^*(\omega)E_r(\omega)\} \circledast \delta(t + t_z), \tag{2.55}$$

where different depths corresponding to different time delay are separated. As can be seen in Fig. 2.13(b), the two cross-correlation terms are symmetric with respect to the autocorrelation terms in the middle. In principle, the two cross-correlation terms contain the same information. Either one can be chosen as the sample signal, the other one becomes its mirror artefact. A simple way to mitigate autocorrelation and mirror artefacts is to place the reference such that the three terms do not overlap after the Fourier transform, as in our simulated case in Fig. 2.13(b). Then the image signal can be directly selected by numerically filtering the relevant part of the signal. However, this reduces the total depth range to half. In order to obtain the full depth range and to eliminate mirror image artefacts, phase-shifting techniques [103] have been used at a cost of speed. Later, single shot techniques taking advantage of dispersion effects have been developed [104].

Part I

3D COMPUTATIONAL IMAGING

3

COMPUTATIONAL-IMAGING-BASED OPTICAL COHERENCE TOMOGRAPHY IN TIME- AND FREQUENCY-DOMAIN

ABSTRACT

A computational 3D imaging system is developed that enables polychromatic, depth-resolved, diffraction-limited imaging of semi-transparent objects. By combining lensless imaging and optical coherence tomography (OCT), we reconstruct tomographic images of 3D objects from a set of wavelength- and phase-resolved diffraction patterns, using numerical methods to achieve image quality beyond the hardware limits of the optical systems used. We implement both time- and frequency-domain versions of full-field OCT systems, and for both versions we demonstrate fully lensless, as well as high-numerical-aperture configurations. We provide a comparison and overview of these different practical approaches to depth-resolved computational imaging. Furthermore, we demonstrate depth-resolved imaging of multilayer samples with an isotropic resolution in the μm range over a depth range that extends well beyond the depth-of-focus given by the numerical aperture of the imaging system.

A research article based on this chapter has been published as: "Du, M., Eikema, K.S.E & Witte, S. Computational-imaging-based optical coherence tomography in time-and frequency-domain. *OSA Continuum* **2**, 3141-3152 (2019)."

3.1 COMPUTATIONAL IMAGING IN OPTICAL COHERENCE TOMOGRAPHY

Three-dimensional (3D) imaging techniques have provided many new insights in material and life science. For the last half century, the unprecedented development of 3D imaging technologies such as computed tomography, magnetic resonance imaging, and ultrasound imaging has changed our life in various aspects [105]. The development of similar 3D imaging capabilities operating at smaller length scales down to micrometers has also been a subject of considerable attention, as it brings the prospect of non-invasive cellular-level-resolution imaging, which may one day replace the need for invasive biopsies in some medical applications. The main 3D optical technique that has shown the potential to fulfill that promise is optical coherence tomography (OCT), which has drawn considerable attention and is already widely applied in medical sensing and diagnosis [2, 3, 5, 6, 98].

The depth-sectioning principle of OCT has been explained in Sec. 2.4. One fascinating property of OCT is the decoupling between transverse and axial resolution, as the axial resolution is determined by the bandwidth of the light source rather than the imaging optics. However, it is complicated to make full use of this advantage, as the depth-of-field (DoF) of a traditional OCT measurement is still limited by the numerical aperture (NA) of the imaging system, leading to a trade-off between transverse resolution and imaging depth (see Fig. 3.1). Computational post-processing methods have been proposed to correct for the defocus blurring by estimating the point spread function of the OCT system and applying deconvolution algorithms [106–108]. Another approach to mitigate the limited imaging depth is to adopt lensless or computational imaging techniques [109–112], where numerical refocus can be used for different depths inside a thick object. Moreover, the interferometric nature of OCT provides an excellent starting point for computational image reconstruction, as the phase of the light field is directly measured in a holographic scheme.

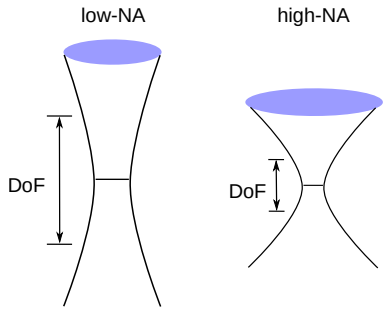

Figure 3.1: The transverse resolution is proportional to the NA of the beam, while the DoF is inversely proportional to NA^2.

This concept of combining holographic methods and broadband illumination to achieve 3D imaging capabilities has been explored by several groups, starting out either from a holography viewpoint [113, 114] or from an OCT-centered approach [115, 116]. In most of these systems, an off-axis holography geometry was employed, which enables rapid extraction of the interferometric term, but at

the expense of field-of-view. One challenge in computational OCT stems from the wavelength-dependence of wave propagation in the Fresnel regime: the different spectral components of a broadband light pulse will therefore each require a different amount of numerical propagation from the detector to achieve a focused image at a specific object depth. In this paper we discuss a set of computational methods for disentangling the information contained in the polychromatic diffraction patterns to retrieve a volumetric image of a 3D object. We introduce and compare methods for time-domain and frequency-domain/swept-source OCT implementations. We then proceed to show these methods experimentally, in both lensless and high-NA configurations. All these variations are combined in one versatile on-axis full-field OCT setup, allowing a direct comparison of the different methods and implementations. With this system, we demonstrate depth-resolved reconstruction of multi-layer samples, with an isotropic resolution at the 2-3 μm level.

3.2 PRINCIPLES OF COMPUTATIONAL OCT

3.2.1 *Computational TDOCT*

In computational TDOCT, we measure interferometric intensities between the diffracted light of the object and the reference. Spatially coherent broadband light sources are required, as the numerical propagation step requires a well-defined spatial phase profile across the object field-of-view. However, each spectral component of the object exit wave propagates differently to the detection plane[38], resulting in a wavelength-dependent interference pattern at the detector plane. The recorded full-field image is then the incoherent sum of all these individual spectral components. In this case, the function of the reference wave is not only that of coherence gating, but also assisting to encode the phase information of the diffracted object field in the interferograms.

For convenience, we expand the interferometric intensity in Eq. 2.52 into:

$$I(t) = \int [\, |\, A_o\, |^2 + |\, A_r\, |^2 + A_o(\omega)A_r^*(\omega)e^{i(\Delta\varphi(\omega)-\omega t)} + A_o^*(\omega)A_r(\omega)e^{-i(\Delta\varphi(\omega)-\omega t)}\,]\, d\omega, \tag{3.1}$$

where $\Delta\varphi(\omega) = \varphi_o(\omega) - \varphi_r(\omega)$ denotes the initial phase difference between the reference and the object signals. In a similar way to Fourier transform spectroscopy[117], a Fourier transform is performed on the intensity signal along the time delay axis,

$$\begin{aligned} I(\omega) &= \mathcal{F}_t\{I(t)\} \\ &= \overline{I}\delta(0) + A_o(\omega)A_r^*(\omega)e^{i\Delta\varphi(\omega)} + A_o^*(-\omega)A_r(-\omega)e^{i\Delta\varphi(-\omega)}. \end{aligned} \tag{3.2}$$

Three terms are obtained in Eq. (3.2): these are the DC term (i.e. at $\omega = 0$), as well as two cross terms at positive and negative frequencies, which are complex conjugates of each other (see in Fig. 3.2(b)). The complex electric field information is contained in these individual cross terms, and a single cross term can be

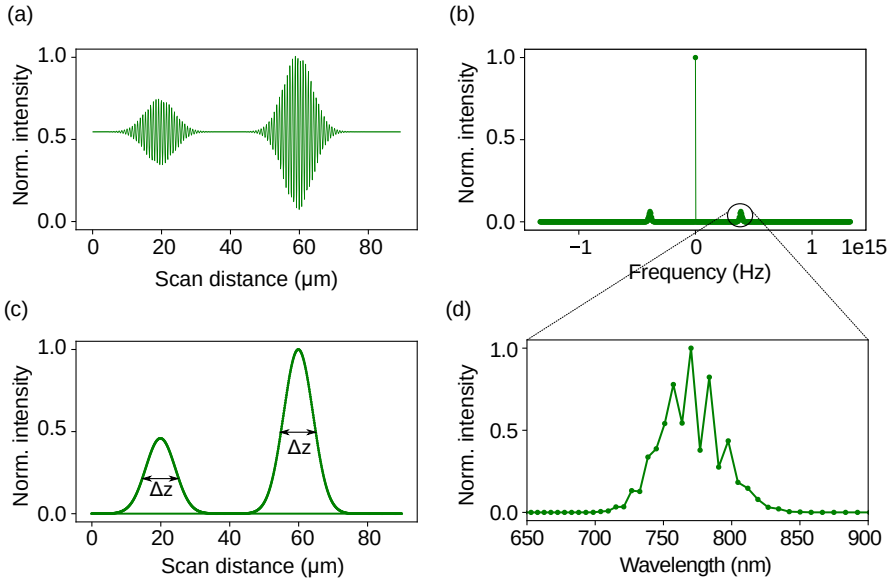

Figure 3.2: (a) Simulated inteferometric intensity as a function of reference scan distances. (b) Fourier transform of the inteferometric signal, where three terms (DC and two cross terms) are separated in the frequency domain. (c) Simulated depth response of a two-layer sample resolved from TDOCT. (d) Zoomed in intensity distribution of the selected cross term in the positive part of the spectrum in (b).

extracted from Eq. 3.2 due to the spectral separation as shown in Fig. 3.2(d). This results in:

$$I_{+1}(\omega, x, y) = A_o(\omega, x, y) A_r^*(\omega, x, y) e^{i\Delta\varphi(\omega,x,y)}, \tag{3.3}$$

Thus for each location (x,y) on the detector, we obtain a complex spectrum, in which the intensity is the product of the amplitudes of the reference and object field (Fig. 3.2(b)), and the phase is the phase difference between them as can be seen in Eq. 3.3. If plane waves are used as reference, this complex field is proportional to the diffracted field of the object. In other words, we obtain the full information of the spectrally resolved diffraction fields of the object, both the amplitude and phase. Thus, numerical refocus can be performed, where each individual diffraction pattern is numerically propagated back to the object plane as

$$\begin{aligned} E_o(\omega, x_0, y_0) &= \mathcal{P}\{I_{+1}(\omega, x, y)\} \\ &= \mathcal{P}\{A_o(\omega, x, y) A_r^*(\omega, x, y) e^{-i\Delta\varphi(\omega,x,y)}\}. \end{aligned} \tag{3.4}$$

In order to retrieve the depth information, an inverse Fourier transform along the frequency axis back to the time domain is performed:

$$E_o(t, x_0, y_0) = \mathcal{F}_\omega^{-1}\{E_o(\omega, x_0, y_0)\}. \tag{3.5}$$

The time delay t is directly related to the axial position inside the object, as the reflected light from an axial position z relative to the reference mirror distance is given by $z = 2ct$. Thus the final result $E_o(t, x_0, y_0)$ in Eq. (3.5) provides the full three dimensional reconstruction of the object. Figure 3.2(c) shows the resolved depth distribution of a simulated two-layer object.

3.2.2 *Computational SSOCT*

The computational SSOCT reconstruction shares the same principle as TDOCT, except that it requires one more Fourier transform and the cross correlation term is selected out in the time domain. As shown in Fig. 3.3(a), the three terms in Eq. 2.55 are separated in the time domain. After selecting out one of the cross terms, an inverse Fourier transform can be performed to obtain the spectrum as shown in Fig. 3.3(b), which leads to the same result as in computational TDOCT (Eq. 3.3), namely the full information of the diffracted fields from the object at each spectral component. Subsequently we can follow the same steps (Eq. 3.4-3.5) as in TDOCT to reconstruct the 3D object.

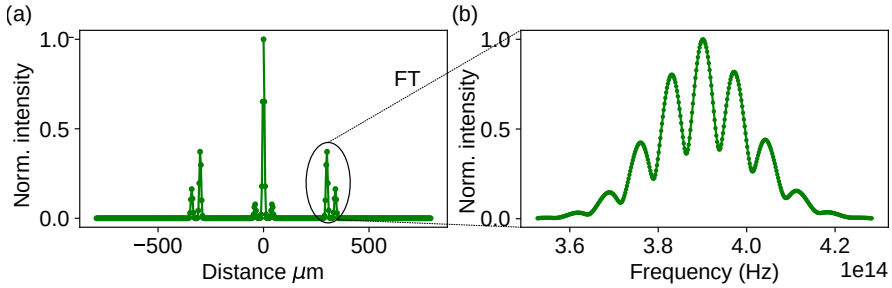

Figure 3.3: (a) Intensity distribution after Fourier transforming the interferometric signal in Fig. 2.13, where three terms (DC and two cross terms) are separated in the time domain. (b) Intensity distribution after Fourier transforming the positive cross order in Fig. 3.3(a) back to the frequency domain.

3.3 EXPERIMENTAL SETUPS AND PERFORMANCE CHARACTERIZATION

3.3.1 *Setup*

A key component in the experimental combination of OCT with lensless imaging is a spatially coherent broadband light source. A broadband supercontinuum white-light laser (NKT Photonics WhiteLase Micro, spectrum from 400 nm to 2000 nm, output power 200 mW) with a high degree of spatial coherence for all spectral components is used as shown in Figure 3.4(a). Short-pass (1000 nm) and long-pass (700 nm) color filters are used to select part of the spectrum for our experiments. A polarizing beamsplitter cube is used to create two paths 1&2 and to provide polarized input for the acousto-optic tunable filter (AOTF, Gooch and Housego: TeO2 AOTF I-TF950-500-1-2-GH96) in path 2. After the polarizing beamsplitter

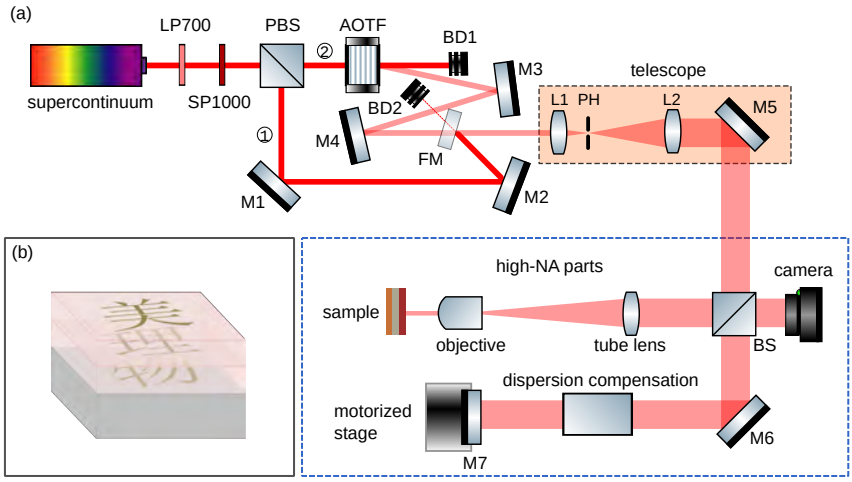

Figure 3.4: (a) Schematic of the setup. LP700: 700 nm long-pass filter, SP1000: 1000 nm short-pass filter, PBS: polarizing beamsplitter cube, AOTF: acousto-optic tunable filter, BS: beamsplitter cube, M: mirror, FM: flip mirror, BD: beam dump, L: lens, PH: pinhole. The setup has 4 different settings: low/high NA TDOCT and low/high NA SSOCT. The gray box contains the components for the high NA setting, consisting of an objective and a tube lens in the sample arm, and the dispersion compensation glass in the reference arm. (b) Schematic of a homemade 3-layer sample.

cube, path 1 (dashed line) is for TDOCT, where the light beam is directed by mirrors M1, M2, and flip mirror FM into the telescope (1:12 magnification with a 50 μm pinhole at the common focal plane) for spatial filtering and collimation. Path 2 (solid line) is for SSOCT, where an AOTF is used to sweep through the spectrum. The AOTF has a broad tuning range from 700 nm to 1200 nm, with sub-nanometer spectral resolution at a maximum modulation speed of 100 kHz, allowing for fast acquisition. The sub-nm spectral resolution enables an imaging depth up to 1.6 mm in air. The zeroth order transmitted beam from the AOTF is blocked, and the first order beam is directed by mirror M3 and M4 into the telescope and spatial filter that was already described above. The main imaging part (dashed blue box) of the setup is based on a Michelson interferometer. The components in the gray box are for high NA settings, where an objective (Mitutoyo, M Plan Apo NIR 10x, 0.26 NA) and a tube lens (Thorlabs, TTL200) are arranged in a telecentric configuration to guarantee a plane wave illumination [118]. Both TDOCT and SSOCT can be performed in either lensless or high NA settings, depending on insertion of these components. For the TDOCT measurements, a reference mirror is mounted on a motorized stage (PI N-565 with controller E861, 13 mm travel range, 0.5 nm system resolution), which scans the time delay between the reference and the sample arms with evenly spaced steps in a stop and go configuration. The stabilization time of the stage for each step is roughly 100 ms. As the shortest wavelength used in the experiment is 700 nm, to fulfill Nyquist

sampling and to take into account the double path in the reflection geometry, the biggest step size allowed is 175 nm. In our experiment 150 nm was chosen. At each step, a polychromatic interferogram is recorded by a 2D image sensor. Two different cameras have been used in the experiments, namely a Prosilica GT 3400 (Allied Vision Technology) with 3.69 μm pixel size and 3384*2704 pixels, and an ORCA-Flash 4.0 V3 (Hamamatsu), with 6.5 μm pixel size and 2048*2048 pixels. In the SSOCT measurements, the stage position is kept fixed, and spectral scanning is performed through electronic control of the AOTF. In these measurements, the camera is synchronized to the AOTF to record monochromatic interferograms at each wavelength.

To demonstrate 3D image reconstruction, multi-layer samples (Fig. 3.4(b)) are fabricated using UV lithography and thermal thin film deposition. Discrete structures are printed layer by layer using various metals, including gold, chromium, and germanium, with a thickness between 10 to 50 nm. In between different layers, photoresists are used as transparent media with a thickness ranging from 10 to 50 μm. Fabrication recipes are included in Appx. h.3.

3.3.2 *Transverse resolution*

The transverse resolution (half pitch) of the computational OCT system is in principle limited by the diffraction limit of the imaging system, $\frac{\lambda}{2NA}$. In reality, the camera pixel size and dynamic range can become limiting factors if the spatial sampling of the Fresnel diffraction pattern is not sufficient [71]. The simple lensless arrangement, featuring only free-space propagation from sample to detector, readily enables numerical aberration correction, but has a limited transverse resolution. To characterize the transverse resolution, we measured a 1951 USAF resolution target using the lensless TDOCT scheme (Fig. 3.4 without the high-NA parts in gray). An example of a measured polychromatic interferogram is shown in Fig. 3.5(a) and the 2D reconstruction is shown in Fig. 3.5(b) where the smallest resolved feature has a width of 11 μm (element 4 in group 5). In this case, the refocus distance from the camera plane to the object plane is 62 mm, which in principle leads to a detection NA of 0.08. With the central wavelength 780 nm, the diffraction limited resolution is 4.9 μm, which is a factor two lower than what is actually achieved. This discrepancy is mainly due to the limited dynamic range of the camera, leading to a reduced signal strength for the higher diffraction angles of the structure.

In order to improve the transverse resolution, the high-NA optics is used as shown in Fig. 3.4(a). This increases the detection NA to 0.26, and at the same time the additional 10x magnification of the imaging system results in an effective sub-micron pixel size in the detected image (0.65 μm for the Hamamatsu camera, and 0.369 μm for the AVT). This makes it possible to achieve diffraction-limited resolution. The OCT measurements can be done either in the image plane or in an out-of-focus Fresnel diffraction plane. Figure 3.5(c) shows a high-NA measurement of the USAF target in the Fresnel regime, performed with SSOCT. After extracting the phase of the diffraction patterns at each wavelength using the methods described in the previous section, we numerically refocus the sample in Fig. 3.5(d).

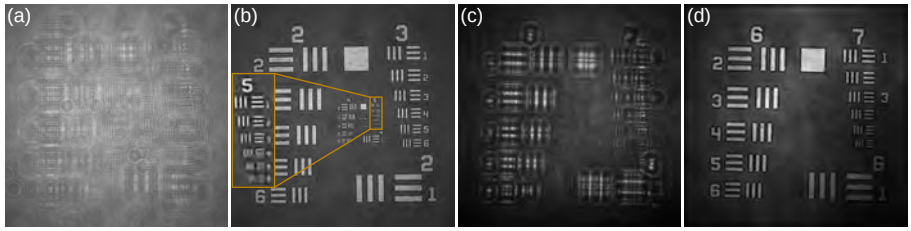

Figure 3.5: Typical imaging results obtained with lensless OCT in different configurations. (a,b) Measurement and reconstruction of a USAF sample using the lensless TDOCT method. (c,d) Measurement and reconstruction of a USAF sample using the high-NA SSOCT method.

The smallest element (element 6 in group 7) on the USAF target is well resolved, demonstrating a transverse resolution better than 2.2 μm.

3.3.3 *Axial resolution*

Similar to traditional OCT, the axial resolution of our imaging systems are determined by the coherence length of the light source. The axial point spread function is mainly determined by the shape of the source spectrum, but dispersion differences between the reference and sample arm need to be compensated as well to achieve optimum depth resolution. Gaussian shaped spectra are considered ideal for not having side lobes in the axial response. However, most broadband light sources do not have smooth Gaussian spectra, thus spectral shaping before and after data acquisition have both been studied [119–122]. Numerical spectral shaping in the post-processing step has the advantage that it also accounts for the spectral response of optical components and detector. Besides Gaussian spectra, other spectral shapes have been proposed to improve axial resolution, including flat, Hamming-windowed, as well as adaptively shaped spectra for sidelobe reduction [123, 124]. In our case, the complex spectrum of the backscattered light recorded by the camera can be calculated by Eq. 3.3, directly enabling post-processing spectral shaping. With a desired shape, for instance a super-Gaussian spectrum, we calculate the ratio between the original resolved spectrum and the desired spectrum to obtain a correction curve. In Fig. 3.6(a), the resolved spectrum from a USAF target measurement (using high-NA SSOCT), together with the assigned super-Gaussian shape is presented. The corresponding axial responses for the direct source spectrum, the super-Gaussian filtered spectrum, and the dispersion-compensated filtered spectrum are plotted in Fig. 3.6(c). It can be seen that the raw broadened, noisy axial response (blue trace) is only slightly improved after the spectral shaping (orange trace), and that the main improvement comes from the numerical dispersion compensation as will be further discussed below.

The main obstacle for getting an optimal axial resolution in our system is chromatic dispersion. When light of a broad spectral range passes through an asymmetric interferometer that has different amounts of dispersive materials in

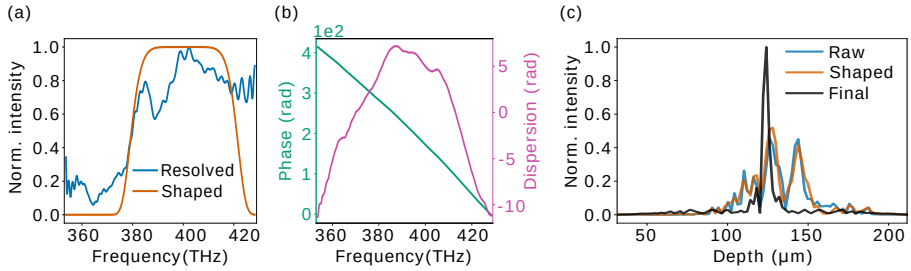

Figure 3.6: A USAF sample measured by high-NA SSOCT method: (a) Resolved spectrum and final shaped spectrum. (b) Averaged phase (left axis) and extracted dispersion (right axis). (c) Axial response from the raw data, after spectral shaping and after dispersion compensation (final).

the two arms, a spectrally dependent phase mismatch between the light fields from the two arms is induced. This is a common problem in traditional OCT, causing a deterioration of the achievable axial resolution. In order to achieve Fourier-limited axial resolution, both hardware- and software-based dispersion compensation methods have been proposed. Choosing identical optics or adding dispersive materials to physically match the optical materials in the two arms of the interferometer can compensate for non-sample induced dispersion [125, 126]. Theoretical modeling of dispersion from specific samples, e.g. human eyes, has been applied to obtain optimal axial resolution [127, 128]. Additionally, iterative optimization based on the sharpness of the image has been demonstrated [129, 130], as well as numerical dispersion control to increase the axial range in frequency-domain OCT [104, 131]. The interferometric OCT measurement scheme directly provides the phase information in the spectral domain (Eq. (3.3)), facilitating numerical dispersion compensation. The measured phase difference $\Delta\varphi(\omega)$ between the backscattered object field and reference field can be expanded into a Taylor series [132]:

$$\Delta\varphi(\omega) = \varphi(\omega_0) + \left.\frac{d\Delta\varphi}{d\omega}\right|_{\omega_0}(\omega-\omega_0) + \frac{1}{2}\left.\frac{d^2\Delta\varphi}{d\omega^2}\right|_{\omega_0}(\omega-\omega_0)^2 + \dots , \tag{3.6}$$

where the zeroth-order term $\varphi(\omega_0)$ is a constant phase term at frequency ω_0, and the first-order term (the group delay) represents the linear phase difference due to the global optical path delay between the reference and the object. The longer the delay, the steeper the slope of the phase $\frac{d\Delta\varphi}{d\omega}$. The second- and higher-order terms are referred to as the dispersion terms that lead to broadening and distortion of the axial resolution, and any (numerical) dispersion compensation scheme aims to minimize these terms. In our lensless arrangement, direct characterization of dispersion is done by fitting a linear function to the resolved phase along the frequency axis and calculating the residual. In the high-NA arrangement, a combination of software- and hardware-based compensation is required, as the dispersion caused by the objective and tube lens in the sample arm is so severe that the first order interference signals extend well beyond the axial measurement range. Thus, prior to the numerical compensation, dispersive glass is added

in the reference arm to reduce the dispersion to a level where extraction of the interferometric cross-term (Eq. 3.3) is feasible. In Fig. 3.6(b) we show the resolved phase and dispersion from the USAF sample measurement. The final axial response after both spectral shaping and dispersion compensation is plotted in Fig. 3.6(c), where 3.5 μm axial resolution in air is achieved. Considering that the DoF of the high NA system is 12 μm, the achieved axial resolution is more than 3 times better. Note that this short DoF would severely limit the axial measurement range in traditional OCT. In contrast, the numerical refocusing capability of computational OCT allows the use of such a high-NA configuration while maintaining the axial range set by the spectral resolution of the measurement system, without loss of transverse resolution outside the DoF.

3.4 EXPERIMENTAL RESULTS ON COMPUTATIONAL 3D IMAGING

In the previous section we discussed characterization measurements on a single-layer USAF sample using different combinations of low- and high-NA, TDOCT and SSOCT to benchmark the achievable resolution. As a next step, reconstructions of home-made lithographic multi-layer samples are presented, and the performance of TDOCT and SSOCT is compared. As a first experiment, a home-made two-layer sample is measured in the low-NA lensless TDOCT arrangement, where a stack of polychromatic diffraction patterns is recorded during the data acquisition. In Fig. 3.7(a), the interference between the diffracted fields from the sample and the reference fields is shown. After numerical reconstruction, two different structures separated in depth are resolved, which are shown in Figs. 3.7(b) and 3.7(c), respectively. Due to the opacity of the top layer (consisting of 50 nm thick gold), a shadow is projected on the bottom layer tomogram. For comparison, the optical microscope image of the sample is shown in Fig. 3.7(d), where both layers are shown at the same time. The second row of Fig. 3.7 shows the reconstruction of another two-layer sample with smaller feature size measured in the high-NA TDOCT arrangement. Following the same reconstruction procedure, 2 μm features are resolved.

As a first characterization of the SSOCT method, the reconstruction of a home-made three-layer sample measured in the high-NA arrangement is shown in Fig. 3.8. The three-layer sample is placed outside the focal plane of the objective. As can be seen in Fig. 3.8(a), all three-layer structures are out of focus. The resolved depth distribution of the whole sample, after the dispersion compensation and spectral shaping, is plotted in Fig. 3.8(b). In this graph the depth axis corresponds to the physical distance of the sample, which is converted from the direct result of optical distance while taking into account the double pass in the reflection geometry and the refractive index of the sample. From this measurement a depth resolution of 2.3 μm (FWHM) in the sample is obtained, and the physical distance between adjacent layers is measured to be 15 μm, which agrees with the expectation from the fabrication procedure. Figures 3.8(c) and 3.8(g) are the optical microscopy images taken from both sides of the sample, where the structure on the middle layer is not recognizable. In contrast, reconstructed tomograms of all three layers of the sample as measured with computational OCT are shown in Figs. 3.8(d-f) respectively. The structured layers in this three-layer

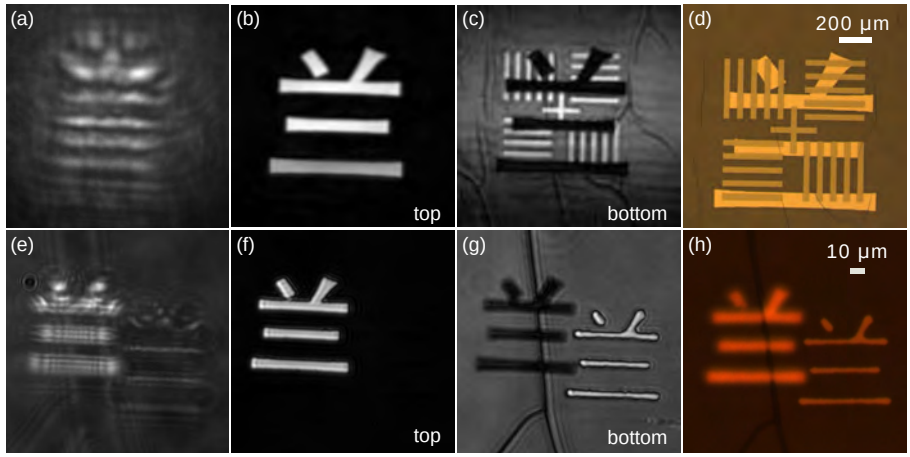

Figure 3.7: Row 1: Measurement of a two-layer sample in the low-NA TDOCT configuration. Row 2: Measurement of a different two-layer sample with smaller features (in order to show the improved transverse resolution) in the high-NA TDOCT configuration. (a) A raw camera frame from the stack of polychromatic interferogram measurements. (b,c) Reconstructed tomograms of the top and bottom layers of the sample. (d) Optical microscope image (5x, 0.13 NA) of the sample. The scale bar specifies the transverse dimension of the two-layer sample. The axial separation of the two layers is 26 μm. (e) A raw camera frame from the stack of polychromatic interferogram measurements. (f,g) Reconstructed tomograms of the top and bottom layers of the sample. (h) Optical microscope image (10x, 0.25 NA) of the sample. The scale bar specifies the transverse dimension of the two-layer sample. The axial separation of the two layers is 28 μm.

sample are made of 10 nm thick layers of Germanium, which are semi-transparent in the near-infrared range. Therefore, the shadowing effect that is visible in the reconstructions shown in Fig. 3.7 is much less apparent in the middle (c) and bottom (d) layer reconstruction for this object. In these high-NA measurements, the axial extent of the sample is larger than the DoF of the system. Therefore, numerical refocusing is done for each layer separately to obtain focused images of the individual layers. In Fig. 3.8(h-j) we show the three-layer reconstruction when only one focal distance (for the bottom layer of the sample Figs. 3.8(f,j)) is chosen. The defocus effect in the middle layer (Fig. 3.8(i)) and the top layer (Fig. 3.8(h)) can be observed.

To enable a direct comparison, the same three-layer sample is also measured in the high-NA TDOCT arrangement. Eight hundred images are recorded covering a scanning range of 120 μm in air (corresponding to 80 μm in the sample). Due to the limited speed of the scan stage, the data acquisition takes about 60 seconds, which is more than 10 times slower than the acquisition time in SSOCT, where 400 images are recorded during a wavelength scan from 700 nm to 850 nm. Due to the fast AOTF sweeping, in SSOCT the speed limitation is the camera (max

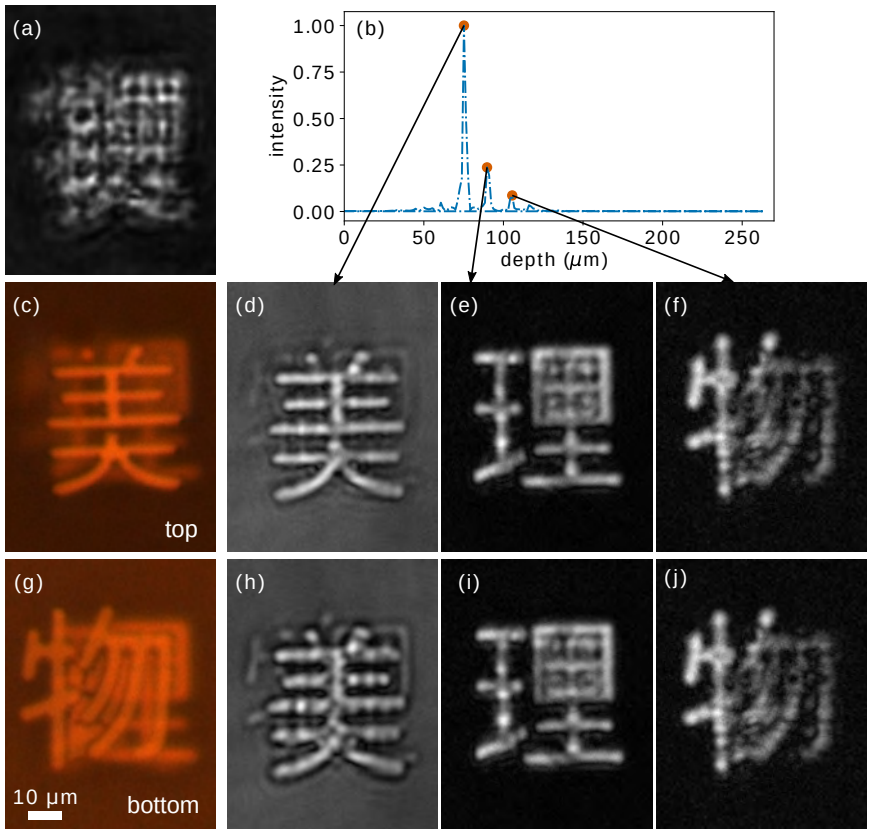

Figure 3.8: (a) A single camera frame taken from a high-NA SSOCT measurement series. (b) Resolved depth distribution of the three-layer sample. (c,g) Optical microscope image (10x, 0.25 NA) of the three-layer sample from the front and back sides. The scale bar specifies the transverse dimension of the three-layer sample. The separation between adjacent layers is 15 μm. The 3D rendering of the sample is shown in Fig. 3.4(b). Reconstructed tomograms of the three layers of the sample with (d-f) and without (h-j) numerical refocusing for each individual layer.

100 fps), while in TDOCT the main limitation is the time required for accurate stage positioning. In fact, in our present setting the SSOCT measurement covers a 3 times larger depth range within the aforementioned measurement time, so that the difference in data acquisition speed actually reaches a factor 30.

The resolved depth resolution in TDOCT is 2.3 μm, which is the same as in SSOCT within the experimental accuracy (see Fig. 3.9(a,b)). The resolved positions of the peaks are all relative to the starting position of the reference, so the absolute numbers in terms of depth can be different. The peak width and the relative distance between the peaks as measured with the two different methods are both in good agreement. The total incident energy on the sample integrated over the duration of the scan was 17 μJ and 31 μJ for TDOCT and SSOCT respectively. At

these energies the final signal to noise ratio (SNR) in TDOCT is 3 dB lower than in SSOCT, which is directly explained by the difference in energy on sample. For further comparison, a series of simulations has been performed to investigate the noise sensitivity of the respective methods (Fig. 3.9(c,d)). From these simulations we find that the influence of the background signal, which is less than 5% of the maximum signal level in our measurements, has a limited effect on the SNR in both cases. However, in principle TDOCT is more sensitive to the noise from the detection side compared to SSOCT, because in the latter case any randomly distributed noise will be filtered by the additional Fourier transform [99, 100]. This can be seen in Figs. 3.9(c) and 3.9(d), where 30% noise is added in the simulation on a two-layer object in both TDOCT and SSOCT. The noise floor is significantly increased for the case of TDOCT, while the SNR for the SSOCT reconstruction is only slightly affected.

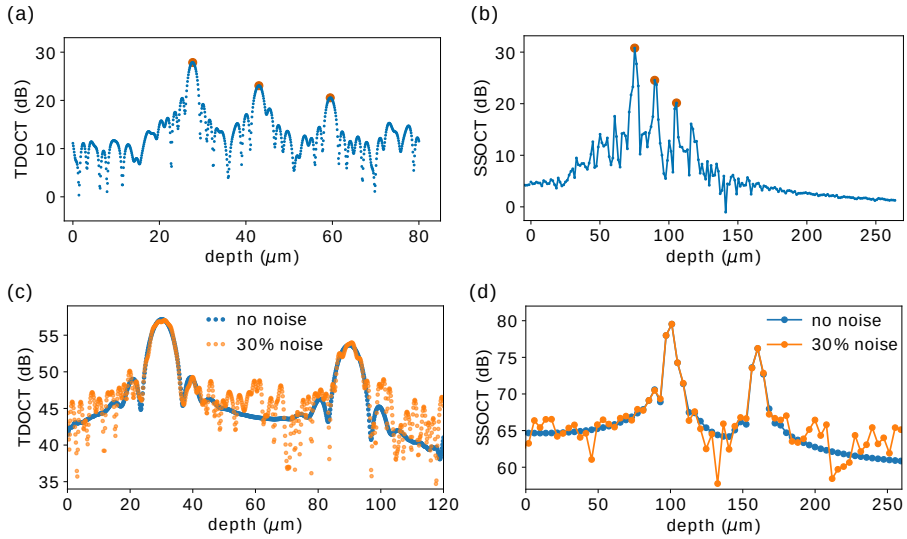

Figure 3.9: Experimentally determined depth distribution of the three-layer sample measured with (a) high-NA TDOCT and (b) high-NA SSOCT on a logarithmic scale. (c,d) Simulated depth response with 30% noise added, and without noise on a two-layer object.

In summary, we have shown a comprehensive comparison of computational full-field OCT methods for tomographic reconstruction of 3D objects. In a single setup, we have combined low- and high-NA imaging systems as well as time-domain and swept-source OCT configurations, enabling a direct comparison of these different methods in terms of achievable resolution, depth range, measurement speed and noise sensitivity. Using this system, we show the advantage of computational imaging methods in OCT to enable high-NA transverse imaging combined with a large depth range that extends well beyond the DoF of the imaging hardware. The lensless (low-NA) arrangement allows for a simple and flexible experimental setup, but has a limited transverse resolution. A significant resolution improvement is

provided by incorporating high-NA optics, which does require additional effort in dispersion balancing in the setup. With a homemade three-layer sample, we demonstrate a 3D reconstruction with 2 μm transverse and 3.5 μm axial resolution, and a measurement depth range of >200 μm.

3.5 INVERSE SCATTERING POINT OF VIEW OF OCT

We have shown that numerical refocusing can be used to enable a large imaging depth across the object, where different back-propagation distances can be chosen to produce sharp images at different depths inside a 3D object. In this section, we show that it is possible to bring the complete depth range of a 3D object into focus simultaneously. This is realized by interpreting OCT data in the inverse-scattering point of view [116]. Here, we show both the theoretical derivation and the implementation with experimental data.

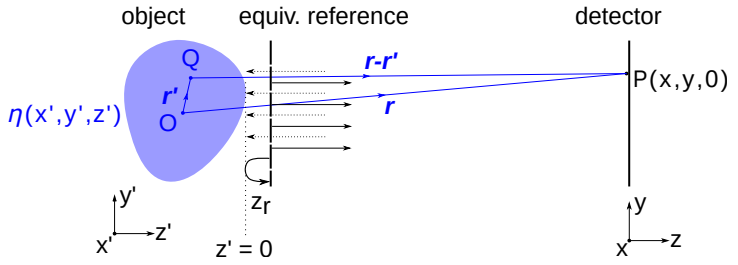

Figure 3.10: Schematic of an OCT measurement geometry. (x', y', z') is the object coordinates, and (x, y, z) is the detection coordinates. $\eta(x', y', z')$ is the 3D susceptibility function of the object. The equivalent position of the reference mirror in the interferometric detection in SSOCT is marked by the vertical lashed line. z_r represents the optical delay distance between the top layer of the object and the reference. For convenience, we set the first layer of the object at $z' = 0$, and the detector plane at $z' = z$.

In order to better understand the problem, we start from setting up the forward model in full-field SSOCT. It is convenient to formulate the model in the frequency domain, nevertheless it has been shown in Sec. 3.2 that TDOCT shares the same principle. As depicted in Fig. 3.10, a 3D object, described by the susceptibility function $\eta(\mathbf{r}')$, is illuminated by a plane wave along z' direction given by:

$$E_i(\mathbf{r}'; k) = A(k) e^{-ik\mathbf{r}'\cdot\hat{\mathbf{z}} + i\phi_0(k)}, \tag{3.7}$$

where $\mathbf{r}' = (x', y', z')$ denotes the object coordinates, $k = \frac{2\pi}{\lambda}$ is the wavenumber, $A(k)$ is the power spectral density of the broadband light source, and $\phi_0(k)$ is the initial phase difference at each frequency. Under the first Born approximation [133], the back-scattered field from the object can be written as:

$$E_s(\mathbf{r}; k) = \iiint_V E_i(\mathbf{r}'; k)\eta(\mathbf{r}') \frac{e^{ik|\mathbf{r}-\mathbf{r}'|}}{|\mathbf{r}-\mathbf{r}'|} d^3\mathbf{r}', \tag{3.8}$$

where $\mathbf{r} = (x, y, z)$ denotes the position vector in the detection coordinates as shown in Fig. 3.10. Returning from the other arm of the interferometer, the reference field at the detector plane can be expressed as:

$$E_r(\mathbf{r}; k) = A(k)e^{i[k(z-z_r)+\phi_0(k)]}, \tag{3.9}$$

where z_r represents the optical path length difference between the reference beam and the first layer of the object as shown in Fig. 3.10. Note that we assume a perfect flat mirror with reflectivity of 1 and the phase-shift induced upon reflection is neglected. At the detector plane, the measured intensity of the interference signal between the back-scattered field from the object and the reference field is given by:

$$I(\mathbf{r}; k) = |E_r(\mathbf{r}; k) + E_s(\mathbf{r}; k)|^2. \tag{3.10}$$

As explained in section 3.2.2, one of the cross terms can be selected out:

$$\begin{aligned} E_{+1}(\mathbf{r}; k) &= E_r^*(\mathbf{r}; k)E_s(\mathbf{r}; k) \\ &= A^2(k)e^{-ik(z-z_r)} \iiint_V e^{-ikz'}\eta(\mathbf{r}')\frac{e^{ik|\mathbf{r}-\mathbf{r}'|}}{|\mathbf{r}-\mathbf{r}'|}d^3r'. \end{aligned} \tag{3.11}$$

From Eq. 3.11 we can see that one of the advantages offered by the interferometric detection of OCT is that the initial phase difference $\phi_0(k)$ between wavelengths is canceled out. In order to solve for the object susceptibility $\eta(\mathbf{r}')$ from Eq. 3.11, we perform a 2D Fourier transform on both side of the equation along axes x and y, and we obtain:

$$E_{+1}(\mathbf{k}_{||}; k) = \frac{i2\pi A^2(k)e^{-ik(z-z_r)}}{k_z} \iiint_V \eta(\mathbf{r}')e^{-i[\mathbf{k}_{||}\cdot\mathbf{r}'+z'(k+k_z)]}d^3r', \tag{3.12}$$

where the 2D Fourier transform of the Green's function is calculated by using the Weyl equation [133]:

$$\iint \frac{e^{ik|\mathbf{r}-\mathbf{r}'|}}{|\mathbf{r}-\mathbf{r}'|}e^{-i\mathbf{r}\cdot\mathbf{k}_{||}}d^2r = i2\pi\frac{e^{-i[\mathbf{k}_{||}\cdot\mathbf{r}'+k_z z']}}{k_z}. \tag{3.13}$$

In the above equations, $\mathbf{k}_{||} = \mathbf{k_x} + \mathbf{k_y}$, $k_z = \sqrt{k^2 - k_{||}^2}$. We can see from Eq. 3.12 that the 3D integral term takes the form of a 3D Fourier transform:

$$\iiint_V \eta(\mathbf{r}')e^{-i[\mathbf{k}_{||}\cdot\mathbf{r}'+z'(k+k_z)]}d^3r' = \eta(\mathbf{q})|_{q_x=k_x, q_y=k_y, q_z=k+k_z}. \tag{3.14}$$

Thus, we can re-write the Eq. 3.11 as:

$$E_{+1}(\mathbf{k}_{||}; k) = \frac{i2\pi A^2(k)e^{-ik(z-z_r)}}{k_z}\eta(\mathbf{q})|_{q_x=k_x, q_y=k_y, q_z=k+k_z}, \tag{3.15}$$

which gives the relation between the cross term obtained from OCT measurements and the 3D Fourier transform of the object susceptibility function. The latter is given by:

$$\eta(q_x, q_y; q_z) = \eta(k_x, k_y; k + k_z) = \frac{E_{+1}(k_x, k_y; k)k_z e^{ik(z-z_r)}}{i2\pi A^2(k)}. \tag{3.16}$$

Since originally the OCT data (E_{+1}) is uniformly sampled in k_x, k_y and k, we need to first resample the data uniformly in the 3D Fourier coordinates $q_x = k_x$, $q_y = k_y$, and $q_z = k + k_z(k_x, k_y)$ via interpolation. Then a one-step 3D inverse Fourier transform can reveal the susceptibility distribution of the sample:

$$\begin{aligned}\eta(x', y', z') &= \mathcal{F}^3\{\eta(q_x, q_y, q_z)\} \\ &= \mathcal{F}^3\{\frac{E_{+1}(q_x, q_y; k(q_z))k_z(q_z)e^{ik(q_z)(z-z_r)}}{i2\pi A^2(k)}\},\end{aligned} \tag{3.17}$$

and in this case all the depths inside the object can be focused at the same time.

For a clear comparison to the single-layer back-propagation approach, we rearrange Eq. 3.12 by calculating only the 2D Fourier transform along axes x' and y', which results in:

$$E_{+1}(\mathbf{k}_{||}; k) = \frac{i2\pi A^2(k)}{k_z}\int_{z'}\eta(kx, ky, z')e^{-iz'k_z}e^{-iz'k}dz', \tag{3.18}$$

where we can see that the term $e^{-iz'k_z}$ represents the depth-related phase accumulation, namely the diffraction effect inside the object. Back-propagating to a specific depth fails to account for the diffraction effect of signals returned from other depths inside the object, therefore limiting the focus range to the DoF of the system. Thus resampling eliminates the DoF limitation, enabling simultaneous refocus of the entire object.

To verify this concept, we apply the resampling approach to both simulated and measured data. First, we performed a SSOCT simulation on a two-layer sample, where the layer separation is 650 µm and the DoF is 60 µm . In Fig. 3.11(a) and (b), the reconstructed tomograms without resampling are shown. When choosing the correct back-propagation distance for the top layer (a cross), we can see that the reconstructed bottom layer structures (circles) are severely defocused. After resampling, the reconstructed tomograms are shown in Fig. 3.11(c) and (d), where both depths are in focus. In fact, the shadow of the top layer cross becomes blurred on the bottom layer in Fig. 3.11(d). The same comparison for the measured data is presented in Fig. 3.12, where Fig. 3.12(a-c) are tomograms reconstructed without resampling, and the back-propagation distance is chosen for the bottom layer. Since the layer separation is 15 µm and the DoF is 12 µm, only a slight defocus effect can be observed on the top layer reconstruction (in Fig. 3.12(a)). After resampling, the reconstructed tomograms are shown in Fig. 3.12(d-f), where all three characters are sharp simultaneously and less cross-talk is observed.

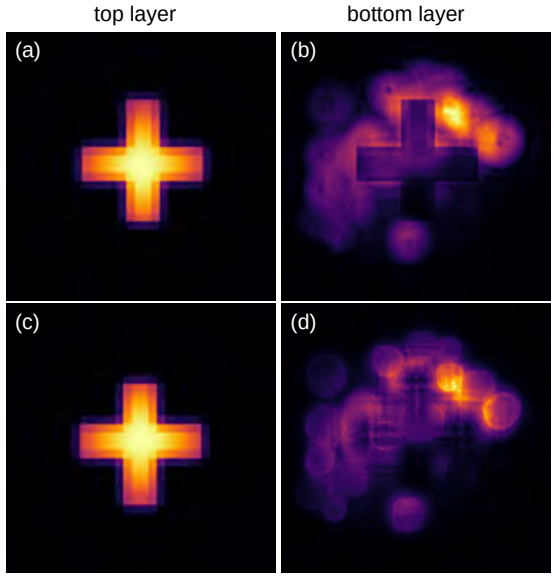

Figure 3.11: Simulation of a two-layer object: (a)(b) Tomograms of the top and bottom layer before resampling. (c)(d) Tomograms of the top and bottom layer after resampling.

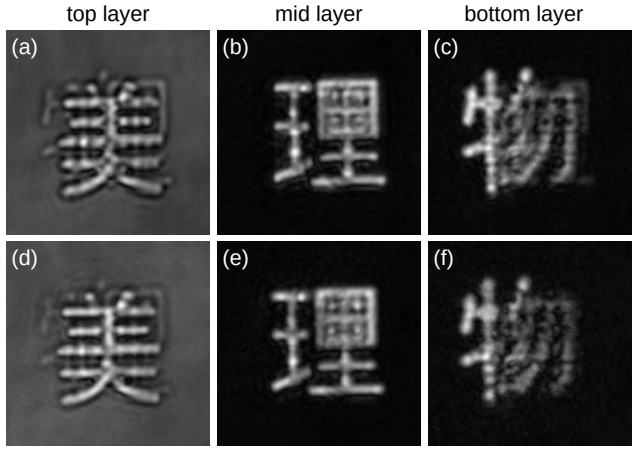

Figure 3.12: Experimental results of a three-layer sample: (a-c) Tomograms of the three layer before resampling. (d-f) Tomograms of the three layer after resampling.

4

PTYCHOGRAPHIC OPTICAL COHERENCE TOMOGRAPHY

ABSTRACT

Computational imaging is a powerful approach to microscopy, in which the performance of an imaging system can be enhanced beyond conventional hardware limits. Ptychography in particular has proven to be a robust computational imaging technique capable of producing quantitative images of complex electric fields. The ability for high-resolution depth sectioning is a major advantage for any imaging method, which so far has remained challenging for wide-field computational imaging methods. Here we demonstrate an approach to high-resolution 3D computational imaging, by combining ptychography with spectral-domain imaging methods inspired by optical coherence tomography (OCT). This results in a simple and flexible imaging system that features the main advantages of OCT, such as the ability for depth-sectioning without the need for sample rotation, decoupling of transverse and axial resolution, and an axial resolution only determined by the source bandwidth. Furthermore, the interferometric reference needed in OCT is replaced by computational methods, further improving the simplicity and robustness of the hardware layout. As ptychography is capable of separating the influence of the probe beam, speckle-free images are obtained. We demonstrate the capabilities of ptychographic optical coherence tomography (POCT) by imaging an axially discrete two-layer lithographic structure, as well as an axially continuous mouse brain sample .

A research article based on this chapter has been published: "Du, M., Loetgering, L., Eikema, K.S.E. & Witte, S. Ptychographic optical coherence tomography. *Optics Letters* **46**, 1337-1340 (2021)."

4.1 INTRODUCTION

Ptychography [30, 31] is a powerful computational imaging technique, which has been successfully applied using various radiation sources, e.g. optical, EUV, x-ray and electron sources [78, 84, 85, 87]. In addition to ptychography's success in two-dimensional imaging, various methods have been investigated to extend the technique to three dimensions. The 2D or single-slice ptychographic forward model assumes a thin object such that the interaction between the probe and object can be factorized into a simple multiplication [78]. For thick samples that do not satisfy the multiplication condition, multi-slice ptychography [89, 90, 134] has been developed to computationally divide the thick sample into thin slices such that on each slice the 2D ptychography approach is applicable. Then, by sequentially propagating the modified waves through the thick object slice by slice, a three-dimensional (3D) reconstruction can be recovered. Multi-slice ptychography has been demonstrated with optical, x-ray, and electron sources [90, 135, 136], and its limitations have been explored [134]. One complicating factor is that the axial sectioning requires a highly structured probe beam. In addition, the depth resolution of the multislice method is limited to the order of the depth-of-field (DoF) of the ptychography setup, which makes it challenging to image axially continuous objects. Another approach to extend conventional ptychography to 3D is to combine it with other 3D imaging modalities. In the x-ray regime, techniques termed ptychographic tomography (PT) [20, 91, 137] and laminography [138, 139] combine 2D ptychography with computed tomography (CT), where a 3D image is reconstructed tomographically from 2D reconstructions at different object viewing angles. Recently, an addition to PT, namely multi-slice ptychographic tomography (MSPT) [140], has been introduced to extend the imaging depth of the technique while preserving the depth resolution. But in general, a drawback of tomographic techniques is the requirement for dense, time consuming angular scans.

In the optical regime, one of the most influential 3D imaging methods is optical coherence tomography (OCT) [2, 141–143]. OCT obtains 3D information of an object by measuring interference signals between light backscattered from the object and an external reference using a broadband light source. Depending on measurement schemes, two main variations are time-domain OCT [2] and Fourier-domain OCT [144, 145]. The former directly measures interference signals as a function of time delay by scanning a reference arm axially, while the latter measures interference signals as a function of wavelength by either using a spectrometer or a swept-source, which offers speed and sensitivity advantages [99–101]. OCT has also been extended and/or combined with other computational imaging techniques to account for refractive distortion and multiple scattering inside the imaged 3D volume [33, 34, 106, 146]. OCT is a coherent imaging modality and as a result requires the use of a stable interferometric reference arm to encode temporal phase. The conversion of the resulting interferograms into depth information does have limitations in the form of autocorrelation and conjugate image artefacts. Furthermore, OCT suffers from speckle noise intrinsic to most coherent imaging methods.

Here we present a new technique that enables high-resolution 3D imaging in a reflection geometry, without the need for object rotation or interferometry, by

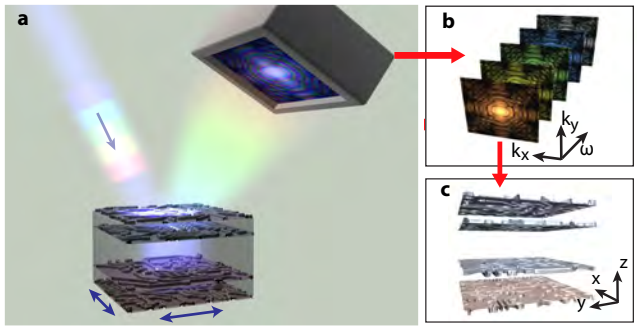

Figure 4.1: Schematic illustration of the ptychographic optical coherence tomography concept. A) Diffraction patterns of the irradiated object are recorded with a camera for a series of sample translations, and a fast wavelength scan is performed at each ptychographic scan position. B) The imaging strategy results in a frequency-resolved set of diffraction patterns. C) 2D ptychographic image reconstructions are performed at each wavelength, to retrieve the wavelength-dependent complex-valued exit surface wave. The relative phase between the different wavelength images is set by phase synchronization at a synthetic reference plane. A 1D Fourier transform from frequency- to time-domain then reveals the depth information in the 3D object.

combining ptychography with swept-source OCT. We demonstrate this ptychographic optical coherence tomography (POCT) technique using a near-infrared swept-source laser in a lensless ptychographic setup, where a fast wavelength scan is performed at each ptychographic scan position. The POCT concept is outlined in Figure 4.1.

Inheriting from OCT, the axial resolution in POCT is decoupled from the lateral resolution and only limited by the source spectral bandwidth. This feature enables fine depth sectioning, not limited by the DoF of the imaging setup that would limit a multi-slice ptychography approach. The electronically controlled wavelength scan offers a speed advantage over angular scans needed in tomographic approaches. Furthermore, by using ptychography's ability to retrieve the complex-valued fields of both the probe beam and the object, POCT provides clean tomographic reconstructions free of speckle artefacts that are common in OCT. As the phase is retrieved through computational methods, the interferometric reference arm can be eliminated from the setup, resulting in a simple, compact and robust layout. We show POCT reconstructions of both an axially discrete two-layer lithographic sample and an axially continuous mouse brain sample.

4.2 EXPERIMENT AND METHODS

Figure 4.2 shows the schematic of the POCT experimental configuration where a swept-source is used in a reflection ptychography setup. Details of the swept-source system are described in Sec. 3.3.1. In the reflection ptychography part, an iris is imaged onto the sample surface to create a localized probe. The sample is translated by a 2D motorized stage in a Fermat's spiral pattern [147]. At each

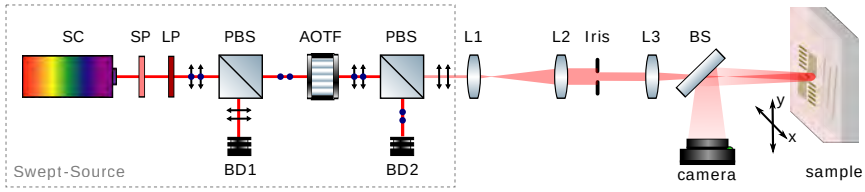

Figure 4.2: POCT experimental setup. The swept-source section consists of a supercontinuum laser (SC), a short pass (SP: 1000 nm) and long pass (LP; 700 nm) filters, polarizing beam splitters (PBS) and an acousto-optic tunable filter (AOTF). BD1,2: beam dumps. Lenses L1 ($f_1 = 50$ mm) and L2 ($f_2 = 150$ mm) are used to expand the beam. An iris is imaged onto the sample surface by the lens L3 ($f_3 = 50$ mm). The object is mounted on an encoded 2D translation stage (2x Smaract SLC-1770-D-S, 46 mm travel range, 70 nm repeatability). The backscattered light from the sample is directed by a beamsplitter(BS) to a CCD camera (AVT prosilica GX1920, 14 bit, pixel size 4.54 µm), with which intensity images are recorded.

scan position, an equidistant frequency scan is performed and monochromatic back-scattered intensity patterns are recorded by the camera at each frequency. Lenses L1, L2, L3 and the iris are used to create and control a localized probe for ptychography.

After the data acquisition, single-slice ptychographic reconstructions are performed at each wavelength. Theoretically, the multiplicative approximation in single-slice ptychography holds [148] when the sample thickness T satisfies $T \leq \frac{2(\Delta r)^2}{\lambda}$, where λ is the wavelength and $\Delta r = \lambda / NA$ is the lateral spatial resolution. Numerical simulations [134] have shown a more relaxed criterion: $T \leq \frac{5.2(\Delta r)^2}{\lambda}$, which is more than two times the theoretical limit. Under the multiplicative approximation, single-slice ptychography offers quantitative object reconstruction, with which high-resolution surface profilometry has been successfully demonstrated [84, 149]. By measuring semi-transparent samples and using multiple-wavelength measurements, POCT aims at volumetric imaging.

Our data analysis pipeline is summarized in Fig. 4.3. At the starting wavelength, we use an auto-focus algorithm specifically tailored to ptychography [150] to calibrate the sample-detector distance. Using this calibration, a momentum-accelerated ePIE algorithm [93, 94] is used to reconstructed the object and probe. Thanks to the small step size in the wavelength scan, the previously reconstructed probe and object can be used as initial guesses for the following reconstruction to speed up the convergence rate. In this way ptychographic reconstructions are performed wavelength by wavelength.

Although quantitative object reconstructions are obtained at each wavelength, initially they appear uncorrelated because of several reasons. Firstly, the reconstructed object pixel size is proportional to the wavelength since Fraunhofer propagation [38] is used. Secondly, the absolute lateral position of the object is one of the ambiguities of ptychography, thus object reconstructions are arbitrarily shifted as shown in Fig. 4.3. Last but not least, there is a random constant phase

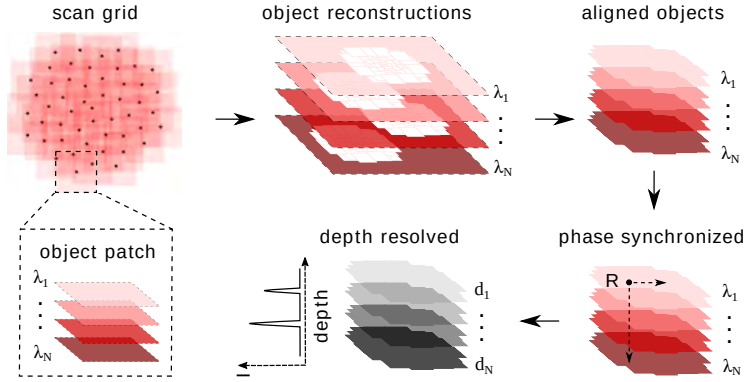

Figure 4.3: POCT data analysis pipeline, after measuring diffraction images at M scan positions with N wavelengths. Single-slice ptychographic reconstructions are performed for each wavelength λ_N, after which all object reconstructions are aligned by scaling and registration, and phase synchronized using a synthetic reference signal. A final Fourier transform reveals the depth distribution.

term for each object reconstruction due to the non-uniqueness of a constant phase offset in ptychography. For lateral alignment, all estimated objects are scaled and linearly interpolated to the reconstruction with the smallest pixel size, and then registered with sub-pixel precision [151]. The phase relation between the different wavelength images can be determined from the object itself, thereby replacing the external interferometric reference surface in swept-source OCT, provided the signal is dominated by a single depth reflection at one object location. In contrast to common-path OCT [152], no flat reference layer is required as phase shifts in one layer are identified by the ptychographic reconstruction upon phase synchronization at a single object location (pixel). Once a reference position is chosen, we synchronize the constant phase offsets of all wavelengths at this position. Finally, a 1D Fourier transform along the wavelength axis reveals the depth information of the object. Given by the Fourier transform relation, the optical sectioning resolution is:

$$\Delta z_{opl} = \frac{\lambda_1 \lambda_N}{|\lambda_1 - \lambda_N|}. \tag{4.1}$$

Taking into account the refractive index n of the object and the double pass in the reflection geometry, the physical depth resolution is given by $\Delta z_{phy} = \frac{\Delta z_{opl}}{2n}$.

4.3 RESULTS AND DISCUSSION

4.3.1 *Two-layer sample reconstruction*

As a first demonstration of POCT, a custom-made two-layer sample has been measured, which consists of metal structures axially separated by a layer of

transparent polymer. Fabrication details of the sample can be found in h.3. A 3D representation of the sample is shown as part of the setup schematic in Fig. 4.2, and Fig. 4.7(a) shows the optical microscope image of the sample.

In POCT, data is recorded using an integration time of 1 ms per exposure, using an average power on the sample of 2.2 µW per wavelength. We use $N = 51$ wavelengths ranging from 708.8 nm to 802.8 nm and $M = 201$ transverse scan positions. we use structured probe beams as illumination, which are created by masking the iris in the setup with a piece of scotch tape. Single-slice ptychography reconstructions are performed wavelength by wavelength. Figures 4.4(a,b) show the reconstructed object and beam at the shortest wavelength of 708.8 nm. As can be seen in Fig. 4.4(c), in total 600 iterations are performed for each wavelength. Figures 4.4 (d-k) show reconstructions at four other wavelengths. The probe beams have a diameter of around 700 µm.

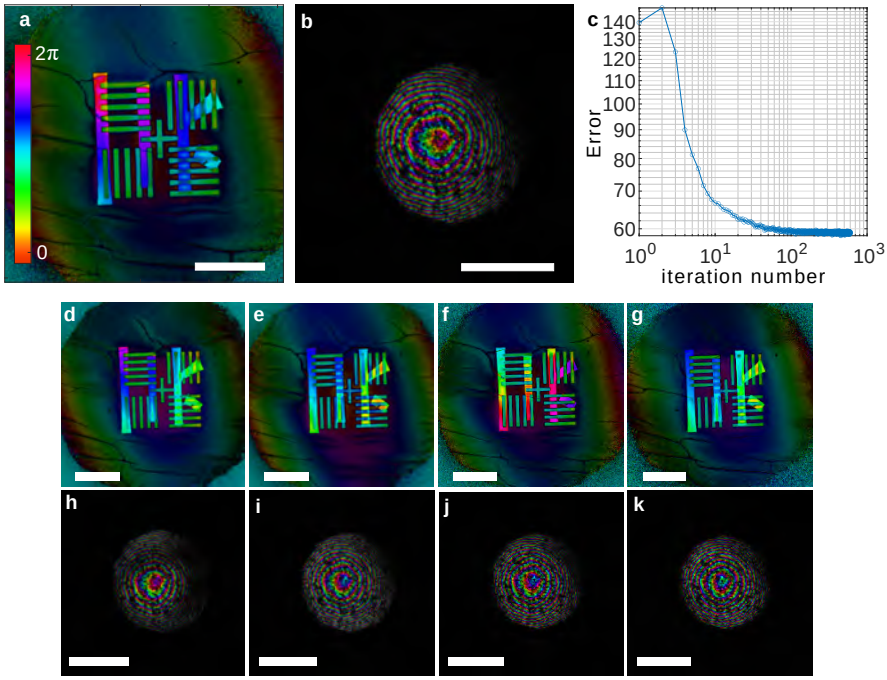

Figure 4.4: Single-wavelength reconstruction results for the two-layer sample. (a-c) Reconstructed object, probe, and error at 708.8 nm. (d-k) Reconstructed objects and probes at four wavelengths $\lambda = 740.5, 775.1, 813.0, 802.8$ nm, respectively. The scale bars are 500 µm. The colorbar in (a) is shared among all the figures.

The sample-detector distance calibrated by zPIE [150] is 38.6 mm. At the shortest wavelength of 708.8 nm and with the detection NA of 0.085, the lateral resolution is $\lambda_{\max}/2\text{NA} = 4.7$ µm and the DoF is 240 µm. The optical sectioning resolution Δz_{opt} based on Eq. 4.1 is 6 µm, resulting in a depth resolution of 2 µm, an improvement over conventional ptychography by two orders of magnitude.

Image scaling and registration

As mentioned in the methods, the object pixel size is dependent on the wavelength since Fraunhofer propagation [38] is used in the ptychographic reconstruction. As shown in Figs. 4.5(a,b), the object at 802.8 nm is smaller than the one at 708.8 nm. Also, due to the ambiguity of the absolute lateral position of the object in ptychography, reconstructed images at different wavelengths are misaligned as shown in Fig. 4.5(d), where we take the difference between two reconstructed amplitudes. To properly align them, we calculate and correct for the lateral shifts based on the amplitude images with sub-pixel resolution using the image registration algorithm in Ref, [151]. In Fig. 4.5(c) we show the rescaled and registered object at 802.8 nm, and the difference in amplitude between the two wavelengths is shown in Fig. 4.5(e), which confirms the alignment.

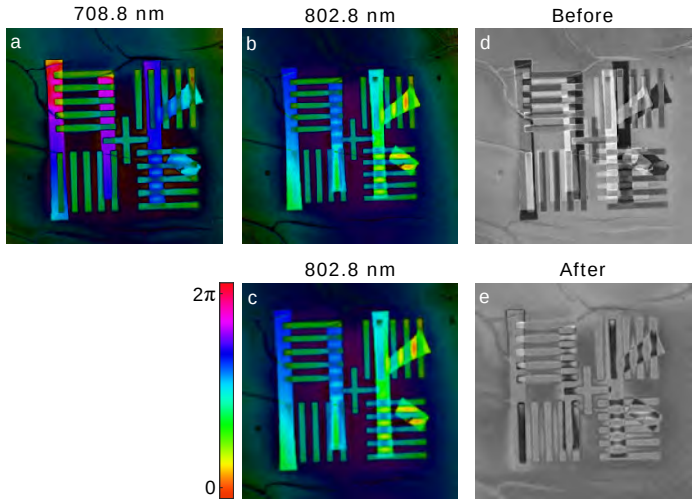

Figure 4.5: Results of image scaling and registration. (a,b) Reconstructed complex-valued object at the shortest wavelength $\lambda = 708.8$ nm and the longest wavelength $\lambda = 802.8$ nm, respectively. (c) The resulted object at 802.8 nm after scaling and image registration. (d,e) The difference between the reconstructed amplitudes at the two wavelengths before and after scaling and image registration.

Phase synchronization and the dispersion effect

We show the total depth distribution of the two-layer sample without the phase synchronization in Fig. 4.6(a), where three peaks are observed at -32.8 µm, 0 µm, and 32.8 µm, respectively. The corresponding tomographic slices are shown in Figs. 4.6(b-d), respectively, where we can see that the structures of the two layers of the sample are mixed. For comparison, we show the results with the phase synchronization step in Figs. 4.6(e-h), where two peaks are observed at -32.8 µm, 0 µm with higher contrast, and the corresponding slices in Figs. 4.6(f,g) show a

successful separation of the two layers. Additionally, as the chosen reference pixel is from the top layer, we can see that due to dispersion the peak for the bottom layer at −32.8 µm is wider than the one at 0 µm. We fit a double Gaussian model to the data (dashed curve in Fig. 4.6(e)), from which we obtain full width at half maximum values of 2.4 µm and 1.4 µm, respectively.

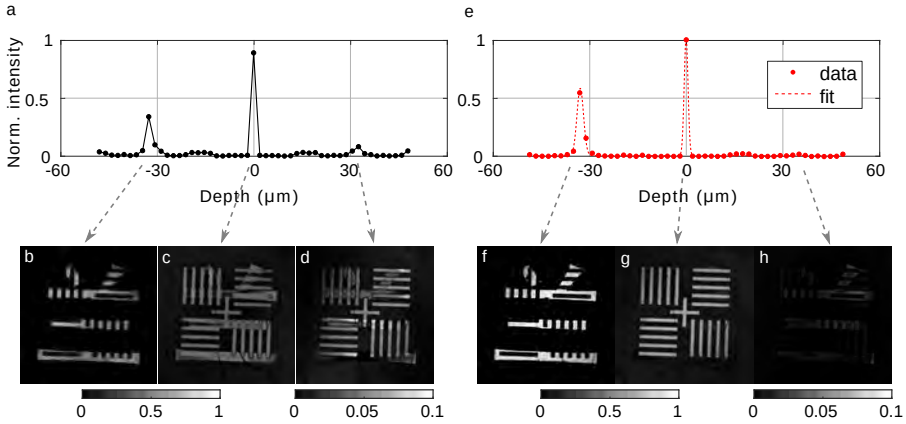

Figure 4.6: Results of depth reconstruction without (a-d) and with (e-h) the phase synchronization. (a,e) Total depth distribution of the two-layer sample summed over all the pixels transversely. The plots are normalized to the maximum of the signal (in e) with the phase synchronization step. The dashed curve is a double Gaussian fit.

The resolved tomograms of the top and the bottom layers are shown in Fig. 4.7(b) and (c) respectively. Figure 4.7(d) shows three depth plots at three locations marked in Fig. 4.7(b) and (c) respectively. The phase synchronization was performed at location 1. The width of the peaks shows that the expected depth resolution of 2 µm is indeed achieved. We do observe a slight broadening of the peak at location 2, which is caused by material dispersion of the spacer layer. Phase synchronization at location 2 would have led to a spectrum-limited resolution at this depth, and more advanced numerical dispersion compensation should enable depth-independent resolution. Because phase retrieval provides complex-valued information rather than interferometric intensity measurements, the depth sections in Fig. 4.7(d) largely suppress any autocorrelation artefacts or complex conjugate signals common to spectral domain OCT. The lateral resolution is evaluated by calculating the Fourier ring correlation (FRC) [153] of two object intensities reconstructed from the shortest (708.8 nm) and longest wavelengths (803.8 nm), and the 1/2-bit resolution criteria [154] is used. In Fig. 4.7(e), the object correlation curve (solid line) is above the 1/2-bit threshold (dashed line) across the detected spatial frequency spectrum, meaning that the two independent reconstructions are consistent up to the Nyquist frequency. Thus the measured half-period lateral resolution in our lensless setup is confirmed to be at the diffraction limit of 4.7 µm.

An advantage that ptychography brings to OCT is the ability to deconvolve the probe from the object image. Coherent speckle noise is thus almost completely eliminated, and the resulting images in Figs. 4.7(b,c) are free of typical coherent

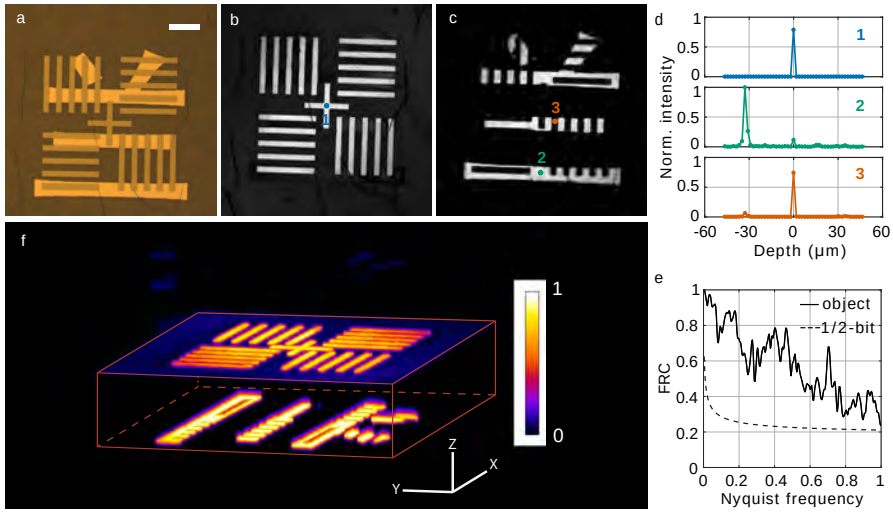

Figure 4.7: (a) Bright-field optical microscope image of the sample. (b),(c) Reconstructed tomograms of the top and bottom layers of a two-layer sample. The bottom layer structure shows shadows of the opaque metal structures above. (d) Reconstructed depth response at three locations marked in (b) and (c). (e) Solid line: Fourier ring correlation (FRC) between object intensities reconstructed at the shortest (708.8 nm) and longest (802.8 nm) wavelengths. Dashed line: the 1/2-bit resolution curve. (f) 3D rendering of the reconstruction, showing the layer separation. The colorscale shows the normalized intensity (linear scale). The distance in the z-direction is increased by a factor of 4 compared to the x- and y-direction. A multi-angle projection of this 3D reconstruction is shown in Supplementary Movie S1 in Ref [155].

imaging artefacts caused by imperfections in the optical system. A 3D rendering of the sample is shown in Fig. 4.7(f). As depicted in Fig. 4.2, the top layer is the metal/air or polymer/air interface, and the bottom layer has metal structures at the polymer/glass interface with matching refractive index. A 3D visualization video is available online (Supplementary Movie S1 in Ref [155]).

4.3.2 *Mouse brain sample reconstruction*

In a second experiment, a cryo-cut unstained mouse brain slice with a nominal thickness of 40 µm has been measured using POCT. This mouse brain sample has continuous axial structures. A low-resolution, bright-field, reflection optical microscope image of the sample is shown in Fig. 4.9(a). A high-NA objective is used in the microscope to focus on the top and the bottom layer of the sample, images of which are shown in Figs. 4.9(b) and 4.9(c). In the experiment, the sample is measured with $N = 49$ wavelengths ranging from 708.8 nm to 851.3 nm at $M = 201$ scan positions. A smooth beam with 0.6 mm diameter is used (see Fig. 4.8), and the camera integration time is set to 3 ms per exposure. The average power on the sample is 5 µW per wavelength.

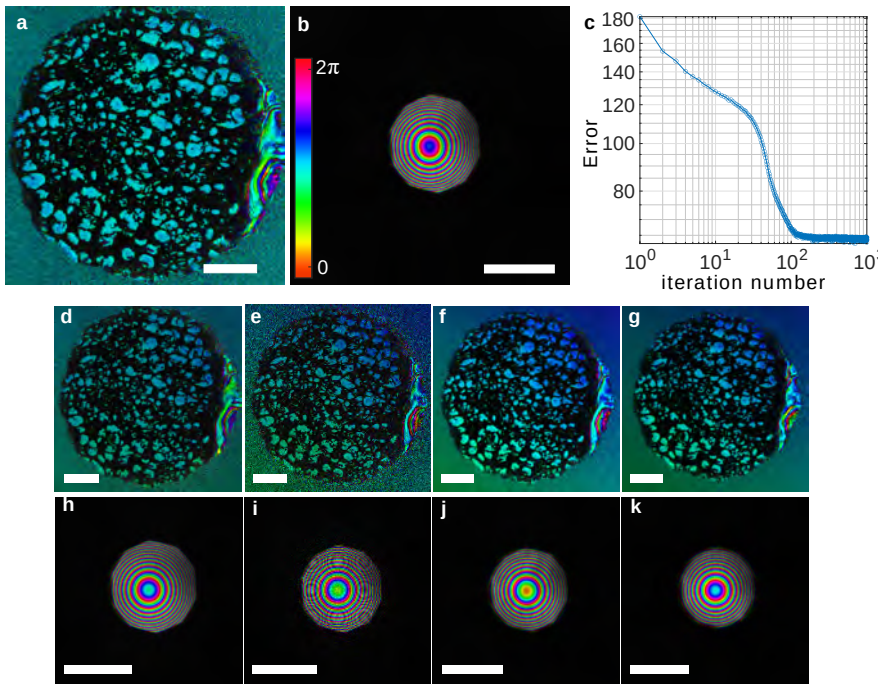

Figure 4.8: Single-wavelength reconstruction results for the mouse brain sample. (a-c) Reconstructed object, probe, and error at 708.8 nm. (d-k) Reconstructed objects and probes at four wavelengths $\lambda = 740.5, 775.1, 813.0, 851.3$ nm, respectively. The scale bars are 500 µm. The colorbar in (b) is shared among all the figures.

Examples of ptychographic reconstructions of the objects and probes at five different wavelengths are shown in Fig. 4.8. 1000 iterations are taken for each reconstruction. The optical sectional resolution Δz_{opt} is 4.3 µm. The calibrated propagation distance from the object to the detector is 25.4 mm, resulting in a detection NA of 0.12, a lateral half-period resolution of 3 µm, and a DoF of 106 µm. Figure 4.9(d) shows the reconstructed tomogram of the deepest layer of the mouse brain tissue, where the bright areas indicate the air/glass substrate interface and the dark areas indicate the brain/glass interface. A tomogram of an upper layer of the sample is shown in Fig. 4.9(e), where the bright areas are ridges of the mouse brain tissue that correspond to the sharp structures in Fig. 4.9(b). Using an averaged value of $n = 1.38$ for the refractive index of mouse brain tissue across the full wavelength range [156], we obtain a value for the thickness of the mouse brain of 20 µm with a depth resolution of 1.6 µm. Figure 4.9(f) shows a color-coded height plot of the reconstructed sample, where for each pixel the height is chosen at the maximum intensity location along the z direction. Figure 4.9(g) shows a 3D rendering of the reconstructed mouse brain sample. A 3D visualization video is available online (Supplementary Movie S2 in Ref [155]).

With the two-layer and mouse brain samples, we demonstrate that POCT successfully performs depth-resolved imaging, where the lateral and axial resolutions are decoupled. This shows that POCT has a great potential for 3D high-resolution imaging. Compared to OCT, POCT does not rely on an external reference and it deconvolves the illumination from the object reconstruction. Therefore POCT does not suffer from reference- and illumination-induced artefacts. Additionally, the current setup only contains a beamsplitter between the object and the camera, thus the reconstruction results (Figs. 4.7(b, c) and Figs. 4.9(d, e)) are almost free of typical coherent imaging artefacts ('speckle') caused by imperfections in optical systems.

One advantage of POCT over CT-based 3D imaging techniques [20, 91, 137, 140] is speed. Firstly, wavelength scanning is faster than mechanical stage rotation, as our acousto-optic scanning method enables sub-ms wavelength switching times, and fast cameras achieve multi-kHz update rates. Secondly, computational complexity is reduced, as POCT only requires a series of 2D reconstructions plus a phase synchronization step, and the correlation between different-wavelength images provides a strong initial guess for both object and probe after a first reconstruction at a single wavelength, ensuring fast convergence. Furthermore, no image stitching algorithms are needed. Lastly, as the phase synchronization is achieved numerically, no phase-stable optical path is needed.

In addition to the present swept-source implementation of POCT, the concept can be extended to other methods in which wavelength-resolved diffraction data is measured, such as Fourier-transform-based diffractive imaging [29, 157] or computational time-domain OCT [158].

Going beyond the present proof-of-concept, various improvements can still be envisaged. One clear limitation of POCT is the absence of coherent amplification by a strong reference wave. We therefore envision the main applications of POCT in material science and lithographic device inspection, where photon flux on sample is not the limiting factor, or in situations where the generation of a reference beam is challenging such as with extreme ultraviolet radiation. While in the lensless

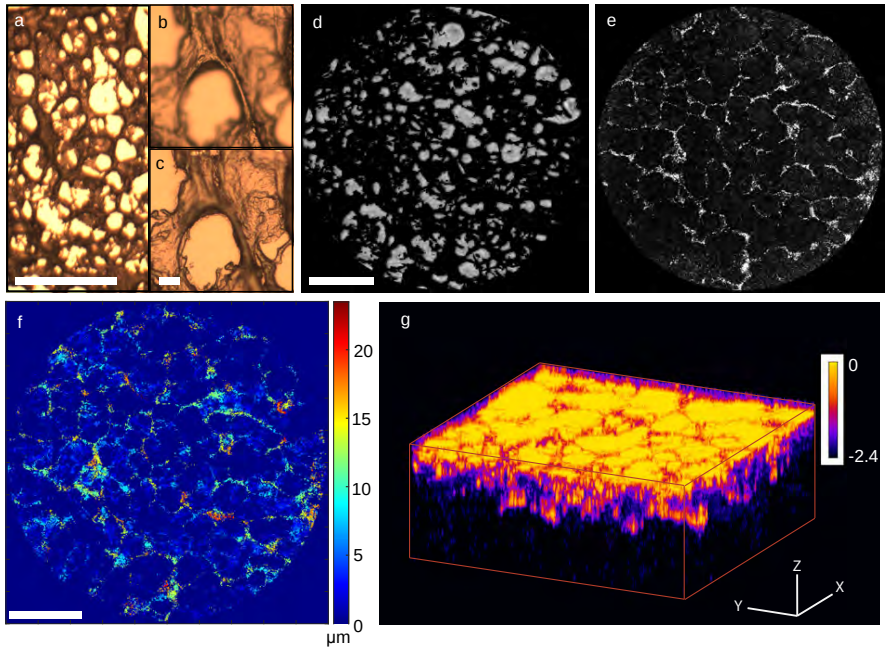

Figure 4.9: (a) Low-NA (0.13/5x) optical microscope image of the mouse brain sample. Scale bar is 500 µm. (b),(c) High-NA (0.45/50x) optical microscope images of the mouse brain sample focused at the top and bottom structures respectively. Scale bar is 20 µm, shared between (b) and (c). (d) Reconstructed tomogram of the bottom layer of the mouse brain sample (the air/glass (bright) or the mouse brain/glass (dark) interface). (e) Reconstructed tomogram of the top layer of the sample (the air/mouse brain interface). Scale bar is 500 µm, shared between (d) and (e). (f), Color-coded height map of the mouse brain sample. Scale bar is 500 µm. (g) 3D rendering of part of the reconstructed mouse brain. The colorscale shows the logarithm of the normalized reflectivity. A magnification factor 4 was applied in the z direction. A rotating projection of this 3D reconstruction is shown in Supplementary Movie S2 in Ref [155].

geometry the NA is limited by the sample-detector distance and detector size, the use of high-NA optics can yield a significant transverse resolution improvement. In addition, the axial imaging range is currently limited to the single-layer projection limit in ptychography, which is typically in the order of tens or hundreds microns at optical wavelengths. In principle, multi-slice ptychography [90, 134–136] can be applied to extend this limit. Moreover, the current POCT implementation has not taken sample dispersion into account, which may be possible through adaptive optics [33]. Finally, although single-layer ptychography could handle multiple scattering to a certain degree, more sophisticated forward modeling in ptychography is required to apply POCT on highly scattering samples in reflection.

4.4 CONCLUSION

We have introduced POCT as a new concept for high-resolution 3D optical imaging. POCT successfully combines advantages of OCT and ptychography, decouples the lateral and axial resolution while maintaining a large FoV, and requires only a single viewing direction. Using a straightforward lensless imaging setup without the need for interferometric reference, we demonstrate a diffraction-limited μm-level 3D image resolution with both discrete and continuous samples. Further improvements to this new imaging modality are clearly possible, and we believe that the POCT concept has great potential as a simple yet robust 3D imaging method, especially on planar nanostructures mounted on wafers, as is commonly found in modern-day nanotechnology.

5

TOWARDS 3D PTYCHOGRAPHY

ABSTRACT

In ptychography, redundant information is collected by scanning a probe transversely across an object in overlapping regions. This allows for more unknown quantities to be robustly recovered along side the 2D object itself, including 2D complex illumination functions [78], coherence modes of the illumination [159], and spectral content of the illumination together with spectral response of the object [160]. This raises the question if a 3D object function can be recovered in a similar fashion. It has been shown that a 3D transmission function of an object indeed can be reconstructed using a multislice approach [89], which computationally segments a thick object axially into a stack of 2D slices, and recovers both the illumination and object slice by slice. However, multislice ptychography is tailored to transmission measurements where only forward propagation is considered, which limits its suitability for solving image reconstruction in a reflection geometry. In this chapter, we explore a different approach that is applicable to both transmission and reflection ptychography. We start by considering weakly scattering objects, for which the first Born approximation can be applied. A 3D ptychography forward model is presented and reconstruction results from simulation are shown and discussed.

5.1 EWALD'S SPHERE

The concept of the Ewald's sphere was originally introduced in crystallography to study and understand reciprocal lattices in order to analyze crystalline structures [23, 161]. Later it became a useful tool in diffraction tomography [82, 133, 162, 163], where measurements are performed in the reciprocal (or Fourier) space and Ewald's sphere reconstruction offers a straightforward geometrical perspective for achieving high resolution 3D image reconstructions [164].

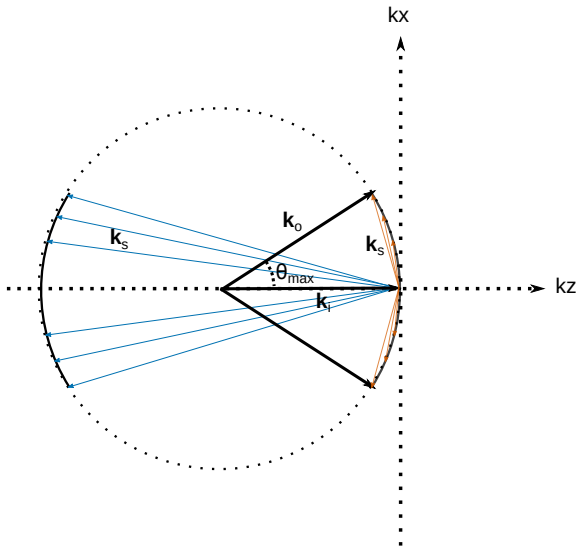

Figure 5.1: Ewald's sphere in 2D projection: $\mathbf{k_i}$ represents a plane wave incidence, θ_{max} is the maximum detection angle, $\mathbf{k_s} = \mathbf{k_o} - \mathbf{k_i}$ is the scattered wavevector. In transmission, relatively low spatial frequencies in k_z (orange) are detected, and in reflection, relatively high spatial frequencies in k_z (blue) are detected.

Here we introduce Ewald's sphere as shown in Fig. 5.1, where a plane wave illumination of a given wavelength λ and direction $\overrightarrow{\mathbf{s_z}}$ is represented by the wave vector $\mathbf{k_i} = \frac{2\pi}{\lambda}\mathbf{s_z}$ in Fourier space. Depending on the detection NA, or equivalently the maximum detection angle θ_{max}, the measurable outgoing wavevectors end up on a shell of a sphere with a radius of $\frac{2\pi}{\lambda}$, namely Ewald's sphere. The 2D projection of Ewald's sphere is shown as a dashed circle in Fig. 5.1. Connecting the origin of the coordinate system with the sphere gives the scattered wavevectors $\mathbf{k_s}$ which reveal the spatial frequencies of the object. As can be seen in Fig. 5.1, forward scattering contains low spatial frequencies in k_z(orange) which can be detected in transmission, and backward scattering contains high spatial frequencies in k_z (blue) which can be detected in reflection [162]. Given by the Fourier transform relation, the detection range in Fourier space determines the imaging resolution in real space. The detectable shell of Ewald's sphere naturally has a smaller extent in k_z than in k_x and k_y, and this offers an intuitive way to

understand the achievable resolution differences in the lateral and axial directions in conventional microscopy.

Ideally, if we can measure the 3D distribution of the scattered field in the Fourier space, a direct Fourier transform would solve for the 3D scattering potential (or the complex refractive index) of an object. In practice, a 2D detector only measures a limited shell inside the 3D Fourier space. Generally there are two ways to cover more area in the Fourier space in order to achieve 3D imaging: one is to increase the illumination angle by either rotating the incident beam or the object itself as in diffraction tomography, and the other way is to use different wavelengths [162, 163] as in computational OCT. Note that extending the range of illumination angles or wavelengths has a different effect in transmission and reflection detection, which is summarized in Fig. 5.2. Figure 5.2(a) shows that changing the illumination angle is equivalent to shifting the center of Ewald's sphere on the small sphere S_1, and the detectable fraction of the sphere (in orange) correspondingly shifts around. Since all shifted spheres go through the origin, the total detectable region forms an elongated donut-like shape, and in the center the lack of information gives rise to the missing cone problem in diffraction tomography [165]. For comparison, Fig. 5.2(b) shows the case of changing illumination wavelength in transmission, where different wavelengths correspond to a different sphere. Note that dispersion is not represented here. Shorter wavelengths correspond to spheres with larger radii. With the same detection NA, shorter wavelengths cover a larger area in Fourier space, and thus lead to higher reconstruction resolutions. Different illumination wavelengths probe similar information, as all the detectable regions collapse to the zero spatial frequency of the scattering object as shown in Fig. 5.2(b). Figure 5.2(c) and (d) show the effects of changing illumination angle and wavelength in reflection, respectively. As can be seen, changing illumination wavelengths in a reflection geometry (Figure 5.2(d)) extends the coverage in k_z effectively, which gives the advantage of increasing the depth resolution. Figure 5.2(e) and (f) show the combination of transmission and reflection detection for the cases of extended illumination angles and wavelengths. In conclusion, with a fixed detection NA, varying illumination angle improves the axial resolution more effectively in transmission and extending illumination wavelength improves the axial resolution more effectively in reflection. A complete way to cover the Fourier space is to measure in both transmission and reflection geometries and by utilizing both angular and spectral diversities as shown in Fig. 5.2(g).

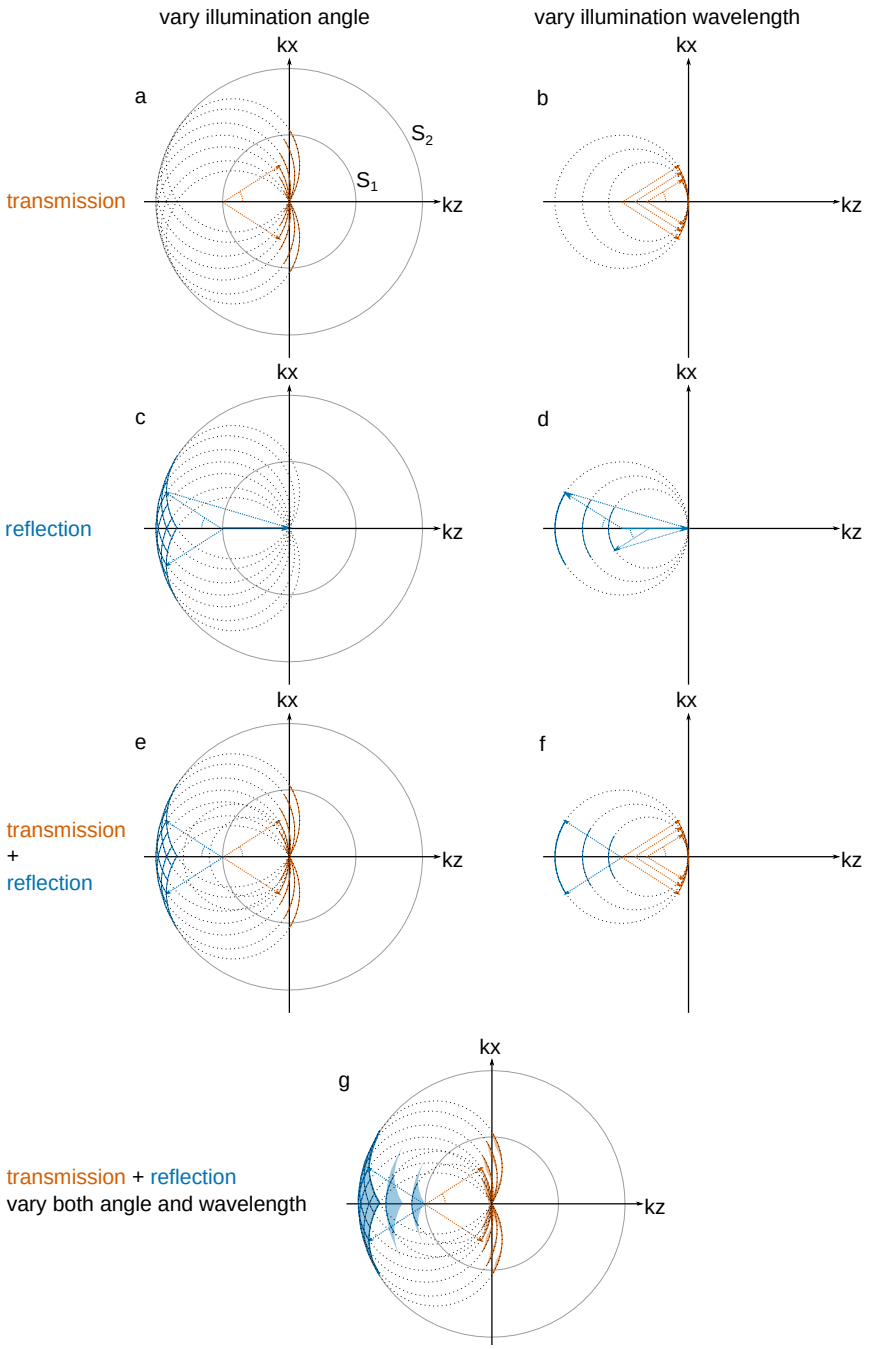

Figure 5.2: Ewald's sphere reconstructions. (a)(b) In transmission, varying illumination angles and wavelengths respectively. (c)(d) In reflection, varying illumination angles and wavelengths respectively. (e)(f) Combining transmission and reflection, varying illumination angles and wavelengths respectively. (g) Vary both illumination and wavelength, and combine transmission and reflection measurements

5.2 FIRST BORN APPROXIMATION

When considering a weakly scattering object of a finite volume (see Fig. 5.3), whose spatially dependent complex refractive index $n(\mathbf{r}')$ only slightly deviates from the refractive index of the environment n_b, the wavefield $\psi(\mathbf{r}')$ inside the scattering volume satisfies the inhomogeneous wave equation [133]:

$$(\nabla^2 + k_0^2 n^2(\mathbf{r}'))\psi(\mathbf{r}') = 0, \tag{5.1}$$

where $k_0 = \frac{\omega}{c}$ is the wavenumber in vacuum. The total wavefield can be expressed as a sum of the incident field and the scattered field:

$$\psi(\mathbf{r}') = \psi_i(\mathbf{r}') + \psi_s(\mathbf{r}'), \tag{5.2}$$

where the incident field satisfies the homogeneous wave equation as the scattering object is absent:

$$(\nabla^2 + k_0^2 n_b^2)\psi_i(\mathbf{r}') = 0. \tag{5.3}$$

Subtracting Eq. 5.3 from Eq. 5.1 and rearranging, we obtain the following differential equation for the scattered field:

$$(\nabla^2 + k^2)\psi_s(\mathbf{r}') = -4\pi O(\mathbf{r}')\psi(\mathbf{r}'), \tag{5.4}$$

where $k = k_0 n_b$ is the wavenumber of the surrounding medium, and $O(\mathbf{r}')$ is the scattering potential of the object:

$$O(\mathbf{r}') = \frac{k_0^2}{4\pi}(n^2(\mathbf{r}') - n_b^2). \tag{5.5}$$

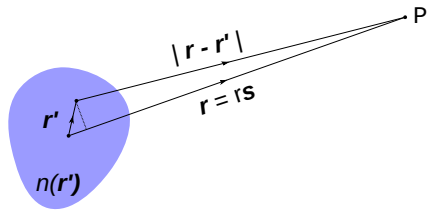

Figure 5.3: A weakly scattering 3D object with a refractive index of $n(\mathbf{r}')$. $\mathbf{r}'$ represents the object coordinates and $\mathbf{r}$ represents the observation coordinates.

To solve for the scattered field in Eq. 5.4, the free-space Green's function $G(\mathbf{r} - \mathbf{r}') = \frac{e^{ik|\mathbf{r}-\mathbf{r}'|}}{|\mathbf{r}-\mathbf{r}'|}$ is used. It describes an outgoing scalar field scattered by a point object, which follows the wave equation $(\nabla^2 + k^2)G(\mathbf{r} - \mathbf{r}') = -4\pi\delta(\mathbf{r} - \mathbf{r}')$. Using the Green's function, the scattered field outside the scattering object can be expressed as [133]:

$$\psi_s(\mathbf{r}) = \int G(\mathbf{r} - \mathbf{r}')\psi(\mathbf{r}')O(\mathbf{r}')d\mathbf{r}', \tag{5.6}$$

which essentially is a convolution of the Green's function, and the product of the object function and the incident field. Applying a 2D Fourier transform on both sides of Eq. 5.6, we arrive at:

$$\tilde{\psi}_s(\mathbf{k}) = \tilde{G}(\mathbf{k})\{\tilde{\psi}(\mathbf{k}) \star \tilde{O}(\mathbf{k})\}, \tag{5.7}$$

where $\mathbf{k} = \mathbf{s}k$ is the wave vector, $\mathbf{s}$ is a unit vector (see Fig. 5.3). Under the far-field approximation ($kr \to \infty$), the Green's function can be simplified as:

$$G(\mathbf{r} - \mathbf{r}') = \frac{e^{ik|\mathbf{r}-\mathbf{r}'|}}{|\mathbf{r} - \mathbf{r}'|} \sim \frac{e^{ikr}}{r} e^{-i\mathbf{k}\cdot\mathbf{r}'}. \tag{5.8}$$

Thus the far-field scattered wavefield can be expressed as:

$$\begin{aligned} \psi_s(\mathbf{r}) &= \frac{e^{ikr}}{r} \int \psi(\mathbf{r}')O(\mathbf{r}')e^{-i\mathbf{k}\cdot\mathbf{r}'} d\mathbf{r}' \\ &= \frac{e^{ikr}}{r} \mathcal{F}^3\{\psi(\mathbf{r}')O(\mathbf{r}')\}, \end{aligned} \tag{5.9}$$

where $\mathcal{F}^3$ represents a 3D Fourier transformation. For a weakly scattering sample, where the scattered field can be considered as a small perturbation of the incident field, the Born approximation can be applied [133]. Under the first Born approximation, the total wavefield $\psi(\mathbf{r}')$ in Eq. 5.9 is replaced by the incident wave $\psi_i(\mathbf{r}')$, and the far-field scattered wave becomes:

$$\psi_s(r\mathbf{s}) = \frac{e^{ikr}}{r} \mathcal{F}^3_{\mathbf{r}'\to\mathbf{s}}\{P(\mathbf{r}')O(\mathbf{r}')\}, \tag{5.10}$$

where $P(\mathbf{r}') = \psi_i(\mathbf{r}')$ is the incident wavefield or probe function as often used in ptychography. Equation. 5.10 shows that according to the first Born approximation, the far-field scattered field corresponds to a 3D Fourier transform of the product of the probe and the object function. This relation has been used in diffraction tomography, where plane wave illumination is often required. If the probe field consists of plane waves, the far-field scattered field is directly linked to the Fourier transform of the scattering potential of the object. Using interferometric detection, both the phase and intensity of the diffraction pattern can be measured. In order to obtain a 3D reconstruction, angular scans and numerical stitching are required which is often time consuming. Here we propose to utilize ptychography to directly reconstruct a 3D object from a single viewing angle, without the need of interferometric detection. Since ptychography is able to deconvolve the probe and object from the measurements, the requirement of plane wave illumination can also be eliminated. This means structured illuminations can be adopted to increase the illumination NA, which in turn can improve the depth sectioning capability from a single-view measurement (This argument is supported in Sec. 5.1).

5.3 THE 3D FORWARD MODEL

To perform 3D ptychography, we take the same measurement scheme as in 2D ptychography, where the probe is scanned transversely with respect to a 3D object,

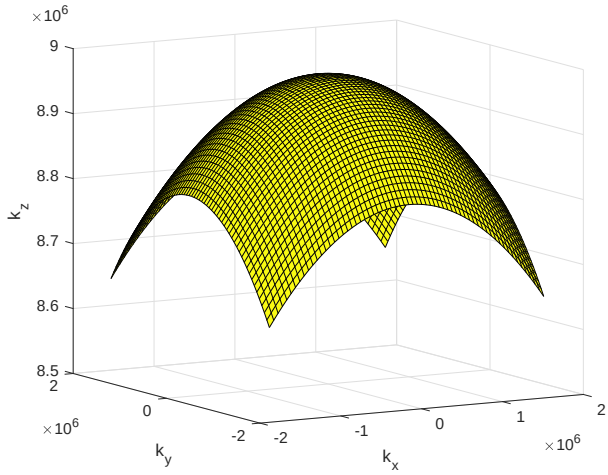

Figure 5.4: The measured spherical shell in the 3D Fourier space given by $k_z^2 = k^2 - k_x^2 - k_y^2$.

and 2D diffraction patterns are recorded at each scan position denoted by j. When a planar detector records a diffraction intensity pattern in the far-field, only a fraction of the 3D diffraction data in the reciprocal space can be measured. As shown in Fig. 5.4, due to the mapping relation between the 3D reciprocal k space and the far-field real space, the measured data corresponds to a part of a sphere[1] given by $k_z^2 = k^2 - k_x^2 - k_y^2$. Thus the forward model in the 3D implementation becomes:

$$I_j(k_x, k_y, k_z) = |\mathcal{F}^3\{P(\mathbf{r})O(\mathbf{r} - \mathbf{R}_j)\}|^2\Big|_{k_z = \pm(k^2 - k_x^2 - k_y^2)^{\frac{1}{2}}}, \tag{5.11}$$

where $\mathbf{R}_j$ is the translation vector, k_x and k_y are the spatial frequencies (as in Eq. 2.23) determined by the detector size and position. With this approach, both transmission and reflection cases can be described: in transmission k_z takes positive values, and in reflection k_z takes negative values.

We modified the original ePIE algorithm to perform 3D reconstructions. The general workflow remains the same as shown in Fig. 2.7. The update rules also have the same form (see Eq. 2.48):

$$\begin{aligned} O_j^*(\mathbf{r}) &= O_j(\mathbf{r}) + \beta_o \frac{P_j^*(\mathbf{r})}{max|P_j(\mathbf{r})|^2}(\psi_j'(\mathbf{r}) - \psi_j(\mathbf{r})) \\ P_j^*(\mathbf{r}) &= P_j(\mathbf{r}) + \beta_p \frac{O_j^*(\mathbf{r})}{max|O_j(\mathbf{r})|^2}(\psi_j'(\mathbf{r}) - \psi_j(\mathbf{r})), \end{aligned} \tag{5.12}$$

except that the object $O_j(\mathbf{r})$, probe $P_j(\mathbf{r})$, and exit wave functions $\psi_j(\mathbf{r})$ are all three-dimensional. One main modification is in the application of the intensity

1 We note that this sphere is different from the Ewald's sphere introduced in Sec. 5.1, because the illumination function is not limited to plane waves and the reciprocal space is not shifted with respect to the incident wavevector.

constraint, where in the 2D case the estimated amplitude of $\tilde{\psi}_j(\mathbf{q})$ is replaced by the measured amplitude $\sqrt{I_j(\mathbf{q})}$ (see Fig. 2.7). In the 3D case, as explained in Eq. 5.11, only part of the sphere inside the 3D Fourier space of the function $\tilde{\psi}_j(\mathbf{k})$ is updated by the measured 2D amplitude $\sqrt{I_j(\mathbf{k})}$.

5.4 SIMULATION RESULTS

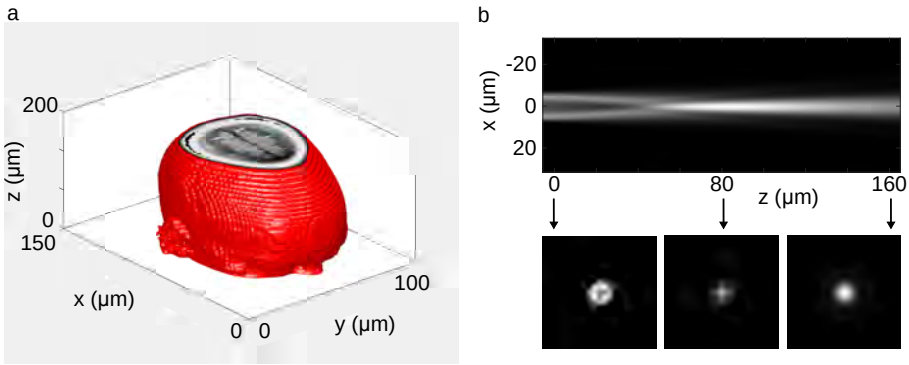

Figure 5.5: (a) A 3D plot of the object used in the simulation. An MRI dataset available from Matlab [166] is rescaled to form the simulated object. (b) Intensity plots of a 3D probe formed by propagating a Gaussian beam through an aperture.

To verify the 3D model, we simulate a ptychographic experiment in the reflection geometry. An MRI dataset of a human cranium available from Matlab [166] is used as the 3D object as shown in Fig. 5.5(a). The simulated object has a total thickness of 170 μm, consisting of 9 different layers with an axial separation of 21 μm. The 3D probe used to scan the object is shown in Fig. 5.5(b). The simulated illumination wavelength is 700 nm and the detection NA is 0.19, which together lead to a transverse resolution of 1.8 μm and an axial resolution (DoF) of 19 μm. 201 diffraction patterns are simulated with a Fermat scanning pattern and an averaged overlap factor of 80%.

We start the reconstruction with the correct probe and an object filled with ones as initial guesses, and allow both to be updated by the algorithm. After 1500 iterations, the algorithm converges and the reconstructed object is plotted in Fig. 5.6. Nine slices in z with a separation of 21 μm are successfully reconstructed.

The simulation results show that it is promising to reconstruct a 3D weakly scattering object using the modified 3D ptychography method. Future work needs to be carried out to test the method with real experimental data. As mentioned previously, the correct 3D probe function is used as the initial guess in the simulation. This can also be done in practice, where a 2D probe can be pre-calibrated and numerically propagated to form a 3D initial guess. Although a smooth beam is used in the simulation, in principle, structured beams are preferred. As we have

shown in the 2D case, structured beams offer better reconstruction resolution (see Sec. 2.3.4), which would also improve the depth sectioning in 3D reconstructions.

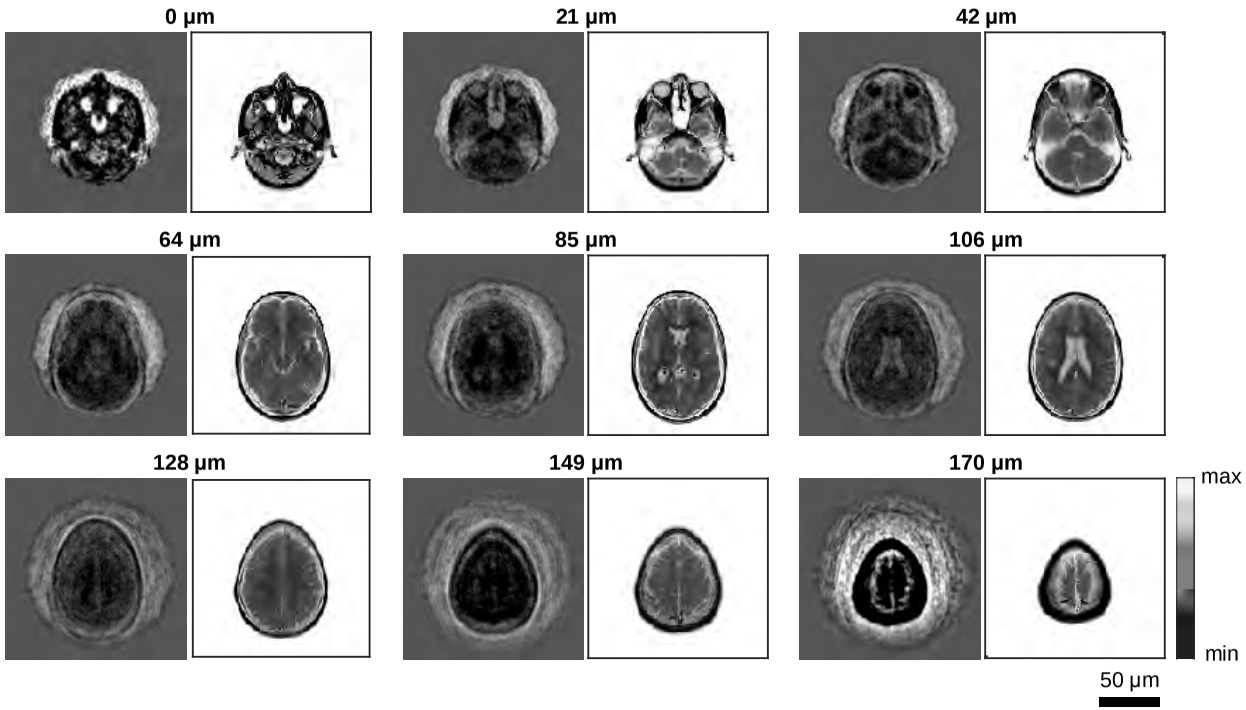

Figure 5.6: A comparison of the reconstruction (left) and ground-truth (right) of nine tomographic images at different depths with a separation of 21 µm.

Part II

COMPUTATIONAL-IMAGING-BASED METROLOGY

6

MEASURING LASER BEAM QUALITY, WAVEFRONTS, AND LENS ABERRATIONS USING PTYCHOGRAPHY

ABSTRACT

We report on an approach for quantitative characterization of laser beam quality, wavefronts, and lens aberrations using ptychography with a near-infrared supercontinuum laser. Ptychography is shown to offer a powerful alternative for both beam propagation ratio M^2 and wavefront measurements compared with existing techniques. In addition, ptychography is used to recover the transmission function of a microlens array for aberration analysis. The results demonstrate ptychography's flexibility in wavefront metrology and optical shop testing.

A research article based on this chapter has been published as: "Du, M., Loetgering, L., Eikema, K.S.E. & Witte, S. Measuring laser beam quality, wavefronts, and lens aberrations using ptychography. *Optics Express* **28**, 5022-5034 (2020)."

6.1 INTRODUCTION

Controlling the shape of laser beams has been an enabling technology for advances in physics, chemistry, and biology. Gaussian and top-hat spatial profiles are typically encountered in applications where laser beams need to be focused to very small areas, such as laser cutting, laser-produced plasma, and high-harmonic generation [167–169]. The focusability of a laser beam is specified by the beam propagation ratio (BPR), often referred to as M^2 [170, 171]. It indicates how tight a laser beam can be focused compared with a diffraction limited Gaussian beam (TEM_{00}) at the same wavelength. Commercial M^2-measurement devices perform beam caustic measurements by translating a pixelated sensor through the focus of a laser beam along the beam propagation direction. Following a fitting procedure, M^2 can be extracted. However, this method is only applicable to stigmatic beams and simple astigmatic beams with fixed principle axes, but not for general astigmatic beams [172]. This means a priori knowledge or assumptions are necessary when applying the M^2-characterization to a laser beam, which limits its application or leads to inaccurate results in cases where incorrect assumptions are applied. In contrast to applications where focusability is important, other applications require highly structured, non-smooth wavefronts. Twisted beams and tailor-made wavefronts can be used in optical tweezers to impart orbital angular momentum or control the trajectory of microparticles [173–175].

Engineering high-quality wavefront shaping devices requires accurate wavefront metrology tools. For smooth wavefronts, the Hartmann-Shack wavefront sensor (HSWFS) is a convenient choice [176]. Here typically a pinhole or microlens array is used to monitor the gradient of the wavefront. From this information the actual shape of the wavefront can be computed up to a constant phase offset. HSWFSs require only a single measurement and can operate at multiple wavelengths [177]. However, disadvantages include the typically low spatial resolution, which is limited by the spacing of its resolving elements. Thus the application of HSWFSs is restricted to wavefronts that vary on spatial length scales larger than the characteristic unit cell of the microlens or pinhole arrays involved. This typically results in a spatial resolution of several tens or hundreds of micrometers in the x-ray and visible range, respectively. Furthermore, singular beams such as Laguerre-Gaussian beams with non-zero topological charge and speckle beams are challenging for HSWFSs, in particular when two singularities enter the same subaperture [178]. An alternative is offered by holographic wavefront sensing methods [179]. While offering superior spatial resolution, typically limited by either the detector pixel size or numerical aperture depending on the experimental geometry, holography requires highly coherent beams, which can be a limiting factor for any application involving sources with limited spatial or temporal coherence. Among other approaches, defocus variation techniques are often applied for wavefront sensing and beam characterization [180]. These methods typically use detector defocus combined with wave propagation modelling to extract wavefront information. While such methods work well for near-Gaussian beams with limited phase variation, they have limitations for more complex beams. In particular, deterministic approaches based on the transport-of-intensity equation suffer from singular behaviour in the presence of zero-crossings and

phase vortices. Non-deterministic methods based on iterative phase retrieval can reconstruct more complex beams, but often struggle for convergence or are computationally challenging [181].

In the last decade, ptychography has emerged as both a useful microscopy and wavefront sensing tool [30, 31, 78, 93, 95, 182, 183]. In ptychography, a specimen is translated through a stationary illumination beam, referred to as the probe, and exposed at overlapping regions. The additional information provided by the overlap in scan positions enables extraction of phase information from the measured diffraction intensities. Initially developed for scanning microscopy with known illumination profile [30, 182], ptychography's capabilities were rapidly extended to simultaneous probe beam retrieval and microscopy [78, 93, 95], making it a useful tool for a variety of microscopy, wavefront sensing and optics characterization tasks [37, 184–187]. The translation diversity available in ptychography enables for both a theoretically unlimited field of view and a separation of object and illumination information. The latter provides a complex-valued 2D beam reconstruction, which offers a excellent starting point for quantitative beam quality and wavefront aberration characterization. Moreover, ptychography can deal with a wide variety of beams without any a priori knowledge, including fully coherent, spatially and temporally partially coherent, stigmatic and astigmatic beams, and is not hampered by singularities present in the beams [159, 160, 185, 187–189]. The spatial resolution achievable in ptychography can be orders of magnitude better as compared with HSWFSs. Furthermore, no reference beam is required, which makes it experimentally more convenient than holography, especially for short-wavelength radiation. A drawback of ptychography as compared with holography and HSWFSs is the requirement for sample translation, which makes the technique slower than single-shot methods.

In this chapter, we perform beam quality characterization of a near-infrared, swept-source, supercontinuum laser, using ptychography. From this analysis we extract the beam matrix, M^2 and the intrinsic astigmatism factor as a function of wavelength. The reproducibility of ptychography wavefront sensing across different samples is investigated. Secondly, we apply ptychography to detect wavefront aberrations due to misalignment, as well as lens aberrations. The recovered wavefront of an astigmatic beam and the recovered transmission function of a microlens array (MLA) are decomposed into Zernike polynomials.

6.2 QUANTITATIVE LASER BEAM QUALITY CHARACTERIZATION

6.2.1 *Wigner distribution and beam matrix*

The Wigner distribution provides a powerful mathematical description of a coherent or partially coherent laser beam [190–193]. It enables quantitative characterization of a laser beam via intensity moments [191, 194–196]. Here we use $h(x, y, u, v)$ to represent the Wigner distribution of a laser beam at a transverse plane, where (x, y) are the spatial coordinates and (u, v) are the angular coordinates. The ax-

ial coordinate z is chosen as the beam propagation direction. The zeroth-order moment describes the total power of the beam:

$$P = \int h(x,y,u,v)dxdydudv. \tag{6.1}$$

The first-order moments provide the beam centroid $(\bar{x},\bar{y})$ and propagation direction $(\bar{u},\bar{v})$:

$$\begin{aligned}
\bar{x} &= \frac{1}{P}\int h(x,y,u,v)xdxdydudv,\\
\bar{y} &= \frac{1}{P}\int h(x,y,u,v)ydxdydudv,\\
\bar{u} &= \frac{1}{P}\int h(x,y,u,v)udxdydudv,\\
\bar{v} &= \frac{1}{P}\int h(x,y,u,v)vdxdydudv.
\end{aligned} \tag{6.2}$$

The second-order moments are related to the beam width and the far-field divergence angle. In total, there are ten independent second-order moments:

$$\overline{x^k y^l u^m v^n} = \frac{1}{P}\int h(x,y,u,v)(x-\bar{x})^k(y-\bar{y})^l(u-\bar{u})^m(v-\bar{v})^n dxdydudv, \tag{6.3}$$

where k, l, m and n are non-negative integers and the sum $k+l+m+n=2$. The third- and fourth-order moments are linked to the beam symmetry and sharpness of a laser beam [191, 197]. Here we focus on the second-order moments, which are also referred to as the generalized beam-propagation parameters [196]. All ten parameters constitute the beam matrix [172]:

$$\boldsymbol{P} = \begin{bmatrix} \boldsymbol{W} & \boldsymbol{M} \\ \boldsymbol{M^T} & \boldsymbol{U} \end{bmatrix} = \begin{bmatrix} W_{11} & W_{12} & M_{11} & M_{12} \\ W_{12} & W_{22} & M_{21} & M_{22} \\ M_{11} & M_{21} & U_{11} & U_{12} \\ M_{12} & M_{22} & U_{12} & U_{22} \end{bmatrix} = \begin{bmatrix} \overline{x^2} & \overline{xy} & \overline{xu} & \overline{xv} \\ \overline{xy} & \overline{y^2} & \overline{yu} & \overline{yv} \\ \overline{xu} & \overline{yu} & \overline{u^2} & \overline{uv} \\ \overline{xv} & \overline{yv} & \overline{uv} & \overline{v^2} \end{bmatrix}, \tag{6.4}$$

Generally, the spatial submatrix $\boldsymbol{W}$ and angular submatrix $\boldsymbol{U}$ are symmetric, and the mixed submatirx $\boldsymbol{M}$ is asymmetric. Depending on the number of independent second-order moments, three geometrical classifications of laser beams are defined: stigmatic (ST), simple astigmatic (SA) and general astigmatic (GA) [172, 198]. ST beams have maximum three independent second-order moments, and SA beams have maximum seven independent second-order moments:

$$\boldsymbol{P}_{ST} = \begin{bmatrix} W_{11} & 0 & M_{11} & 0 \\ 0 & W_{11} & 0 & M_{11} \\ M_{11} & 0 & U_{11} & 0 \\ 0 & M_{11} & 0 & U_{11} \end{bmatrix}, \ \boldsymbol{P}_{SA} = \begin{bmatrix} W_{11} & 0 & M_{11} & M_{12} \\ 0 & W_{22} & M_{12} & M_{22} \\ M_{11} & M_{12} & U_{11} & 0 \\ M_{12} & M_{22} & 0 & U_{22} \end{bmatrix}. \tag{6.5}$$

The GA beams have maximum 10 independent second-order moments. The propagation law for the beam matrix through first-order optical systems is

$$\boldsymbol{P_2} = \boldsymbol{S}\boldsymbol{P_1}\boldsymbol{S}^T, \tag{6.6}$$

where $\boldsymbol{S}$ is a 4×4 transformation matrix that describes a first-order optical system, often known as ABCD systems. For example, the free space propagation over a distance z can be describe by the matrix:

$$\boldsymbol{S}_f(z) = \begin{bmatrix} \boldsymbol{I} & z\boldsymbol{I} \\ 0 & \boldsymbol{I} \end{bmatrix}, \tag{6.7}$$

Thus, we can obtain the new beam matrix $\boldsymbol{P_2}$ after the propagation:

$$\boldsymbol{P_2} = \begin{bmatrix} \boldsymbol{W} + z\boldsymbol{M^T} + z\boldsymbol{M} + z^2\boldsymbol{U} & \boldsymbol{M} + z\boldsymbol{U} \\ \boldsymbol{M^T} + z\boldsymbol{U} & \boldsymbol{U} \end{bmatrix} \tag{6.8}$$

where the angular submatrix $\boldsymbol{U}$ remains the same during free-space propagation, while the other three submatrices are functions of propagation distance z. If we focus on the sub-matrix of the spatial moments $\boldsymbol{W}(z) = \boldsymbol{W} + z\boldsymbol{M^T} + z\boldsymbol{M} + z^2\boldsymbol{U}$, we have

$$\begin{aligned} W_{11}(z) &= \overline{x^2}(z) = \overline{x^2} + 2z\overline{xu} + z^2\overline{u^2} \\ W_{22}(z) &= \overline{y^2}(z) = \overline{y^2} + 2z\overline{yv} + z^2\overline{v^2} \\ W_{12}(z) &= \overline{xy}^{11}(z) = \overline{xy}^{11} + z(\overline{xv} + \overline{yu}) + z^2\overline{uv} \end{aligned} \tag{6.9}$$

From the new second-order spatial moments $W_{11}(z)$, $W_{22}(z)$ and $W_{12}(z)$, we can see that the free space second moment propagation is a parabolic function of the propagation distance z. Moreover, analytically the beam matrix can't be solely reconstructed by measuring intensity distributions through free space propagation, because the two terms $\overline{xv}$ and $\overline{yu}$ are coupled.

However, it is possible to recover a complete beam matrix through multiple intensity measurements. From a single intensity measurement, three spatial second-order moments out of ten can be directly calculated. By propagating the beam through known first-order optical systems, ten second-order moments are mixed in a deterministic way due to the propagation law (Eq. 6.6). Mathematically minimum four intensity measurements are needed to completely invert the beam matrix at the input plane (as shown in Eq. 6.10, $B_{in} = B_{out}A^{-1}$, 12 non-linear equations for 10 unknowns).

$$\underset{B_{out}}{\begin{bmatrix} (W_{11})_I \\ (W_{12})_I \\ (W_{22})_I \\ \vdots \\ (W_{11})_{IV} \\ (W_{12})_{IV} \\ (W_{22})_{IV} \end{bmatrix}} = \underset{A}{\begin{bmatrix} A_{1,1} & \dots & A_{1,10} \\ \vdots & \ddots & \vdots \\ A_{12,1} & \dots & A_{12,10} \end{bmatrix}} \underset{B_{in}}{\begin{bmatrix} W_{11} \\ W_{12} \\ W_{22} \\ M_{11} \\ M_{12} \\ M_{21} \\ M_{22} \\ U_{11} \\ U_{12} \\ U_{22} \end{bmatrix}} \tag{6.10}$$

Nemes and Siegman [172] proposed a method to calculate the beam matrix of GA beams based on intensity measurements by switching spherical and/or cylindrical lenses in the beam path. The combination of free-space propagation and a cylindrical lens has also been discussed [199]. These methods require lens switching and/or detector translation, which is practically inconvenient.

Ptychography offers a quantitative reconstruction of the complex beam profile. Knowing the complex beam profile theoretically allows to directly compute its Wigner distribution and its beam matrix. However, in practice this approach is challenging since the computational complexity of the Wigner distribution of a two-dimensional signal with N pixels per dimension is N^4. A computationally less demanding alternative is to implement a numerical equivalent of the approaches [172, 199, 200] by simulating beam propagation through ABCD optical systems. In this work, we obtain equivalent intensity information as in [200] by numerically propagating the measured complex field of the beam: three intensities are obtained through free-space propagation, while a fourth is obtained by simulating propagation through a cylindrical lens. This choice of output observations can be shown to be non-singular and thus invertible [172].

6.2.2 *Beam propagation ratio M^2*

The focusibility of a laser beam is quantified by a factor called M^2, also known as the beam propagation ratio[1]. It describes how tightly a laser beam can be focused compared to a diffraction-limited Gaussian beam (TEM_{00}) with the same wavelength, which has the smallest $M^2 = 1$ [170, 201]. In this section we show the definition and experimental determination of M^2.

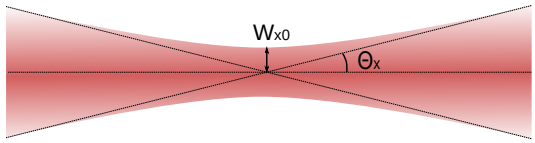

Figure 6.1

We have shown that in the previous section the second-order spatial moments in free-space propagation follows the parabolic relation. We rearrange the Eq. 6.9 into:

$$\begin{aligned}\overline{x^2}(z) &= \overline{u^2}(z + \frac{\overline{xu}}{\overline{u^2}})^2 + \overline{x^2} - \frac{\overline{xu}^2}{\overline{u^2}} \\ &= \overline{u^2}(z - z_{x0})^2 + \overline{x^2}_0 \end{aligned} \tag{6.11}$$

where z_{x0} is the the position where we obtain the minimum $\overline{x^2}_0$. The same can be done for $\overline{y^2}(z)$ in the y-direction. We adopt the variance definition ($D4\sigma$ definition) for the beam radius:

$$W_x(z) \equiv 2\sigma_x = 2\sqrt{\overline{x^2}(z)}, \tag{6.12}$$

1 The two terms M^2 and beam propagation ratio (BPR) are the same and are inter-changeable

Then by substituting variables in Eq. 6.11, we obtain the mathematical expression of how the beam radius of a laser beam (of arbitrary spatial modes) propagates in free space under paraxial approximation [170, 171, 201]:

$$W_x{}^2(z) = W_{x0}{}^2 + M_x{}^4(\frac{\lambda}{\pi W_{x0}})^2(z - z_{x0})^2. \tag{6.13}$$

where W_{x0} is the beam waist, and $M_x{}^2$ is called the beam propagation ratio (BPR) which is defined as the product of two standard deviations in the real and Fourier space at the focal plane of the beam:

$$M_x{}^2 = 4\pi\sqrt{\overline{x^2}_0}\frac{\sqrt{\overline{u^2}}}{\lambda} = 4\pi\sigma_{x0}\sigma_{s_x}. \tag{6.14}$$

The normalized angular coordinates $s_x = u/\lambda$ and $s_y = v/\lambda$ are known as the spatial frequency coordinates. Since σ_{x0} and σ_{s_x} are Fourier pairs, they satisfy the condition $\sigma_x\sigma_{s_x} \geq 1/4\pi$, which gives

$$M_x{}^2 \geq 1, \tag{6.15}$$

where the equality holds for a diffraction-limited Gaussian beam. Another way to interpret the definition of the beam propagation ratio is

$$M_x{}^2 = \frac{W_{x0}\Theta_x}{\lambda/\pi} = \frac{BPP}{BPP_G}, \tag{6.16}$$

where $\Theta_x = 2\sqrt{\overline{u^2}}$ is the half-angle beam divergence (see in Fig. 6.1). The product of the two is also called Beam Parameter Product (BPP), and the smallest BPP is from a diffracted limited Gaussian beam, which has a value of λ/π. Thus the beam propagation ratio M^2 can be defined as the ratio between the BPP of the beam and the BPP of a diffraction-limited Gaussian beam at the same wavelength. Both BPP and M^2 are free-space propagation invariant. M^2 of a laser beam can be determined experimentally through caustic measurements: measuring the bean radius as a function of propagation distance, then fit the data into Eq. 6.13, where M_x^2 and M_y^2 can be extracted. Commercial M^2-measurement devices obtain the caustic measurement by scanning a lens. However, only for ST and aligned SA beams, M_x^2 and M_y^2 stay invariant while propagating through aberration-free first-order optical systems[2]. For misaligned SA, and GA beams, this way of determining M^2 is not accurate. A prior knowledge about the geometrical type of the beam becomes necessary before performing the traditional M^2 measurement, which limits it's applications. A more general way to determining M^2 is explained in the next section.

6.2.3 *General calculation for BPR and IAF*

A more general characterization of an arbitrary laser beam is to reconstruct the full beam matrix, from which the geometric type of the beam can be classified.

2 Free-space propagation is a special case of first-order optical systems, where M_x^2 and M_y^2 are invariant through propagation. However, commercial M^2-measurement devices often uses a lens, and M_x^2 and M_y^2 become variant after lens transformation.

Nemes [172] has shown that for a laser beam of any geometrical kind, two invariants exist when the beam propagates through first-order optical systems, which define the intrinsic classification of a laser beam. The correlation between the geometrical and intrinsic classifications of a laser beam has been studied [198, 202]. One invariant is the effective BPR M^2_{eff}:

$$M^2_{\text{eff}} = \frac{4\pi}{\lambda}[det(\boldsymbol{P})^{\frac{1}{4}}] \geq 1. \tag{6.17}$$

For SA beams, the BPR can be calculated along two principle axes as [172]:

$$\begin{aligned} M^2_x &= \frac{4\pi}{\lambda}\sqrt{W_{11}U_{11} - M^2_{11}} \geq 1, \\ M^2_y &= \frac{4\pi}{\lambda}\sqrt{W_{22}U_{22} - M^2_{22}} \geq 1, \end{aligned} \tag{6.18}$$

where $M^2_{\text{eff}} = \sqrt{M^2_x M^2_y}$ holds for SA beams measured along the principle axes. For ST beams, a single factor $M^2 = M^2_x = M^2_y = M^2_{\text{eff}} \geq 1$ is used to describe its focusability property. $M^2 = 1$ holds for a stigmatic Gaussian TEM_{00} beam, which indicates ideal collimation and focusing properties.

The other invariant is the intrinsic astigmatism factor (IAF) a [172]:

$$\begin{aligned} a = \frac{8\pi^2}{\lambda^2}[&(W_{11}U_{11} - M^2_{11}) + (W_{22}U_{22} - M^2_{22}) \\ &+ 2(W_{12}U_{12} - M_{12}M_{21})] - M^4_{\text{eff}} \geq 0. \end{aligned} \tag{6.19}$$

The IAF is zero for ST beams, as well as for SA and GA beams that can be transformed into ST beams through symplectic optical systems. Note that it is different from Zernike-based astigmatic aberration, where the beam exhibits different focii in different planes along propagation. According to ISO 11146 [196], a beam is classified as intrinsically stigmatic if the normalized IAF

$$\frac{a}{M^4_{\text{eff}}} < 0.039. \tag{6.20}$$

Thus, once the beam matrix is known, the geometrical type of beam can be classified, and the corresponding BPR and IAF can be extracted. In section 6.2.1, we have explained that a complete beam matrix of a laser beam can be calculated by numerically propagating the complex-valued beam through ABCD optical systems. One advantage is that the choice of the propagation distances and focal strengths of lenses in the simulation is flexible. So we choose observation planes in which the four transformed beam profiles have beam widths greater than 10% of the numerical array size. This approach avoids inaccurate second-order moment determination due to noise, which can be major source of error in propagation-based M^2-measurement devices that require careful background subtraction methods in particular around the focal plane of a laser beam [194–196].

6.2.4 *Zernike decomposition of aberrated wavefronts and transmission functions*

Zernike polynomials are a complete set of orthogonal polynomials, widely used in optical wavefront analysis and aberration characterization of optical components and systems. It is defined on a unit circle, usually in polar coordinate (ρ, θ), where the radial component ρ is in the range of 0 to 1, and the azimuthal component ranges from 0 to 2π. Each Zernike polynomial is expressed as a product of three terms (in double-index convention):

$$Z_n^m(\rho,\theta) = N_n^m R_n^m(\rho)\Theta(\theta), \tag{6.21}$$

where N_n^m is a normalization factor:

$$N_n^m = \sqrt{\frac{2(n+1)}{1+\delta_{m0}}}, \tag{6.22}$$

$R_n^m(\rho)$ is a radial dependent term:

$$R_n^m(\rho) = \sum_{k=0}^{\frac{n-|m|}{2}} \frac{(-1)^k (n-k)!}{k![\frac{n+|m|}{2}-k]![\frac{n-|m|}{2}-k]!}\rho^{n-2k}, \tag{6.23}$$

and $\Theta(\theta)$ is a azimuthal dependent term:

$$\Theta(\theta) = \begin{cases} \cos(m\theta); & \text{for } m \geq 0 \\ \sin(-m\theta); & \text{for } m < 0 \end{cases}. \tag{6.24}$$

The index n is a nonnegative integer, describing the highest order of the radial polynomial. The index m ($|m| \leq n$) is the azimuthal frequency. For a given n, the azimuthal frequency m can only be $-n, -n+2, -n+4, ..., n$. For convenience, we use Noll's convention for the Zernike polynomials [203]. Figure 6.2 shows the first 28 Zernike polynomials.

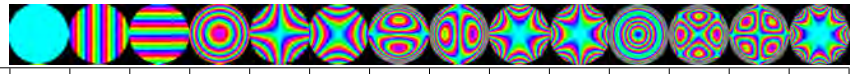

Z_j	Z_1	Z_2	Z_3	Z_4	Z_5	Z_6	Z_7	Z_8	Z_9	Z_{10}	Z_{11}	Z_{12}	Z_{13}	Z_{14}
Z_n^m	Z_0^0	Z_1^1	Z_1^{-1}	Z_2^0	Z_2^{-2}	Z_2^2	Z_3^{-1}	Z_3^1	Z_3^{-3}	Z_3^3	Z_4^0	Z_4^2	Z_4^{-2}	Z_4^4

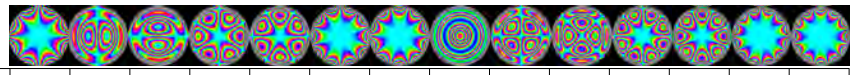

Z_j	Z_{15}	Z_{16}	Z_{17}	Z_{18}	Z_{19}	Z_{20}	Z_{21}	Z_{22}	Z_{23}	Z_{24}	Z_{25}	Z_{26}	Z_{27}	Z_{28}
Z_n^m	Z_4^{-4}	Z_5^1	Z_5^{-1}	Z_5^3	Z_5^{-3}	Z_5^5	Z_5^{-5}	Z_6^0	Z_6^{-2}	Z_6^2	Z_6^{-4}	Z_6^4	Z_6^{-6}	Z_6^6

Figure 6.2: The first 28 Zernike polynomials in both double-index convention (Z_n^m) and Noll's convention (Z_j).

Assuming that the phase of the illumination $P(\boldsymbol{r}) = |P(\boldsymbol{r})| \exp[i\alpha(\boldsymbol{r})]$ and object transmission function $O(\boldsymbol{r}) = |O(\boldsymbol{r})| \exp[i\beta(\boldsymbol{r})]$ recovered in ptychography

can be unwrapped into smooth functions $\alpha(\boldsymbol{r})$ and $\beta(\boldsymbol{r})$, we can expand these into Zernike polynomials Z_j, i.e.

$$\alpha(\boldsymbol{r}) = \sum_j a_j Z_j(r, \vartheta), \tag{6.25}$$

and

$$\beta(\boldsymbol{r}) = \sum_j b_j Z_j(r, \vartheta), \tag{6.26}$$

where $r = \sqrt{x^2 + y^2}$ and $\vartheta = \arctan(y/x)$ are polar coordinates. It is noted that the assumption of smoothness does not hold for singular beams and optical elements such as phase plates. While ptychography still functions properly under these circumstances, an aberration analysis in terms of Zernike polynonmials is then not suitable and other choices of basis functions such as Laguerre-Gaussian modes are more appropriate.

6.2.5 *Experimental setup*

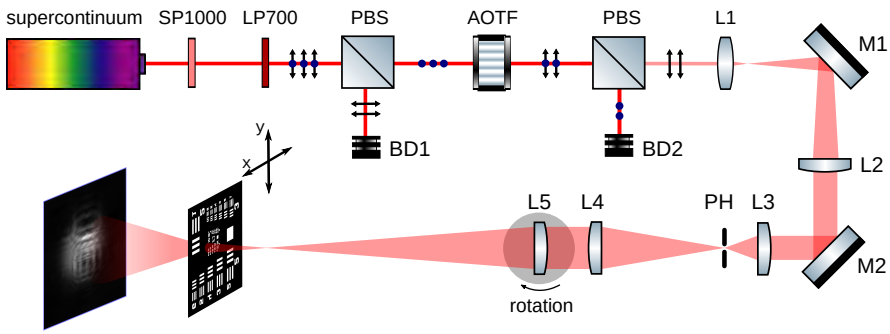

Figure 6.3: Experimental setup. A supercontinuum source is spectrally limited via short pass (SP1000) and long pass (LP700) filters to the range 700 nm to 1000 nm. A linearly polarized, quasi-monochromatic beam is produced using a combination of polarizing beam splitters (PBS) and an acousto-optic tunable filter (AOTF). The beam is expanded through lenses L1 ($f_1 = 25$ mm) and L2 ($f_2 = 300$ mm), and spatially filtered through elements L3 ($f_3 = 50$ mm), PH (20 µm pinhole), and L4 ($f_4 = 200$ mm). Finally the beam is focused by L5 ($f_5 = 500$ mm) onto a sample. Translating the specimen transversely and recording the resulting diffraction intensities give the input data for the ptychographic analysis.

The experimental setup we used for ptychography is depicted in Fig. 6.3. A supercontinuum source (NKT Photonics whiteLase Micro, 400 nm to 2000 nm, output power 200 mW) is spectrally limited by the use of two successive edgepass filters (Thorlabs LP700 and SP1000) to the range of 700 nm to 1000 nm. An acousto-optic tunable filter (AOTF, Gooch & Housego, TF950-500-1-2-GH96, 700 nm to

1200 nm) selects a narrow spectral bandwidth (bandwidth 0.6 nm, $\lambda/\Delta\lambda > 1000$). Polarizing beam splitters (PBS) are used to feed a linearly polarized beam into the AOTF and to select the first diffraction order downstream the AOTF. After a relay unit consisting of lenses (L1, L2) and mirrors (M1, M2), the beam is spatially filtered (pinhole PH, 20 µm) and collimated. A lens (L5) focuses the beam onto a specimen mounted on an encoded xy-translation stage (2x Smaract SLC-1770-D-S, 46 mm travel range, 70 nm repeatability). The resulting diffraction intensities downstream the sample are recorded on a CCD camera (AVT prosilica GX1920, 14 bit, pixel size 4.54 µm). In part of the experiment (discussed in section 6.3.2), the lens L5 is rotated to generate astigmatic beams for astigmatic wavefront analysis.

6.3 RESULTS

6.3.1 *Spectrally-resolved beam parameters (BPR and IAF)*

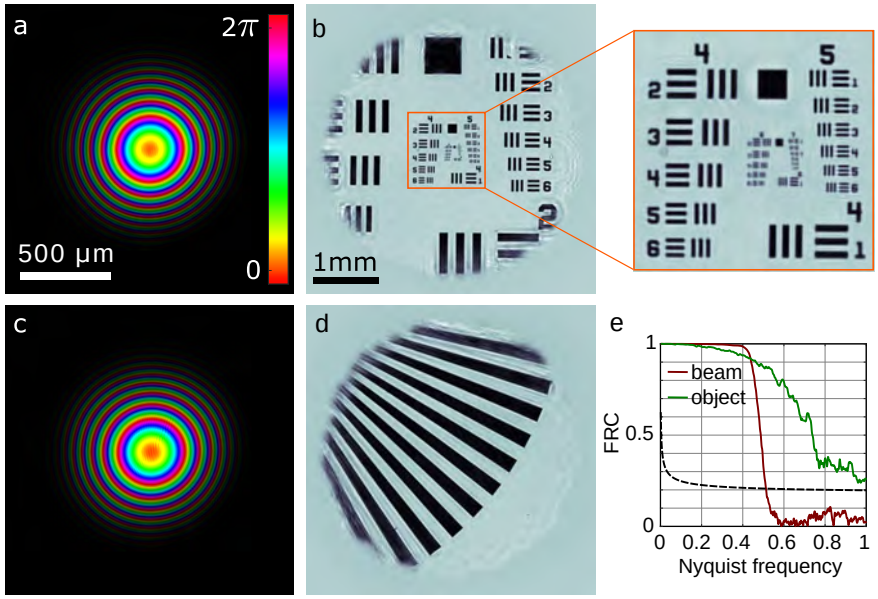

Figure 6.4: (a,b) Reconstructed probe and object for the USAF target at the central wavelength $\lambda = 784$ nm. (c,d) Reconstructed probe and object for Siemens star at $\lambda = 784$ nm. Panel (a) and (c) share the same scale bar and color bar. Panel (b) and (d) share the same scale bar. (e) Fourier ring correlation (FRC) of two independent data sets measured with the Siemens star at the central wavelength $\lambda = 784$ nm. The dashed line is the 1/2-bit resolution threshold.

To test the extraction of the BPR and IAF from the reconstructed beams by means of ptychography, we collected 15 ptychographic data sets in the spectral range from 709 nm to 842 nm for both USAF (Thorlabs R3L1S4P) and Siemens star (Thorlabs R1L1S3P) resolution test targets. The distance between the sample and

the camera is 42.8 mm. Each data set consists of 200 diffraction patterns recorded in a Fermat's spiral scanning pattern [147], with an average overlap of 70%. This relatively high overlap parameter is chosen in order to guarantee a high-quality reconstruction of the beam. Reconstructions were carried out using an NVIDIA Tesla K40 GPU.

The reconstructed probe and object for the ptychography scan of the USAF target at the central wavelength of 784 nm are shown in Fig. 6.4(a) and (b), respectively. Likewise, the reconstructed probe and object for the Siemens star at 784 nm are shown in Fig. 6.4(c) and (d), respectively. In the probe plots (Fig. 6.4(a, c)), hue depicts phase modulo 2π and brightness depicts the square root of the intensity of the illuminating beam. In the object plots (Fig. 6.4(b, d)), only the modulus of the object transmissivity is shown since the reconstructed phase is flat. The reconstruction pixel size for both the probe and the object is 5.5 µm. The half period spatial resolution of the USAF reconstruction at 784 nm is 7.8 µm (Element 1 in group 6 on the USAF target). In order to assess the reproducibility of both the probe and object estimates, we reconstructed two independent data sets measured with the Siemens star at 784 nm and calculated the Fourier ring correlation (FRC) [154]. This is shown in Fig. 6.4(e). The dashed line is the 1/2-bit resolution threshold. The intersection of the object and probe FRC curves and the threshold indicates the reconstruction resolution. It is seen that the two independent object reconstructions are consistent up to the Nyquist frequency, which in our experiment is limited by the detector numerical aperture. For the probe beam, the two reconstructions are consistent up to half of the Nyquist frequency. This is due to the fact that the beam does not contain higher spatial frequencies.

From each complex-valued probe reconstruction, we calculate the beam matrix at each wavelength, and the results show that all beams are SA beams. Following Eq. 6.17-6.19, we computed the M_x^2, M_y^2, M_{eff}^2 and IAF values for each beam, which are shown in Fig. 6.5(a-d), respectively. Across the full wavelength range, the average difference of the extracted M_x^2, M_y^2 and M_{eff}^2 measured between two different samples is 4%, 3% and 4% respectively, which confirms that the complex-valued beam reconstruction is sample-independent. The normalized IAF (a/M_{eff}^4) in Fig. 6.5(d) is below 0.039 as marked by the dashed line, which classifies the beams at all wavelengths as intrinsically stigmatic. In Fig. 6.5(c,d), at 709 nm and 784 nm, both M_{eff}^2 and a/M_{eff}^4 values calculated from five independent measurements on the Siemens star are shown as black dots.

6.3.2 *Characterization of aberrated wavefronts*

In addition to characterizing beam profiles and wavefronts, the ptychographic reconstruction approach is equally suitable for analyzing the quality of optical components. We introduced astigmatism to the probe beam at 784 nm by manually rotating lens L5 in Fig. 6.3. Three ptychographic measurements were performed under the same experimental conditions as mentioned in section 6.3.1 with a USAF resolution target at three different lens angles ($\theta = 0°, 15°, 30°$). The reconstructed complex beams at the object plane are depicted in Fig. 6.6(a-c). Here Fig. 6.6(a) shows the reconstructed beam in the default alignment ($\theta = 0°$) before rotating the lens. Figure 6.6(b) and (c) show the reconstructed beam with increased lens

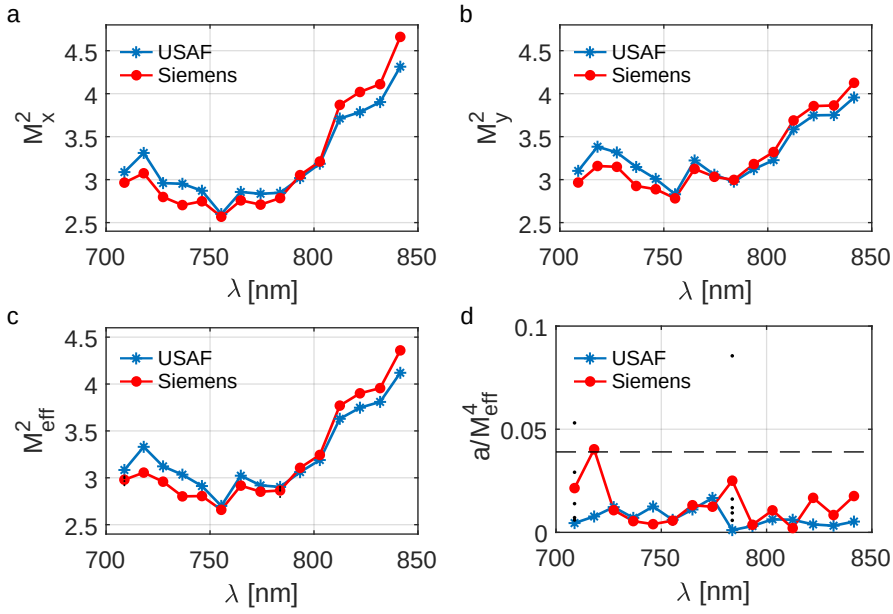

Figure 6.5: (a) M_x^2, (b) M_y^2, (c) M_{eff}^2 and (d) normalised IAF as a function of wavelength for USAF (blue, asterisk) and Siemens star (red, dot) resolution test targets. At 709 nm and 784 nm, five independent measurements are carried out with the Siemens star. The corresponding M_{eff}^2 and a/M_{eff}^4 values are shown as black dots in (c) and (d) respectively.

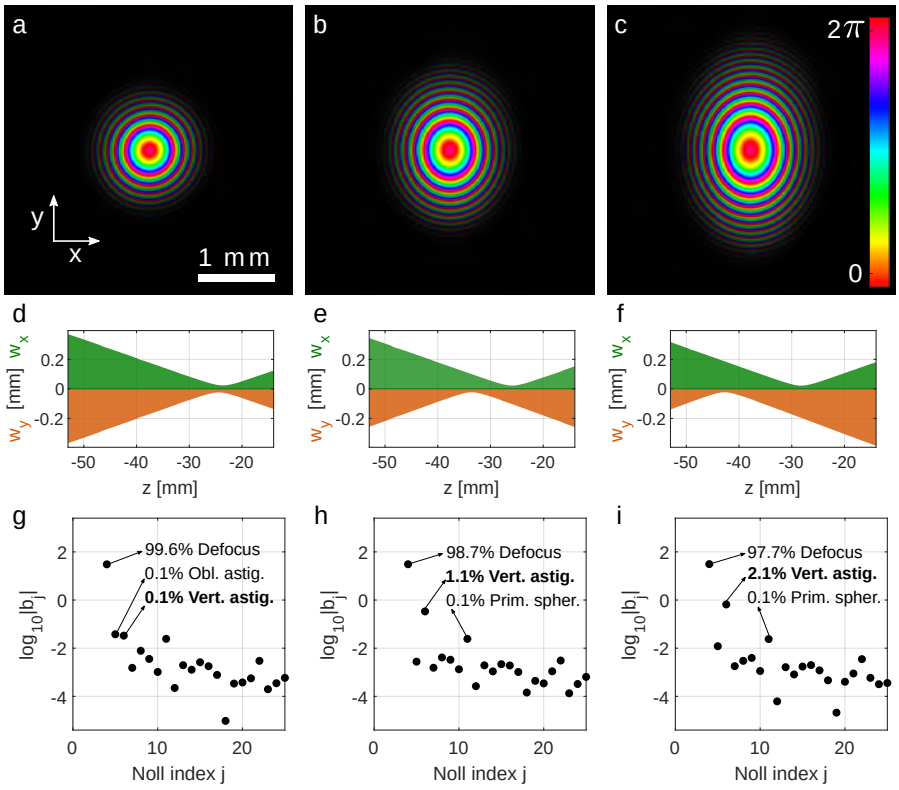

Figure 6.6: (a-c) Reconstructed probe beams at 784 nm produced at three different angles of the lens L5 (compare Fig. 6.3). The scale and color bar are shared among a-c. (d-f) Beam radii in x- (upper green) and y-direction (lower orange) as a function of propagation distance z for three different probe beams (the object plane is defined at $z = 0$). (g-i) Zernike expansion coefficients. Top three contributions (excluding piston and tilts) are listed in each case.

rotation around the y-axis ($\theta = 15°, 30°$). The calculated beam radii ($w = 2\sigma$) in x- and y-direction as a function of propagation distance z upstream the object (the object is at z = 0 mm) are plotted in Fig. 6.6(d-f). Increased lens rotation introduces astigmatism, which results in different focal lengths in x- and y-direction. We numerically propagated the three beams back to the lens plane (-52 cm) and calculated the first 25 Zernike coefficients (b_j in Noll's convention) for each. The results are shown in Fig. 6.6(g-i). The first three Zernike coefficients (piston and tilts) are excluded since they are non-unique in ptychographic reconstructions. Figure 6.6(g) shows that the default wavefront ($\theta = 0°$) is dominated by defocus, plus small contributions of oblique and vertical astigmatism. At a lens orientation of $\theta = 15°$, the vertical astigmatism contribution increases to 1.1%. At a lens rotation of $\theta = 30°$, the contribution of vertical astigmatism increases further to 2.1%.

6.3.3 *Aberration characterization of a microlens array*

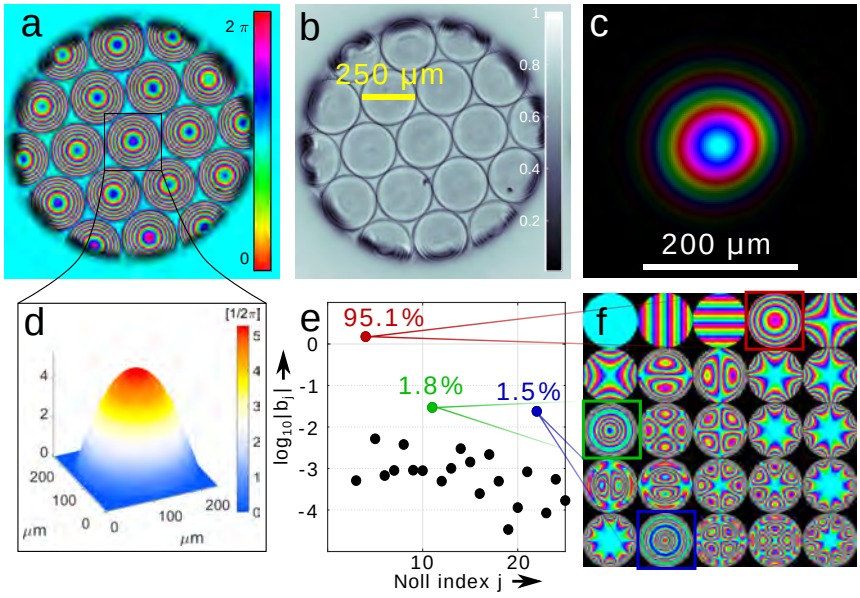

Figure 6.7: (a) Reconstructed complex transmissivity of a microlens array. Hue and brightness represent phase modulo 2π and transmissivity. (b) Modulus of (a). (c) Reconstructed probe beam. (d) Extracted transmission function of central microlens in (a). (e) Zernike expansion coefficients. The relative contributions in percent for defocus (red), primary spherical (green), and secondary spherical (blue) aberrations are highlighted. (f) The first 25 low-order Zernike polynomials in Noll's convention. Panels (a), (c), and (f) share the same colormap.

To illustrate the high spatial resolution that can be achieved, we describe the experimental characterization of a microlens array by means of ptychography.

A microlens array (Suss MicroOptics, MLA no. 18-00082) was mounted on the scanning stage in the experimental setup in Fig. 6.3. A wavelength of 784 nm was selected by the AOTF. The distance from the lens L5 to the object was adjusted to produce a beam with an approximate full width at half maximum of 200 µm. A total of 1500 diffraction patterns were recorded in a Fermat's spiral scanning pattern, with an average overlap of 80%. The distance between the microlens array and the detector was 41.5 mm.

The reconstruction result of the microlens array is shown in Fig. 6.7. Figure 6.7(a) shows the complex transmission function of the object. The colormap in Figure 6.7(b) shows the transmissivity, as would be observed under a bright field transmission microscope. Figure 6.7(c) depicts the reconstructed probe. A central microlens (black square in Fig. 6.7(a) was selected and phase unwrapped as shown in Fig. 6.7(d). The unwrapped wavefront was decomposed into Zernike polynomials. Figure 6.7(e) depicts the expansion coefficiencts b_j (see Eq. 6.26) in the Zernike decomposition on a semi-log-scale. We highlighted the relative magnitude of the three dominant contributions, namely the Zernike coefficients for defocus (red, 95.1%), primary spherical (green, 1.8%), and secondary spherical (blue, 1.5%) aberrations. As in the previous section, piston and tilt were excluded due to their non-uniqueness.

6.4 DISCUSSION

We have shown that quantitative laser beam quality characterization can be readily performed via ptychography. Using ptychography for quantitative wavefront reconstructions raises the question which objects are suitable for wavefront analysis, and whether or not this analysis is reproducible across objects. While we have not answered this question in general or from a theoretical standpoint, we used simple binary objects with distinct spatial features to show that in practice the beam reconstruction is reproducible and largely independent of the selected object. In the beam characterization experiments, 200 scanning positions were used to cover an object field of view (FoV) of 4 mm in diameter (see Fig. 6.4(b,d)). In principle, less scanning positions can be chosen to speed up both the data acquisition and process time at the expense of object FoV.

Nonetheless, an important requirement in Fresnel and far-field ptychography is that the probe has a finite extent in the object plane in order to prevent undersampling in the detection plane. The upper limit of the beam diameter D is given by $D \leqslant \lambda z / x_p$, where λ, z, and x_p are the wavelength, object-detector distance, and detector pixel size, respectively. Variations of ptychography have been reported that allow to relax this restriction [204, 205].

One of the difficulties we encountered in the beam characterization is that the second-order moment calculation is sensitive to noise as it depends quadratically on the probe coordinates. Thus in particular for small beams, residual noise contributions at edges of the numerical array can significantly affect the second-order moment estimation. This noise issue also affects traditional focus-scanning-based M^2 measurements, where an accurate determination of the second-order moments near the focus is critically dependent on the choice of noise corrections. ISO 11164 [196] provides suggestions on background and offset corrections in

order to select out the illuminated pixels from direct intensity measurements, where it is assumed that the detected intensities are subject to Gaussian noise. However, a subtlety in our experiments is that the reconstruction plane is not equal to the detection plane, leading to a transformation of the underlying noise distribution. In particular, the noise in our beam reconstructions consists of complex-valued random phasor sums, leading to an intensity distribution often modelled by a Rician distribution [206]. Using our numerical approach we could bypass these subtleties by using symplectic beam matrix transformations that lead to expanded beams, where the second moment is much less sensitive to the underlying noise at large coordinates. We observed stable M^2 values when the beam width was at least 10% of the total array dimension. No masking or thresholding was applied to avoid underestimation of the beam width by cutting the tails of the beam. These features make ptychography into a robust approach for beam matrix determination and M^2 characterization, with clear advantages over conventional methods in terms of noise sensitivity. Further studies on noise propagation in ptychography have to be carried out to improve the accuracy of the second-order moment calculation and allow for automated M^2 and IAF extraction.

Zernike decomposition was used in the analysis of aberrated wavefronts induced by lens rotation. All beams were propagated back to the focusing lens plane where the Zernike decomposition takes place. Although Zernike polynomials have been widely applied in aberration analysis for various optical systems, one limitation is that they are not free space propagation invariant. An alternative propagation invariant, orthogonal modal expansion has been proposed and could be used to avoid the back-propagation step (compare section 6.3.2) into the lens plane plane [207].

We have shown an optical shop testing application, where a microlens array was reconstructed and decomposed into Zernike polynomials. We observed that using a beam size smaller than the spatial periodicity of the microlens array (250 µm) helps the algorithm converge to the solutions much faster than when using a larger beam. For larger beams, the periodicity of the microlens array results in diffraction patterns with increasingly pronounced Bragg peaks. Translating the object through a large beam only leads to a small variation in the signal between the Bragg peaks, which may cause the algorithm to struggle for convergence. To mitigate issue due to sample periodicity, a technique referred to as modulus enforced probe (MEP) may be used, which additionally constrains the detector wave in the absence of the sample [85]. Recent work by other researchers used a structured probe to analyse a microlens array, suggesting that the information content in the diffraction data can be increased by breaking the spatial periodicity of the sample by use of a non-smooth probe profile [37]. This allows the use of larger beams, which are preferred to reduce the total number of measurements to cover a large object field of view.

6.5 CONCLUSION

Ptychography allows to reconstruct both the intensity profile and wavefront of linearly polarized laser beams, which enables various ways of quantitative

characterization of interest. We have shown that one ptychography setup can replace both an M^2-measurement device and a wavefront sensor at the same time, while outperforming both in terms of spatial resolution and versatility of the experimental setup. For laser beam quality characterization, commercial M^2-measurement devices based on axial detector translation are only suitable for stigmatic and simple astigmatic beams. We demonstrated that ptychography enables complex beam recovery from which the complete beam matrix and derived quantities such as M_x^2, M_y^2, M_{eff}^2 and IAF can be computed. By decomposing the recovered beam and object into Zernike polynomials, ptychography can be used for quantitative characterization of beam misalignment and optical shop testing. We therefore believe that wavefront sensing via ptychography is superior to holography, Hartmann-Shack sensors, and propagation-based phase retrieval in applications where speed is not critical.

7

CHARACTERIZATION OF ROUGH SURFACES

ABSTRACT

We apply computational imaging methods for surface roughness characterization. Steel surfaces with a roughness value similar to or larger than the optical wavelength are investigated. We show rough surface reconstructions using both Ptychography and computational OCT, between which challenges and differences are discussed. Height map reconstructions from computational OCT show good agreement with results obtained from commercial confocal instruments. Besides direct imaging of rough surfaces, we also present an approach to extract surface roughness parameters from indirect scattering speckle measurements. We explore the relation between polychromatic speckle contrast and surface roughness, where a generalized model is presented and discussed.

7.1 INTRODUCTION

2D Surface topography plays an important role in determining surface properties, e.g. friction, thermal conductance, adhesion, and optical scattering properties [208]. In the steel industry, surface roughness is measured in manufacturing for production monitoring and product control purposes. Accurate off-line measurement techniques are available [209], which, however, are time consuming, therefore resulting in long feedback cycles. Fast and accurate on-line metrology tools for surface topography measurements are highly desired.

Stylus profilometry is a traditional profiling technique that uses a micron-scale probe to physically contact and scan a surface. The height profile of the surface is recorded from the mechanical feedback of the instruments. Stylus profilometers provide accurate and robust height profile measurements with a high resolution down to sub-nanometers and a large height measurement range from tens of nanometers up to a few millimeters [209]. However, it can cause damage to the surface and the scanning process is time-consuming. The transverse resolution, which is limited by the tip size, often ends up in the range of a few micrometers. A high precision scanning probe microscopy technique [210], i.e. atomic force microscopy (AFM) is also used for measuring rough surfaces. It offers sub-nanometer height and lateral resolution. The disadvantages are low measurement speed and small field of view. Both scanning techniques require a relatively clean and stable working environment, which make them only suitable for off-line metrology.

Compared to mechanical-scanning contact type of techniques, optical methods allow direct two dimensional probing with a longer working distance. Therefore optical methods have great potentials for wide-field, contactless, non-destructive, high-speed, and on-line surface metrology applications. There are generally two types of optical approaches for rough surface characterization. One is to optically map out the surface topography using imaging techniques such as white light interferometry, phase shifting interferometry, as well as scanning confocal microscopy [211–214]. The other is the so called parametric approach, which measures scattering speckles of rough surfaces to estimate statistical characterizations of the surface without resolving the surface topography [211, 215]. The optical imaging approach offers a high resolution in height measurement down to sub-nanometers, and a good transverse resolution ranging from a few tens of micrometers down to sub-micrometer. However, although imaging techniques are non-contact, the required working distance decreases with the increase of imaging resolution. They also require stationary samples which makes them less suitable for on-line measurements where sample vibrations and movements are unavoidable. The optical scattering-based techniques in principle are best suited for performing fast measurements in a manufacturing environment. Rough surface scattering phenomena have been investigated since the 1960s when coherent laser light became available. Analytical models have been developed to predict how light scatters from rough surfaces, from which statistical properties of the surfaces can be obtained. However, due to the complexity of the scattering problem, many assumptions of statistical properties of rough surfaces often have to be made to simplify the problem, which makes it challenging to account for general

rough surfaces. In particular, the extremes of very rough and very flat surfaces are analytically tractable, while wavelength-scale surface roughness measurements have remained challenging. It is the latter regime that the experiments below are focused on.

In this chapter, we explore the capability and limitation of two computational imaging techniques, ptychography and computational OCT, for rough surface characterization. Also, a model-based method for extracting surface roughness values from speckle contrast measurements is shown and discussed.

7.2 SURFACE ROUGHNESS PARAMETERS

We first introduce two parameters used to describe vertical variations of a rough surface[1]. We use $Z(x,y)$ to represent a 2D surface height distribution with a zero mean. Following the ISO definition [216], S_a is called the arithmetical mean of the height distribution over a defined surface area A:

$$S_a = \frac{1}{A}\iint_A |Z(x,y)|dxdy. \tag{7.1}$$

S_q is the root mean square (rms) roughness parameter over a defined surface area A:

$$S_q = \sqrt{\frac{1}{A}\iint_A Z^2(x,y)dxdy}, \tag{7.2}$$

where $S_q \geq S_a$. In particular, for surfaces whose height distribution follows Gaussian statistics, the relation holds [211]: $S_q = \sqrt{\frac{\pi}{2}}S_a$

7.3 ROUGH SURFACE CHARACTERIZATION USING COMPUTATIONAL IMAGING TECHNIQUES

When laser light reflects from a single smooth surface, where the scale of the micro-structures is much smaller than the wavelength of the light, single scattering events dominate. Assuming plane wave illumination, the phase of the exit surface wave directly represents the height variation of the surface, which makes it straightforward to retrieve the surface topography using optical imaging methods. However, when light reflects off a rough surface, where phase wrapping problems rise, also multiple scattering events possibly can not be ignored anymore, the exit surface wave thus no longer directly represents the surface topography. Yet, it has been shown that the interaction between laser light and rough surfaces is deterministic, which leads to a deterministic speckle pattern [217]. Thus it should be possible to obtain some information about the micro-structures on the surface. In this section, using computational imaging methods we try to reconstruct surface topographies of rough steel samples with an S_a value at the scale or larger than the optical wavelength. Results from ptychography and computational OCT are presented and discussed.

1 A correlation length is typically used to describe the transverse scale of a rough surface, which is not discussed in this thesis.

7.3.1 *Rough surface imaging using ptychography*

Ptychography offers a quantitative reconstruction of an object, which is separated from the illumination. Reflection ptychography has been used to obtain surface height maps from quantitative phase reconstructions [84] as:

$$Z(x,y) = \frac{\Delta\phi(x,y)}{4\pi}\lambda. \tag{7.3}$$

The phase shift $\Delta\phi(x,y)$ has two contributions: one is the material dependent phase shift upon reflection, the other is from the optical path delays determined by the geometric height differences of the surface. In the case of a single material surface, the geometric phase shift dominates [84]. Thus the height map $Z(x,y)$ can be directly calculated from the phase shift term $\phi(x,y)$ obtained from ptychography using Eq. 7.3 for height variations smaller than half of the wavelength. Otherwise phase wraps lead to ambiguities. In Ref. [84], the authors show that the height range can be extended by using dual wavelengths, where a so called synthetic wavelength $\lambda_{syn} = \frac{\lambda_1\lambda_2}{|\lambda_1-\lambda_2|}$ determines the measurement range, which can be much longer than either of the two wavelengths.

The reconstructed surface reported in [84] has micrometer-scale height variations with fairly smooth surfaces (nanometer-scale roughness). Here, we apply ptychography on surfaces with a roughness S_q comparable or even larger than the illumination wavelength. We use the same experimental settings as shown in Fig. 4.2, where a pinhole is imaged onto the surface to provide a localized probe. A pre-calibrated probe function from ptychography measured with a USAF sample is used as the initial guess, which speeds up the convergence significantly. Figure 7.1(a) shows a complex plot of the reconstructed steel surface with a nominal S_a value[2] of 0.7 µm, which is comparable to the wavelength $\lambda = 708\,\text{nm}$. Figure 7.1(b) shows a complex plot of the reconstructed probe. The amplitude of a zoomed-in region of the steel surface is plotted in Fig. 7.1(c), where the similar features can be recognized comparing to the photo reconstruction in Fig. 7.1(d) from confocal measurements provided by Tata Steel, although different areas are measured.

In fact, attempts of reconstructing steel surfaces with higher roughness values all failed. For this surface with an S_a value of 0.7 µm, although the algorithm converges, we can see that the reconstruction quality of the steel surface is not ideal. In Fig. 7.1(a), the surrounding area outside the scan region is filled with noise, which does not comply with the fact that a localized beam with hard edges is used. This is an indication that the forward model (2.38) used in ptychography does not correctly describe the diffraction data. There are two possible explanations for the problems: one is that random structures on the steel surface exhibit large-angle scattering beyond the detection NA, where a fair fraction of the beam energy is not accounted for in the reconstruction. One observation supporting this argument is that the scattered light indeed spreads to the edges of diffraction patterns on the camera. This also induces numerical errors due to the periodic convolution nature of discrete Fourier transforms. The other possible cause is multiple scattering.

2 The reference value is provided by Tata Steel using confocal microscopy

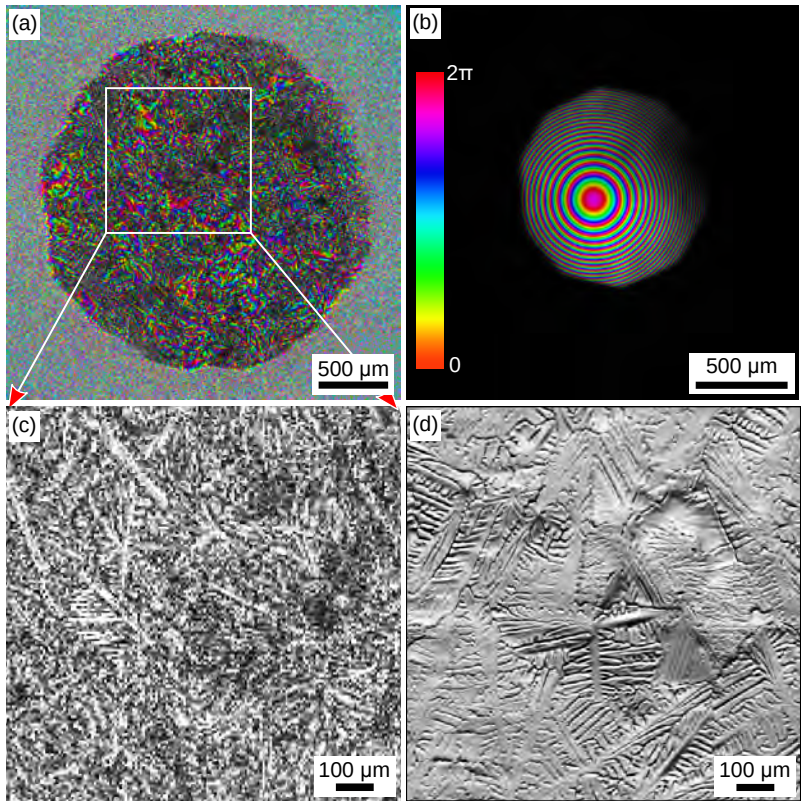

Figure 7.1: (a) and (b) Ptychographic reconstruction of a steel surface and the corresponding probe beam, respectively. In the complex plot, the brightness represents the amplitude and the hue represents the phase. The color bar is shared between (a) and (b). (c) Amplitude plot of the zoom-in region of the reconstructed steel surface in (a). (d) A photo reconstruction of the steel surface in false color by Tata Steel.

Intuitively, due to multiple scattering, the probe 'sees' a different object after each translation where the forward model breaks down. Future work needs to be carried out to verify the main cause of the reconstruction artefacts. For the high-NA scattering argument, a larger detector can be used to avoid the missing data problem. Alternatively, a super-resolution ptychography method [218] has been reported to extrapolate the high-angle diffraction data beyond the detector, which can be applied to numerically verify the argument. If reconstruction artefacts still remain visible after resolving the high-angle scattering issue, multiple scattering contributions also need to be considered. A proposed solution would be modifying the forward model by dividing the surface exit wave into single scattering and multiple scattering parts. The single scattering part can be modeled in the usual way as a product of the probe and the object, while the multiple scattering part can be modeled as coherent noise. In addition, if depolarization effects are also

considered, the multiple scattering part can be modeled as a combination of coherent and incoherent noise.

7.3.2 *Computational OCT for rough surfaces*

To investigate an imaging method, we also apply computational OCT for surface roughness characterization. Measurements are performed using the computational OCT setup as shown in Fig. 3.4, Chap. 3. Here we present TDOCT measurements on a steel surface, where 400 images are recorded in a z-scan with a step size of 150 nm. The sample is directly measured in the image plane, thus no numerical focusing is needed. Following the reconstruction method described in Chap. 3, we obtain a 3D distribution of the surface $I(x, y, z)$ with a depth resolution of 3.5 µm. To obtain a height map of the surface, we calculate the center of mass in the z direction:

$$Z(x, y) = \frac{\int zI(x, y, z)dz}{\int I(x, y, z)dz}. \tag{7.4}$$

Surface tilts are removed using the Normal equation as explained in Appx. h.4. The reconstructed height map of the surface is shown in Fig. 7.2(a), which agrees well with the height map in Fig. 7.2(b) provided by Tata Steel measured with a confocal instrument. The extracted S_a values are 2.75 µm and 2.69 µm from the TDOCT and confocal microscopy methods respectively, which also confirms the good agreement between the two methods.

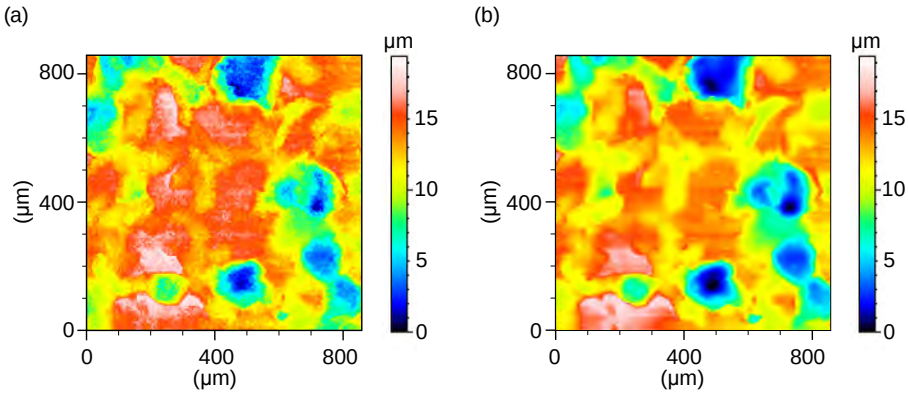

Figure 7.2: (a) Topographic measurement of a steel surface using TDOCT. (b) Topographic measurement of the same area as in (a) performed at Tata Steel using confocal scanning microscopy.

Compared to less-successful ptychographic reconstructions discussed in Sec. 7.3.1, computational OCT seems to perform better on rough surfaces, especially on surfaces with a S_a value larger than the optical wavelength. As an example, for the surface shown in Fig. 7.2, ptychography fails to converge to a physical solution. One possible explanation is that the NA is more than two times larger in the

OCT system as compared to the lensless ptychography setup. This supports the argument that the failed ptychographic reconstruction is caused by the mismatch between the forward model and experimental data due to the incomplete detection of the scattering angles. However, we also observed that if computational OCT measurements are performed not directly in the image plane of rough surfaces, it is very challenging to find back the focal plane through numerical refocus, which could be explained by the scrambled phase caused by multiple scattering. In order to understand the problem better, further systematic studies need to be carried out.

7.4 STATISTICAL PROPERTIES OF ROUGH SURFACES: POLYCHROMATIC SPECKLE CONTRAST

When laser light reflects from a rough surface, or transmits through a diffuser, a granular speckle pattern is often observed. Since the invention of lasers in the 1960s, many studies on speckle phenomena have been carried out both theoretically and experimentally. The formation of optical speckles are subject to light coherence and diffusive objects. In fact, speckle patterns are used to study both coherence properties of light and properties of objects that the light interacts with. Both spatial and spectral speckle correlations have been investigated to provide statistical information about rough surfaces [217]. Here we focus on speckle contrast, or more specifically on changes of speckle contrast as a function of optical source bandwidth, for surface roughness characterization.

7.4.1 *Speckle contrast*

When the intensity fluctuation I of a speckle pattern is measured, the average speckle contrast, or visibility, is given by the normalized standard deviation of the speckle intensity:

$$V = \frac{\sigma_I}{<I>}, \tag{7.5}$$

where σ_I is the standard deviation, and $<I>$ is the mean of the intensity. The relation between surface roughness and speckle contrast under monochromatic illumination has been studied experimentally [219, 220]. As a perfectly smooth surface produces a smooth intensity pattern, the speckle contrast is zero. With an increasing surface roughness, the height fluctuations lead to phase fluctuations of the reflected light, which further lead to intensity fluctuations upon propagation, resulting in an increase in speckle contrast. When the surface roughness becomes comparable to a quarter of the wavelength, which means that the height variation of the surface is large enough to form complete destructive interference, fully developed speckles form and the speckle contrast saturates. Thus, for low-roughness surfaces, where a monotonic relation holds, monochromatic speckle contrast measurements can be used to characterize the surface roughness [219].

For rough surfaces that produce fully developed speckles, it is useful to vary the coherence properties of the light. Correlations between surface roughness and spatially or temporally varying illuminations have been studied [217]. Here

we focus on spectral correlation. Goodman first formulated calculations on cross correlation of speckle patterns produced by different wavelengths, which show that the degree of correlation is dependent on the surface roughness [221]. It was first experimentally demonstrated in 1972 by Sprague that the contrast of speckle patterns measured using white light monotonically decreases with increasing surface roughness [222]. Speckle decorrelation with increasing wavelength differences is proposed for speckle noise reduction [223]. More theoretical studies followed to quantify the correlation between surface roughness and the contrast of speckle patterns produced by broadband light [224–226].

Polychromatic speckle patterns are calculated as an incoherent sum of individual monochromatic speckle patterns:

$$I = \int S(k)I(k)d(k), \tag{7.6}$$

where $k = \frac{2\pi}{\lambda}$ is the wavenumber, $S(k)$ is the spectral density function. The visibility of polychromatic speckle patterns is expressed as:

$$V^2 = \frac{\sigma_I^2}{< I >^2} = \frac{\iint S(k_1)S(k_2) < I(k_1)I(k_2) > dk_1 dk_2}{[\int S(k) < I(k) > dk]^2}, \tag{7.7}$$

where $< I(k_1)I(k_2) >$ is the spectral correlation. Intuitively, speckle patterns decorrelate faster for surfaces with higher roughness values. The variation in correlation among all monochromatic speckle patterns gives rise to the final contrast difference in the polychromatic speckle patterns. Due to the complexity of the problem, many statistical assumptions have to be applied to obtain a simple analytical solution, including a normally distributed surface height fluctuation, a Gaussian spectrum, negligible multiple scattering, normal incidence illumination with plane waves, and on-axis detection. Here we directly use the final simplified expression [225–227] for the contrast V of a polychromatic speckle pattern measured in the far-field as a function of spectral bandwidth W in wavenumber and the surface roughness S_q:

$$V^2 = \frac{1}{\sqrt{1 + (2W\sigma_l)^2}} = \frac{1}{\sqrt{1 + (4WS_q)^2}}, \tag{7.8}$$

where σ_l is the standard deviation of optical path length variations caused by rough surfaces. If only specular reflection is considered, σ_l is directly related to the standard deviation of the height distribution as $\sigma_l = 2\sigma_z = 2S_q$. In the case where non-specular reflection is considered, σ_l^2 also has contributions from light scattered transversely, which is dependent on the aperture size of the system [226, 227]. Here we propose a more general model:

$$V^2 = \frac{1}{\sqrt{1 + W^2(a + bS_q)^2}}, \tag{7.9}$$

where a represents a statistical factor for transverse optical path length fluctuation, and b is the ratio between the vertical optical path length fluctuation and the vertical height variation of the surface, and W is the illumination bandwidth in wavenumber. In the following section, we test the model with experimental data to see if it can be applied as a general model for predicting surface roughness from polychromatic speckle contrast measurements.

7.4.2 *Preliminary results on speckle contrast measurement*

We measure speckle patterns of rough steel surfaces as a function of wavelength, from which we calculate speckle contrast curves. Using roughness values obtained from OCT measurements on the same samples, we fit the experimental data to the model (Eq. 7.9) introduced in Sec. 7.4.1. From these fits we retrieve the coefficients a and b that best describe the roughness of our samples according to Eq. 7.9.

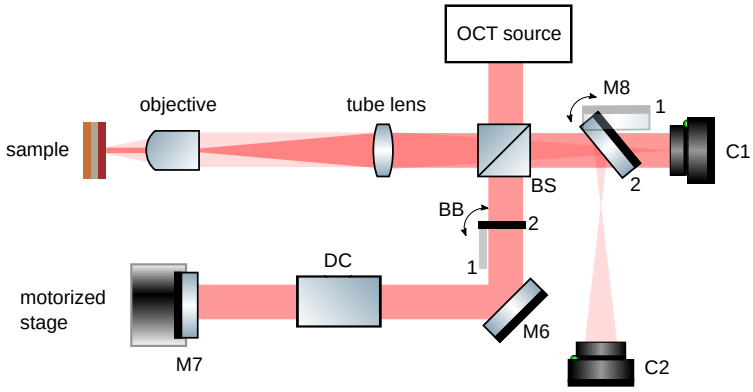

Figure 7.3: Schematic of OCT-speckle measurement setup. Based on the computational OCT setup, a flippable Mirror (M8), a beam block (BB), and a second camera (C2) are added to perform the speckle measurements. For OCT measurements, M8 and BB are at position 1, and for speckle measurements, M8 and BB are at position 2.

The computational OCT setup (Fig. 3.4) is modified as shown in Fig. 7.3 to perform SSOCT and speckle measurements sequentially on the same part of the sample under the same illumination conditions. For speckle measurements, a flip mirror *M8* is added to direct light to the added camera *C2*, which records speckle patterns in the far-field. The beam block (BB) is added to block the reference, thus only back reflected light from the object is measured. Six different steel surfaces with an S_q value ranging from 0.6 µm to 2.4 µm are investigated. On each surface, 10 different areas are measured to account for regional variations. The height map of each measurement is reconstructed using SSOCT, from which the roughness S_q is calculated as described in Sec. 7.3.2. Examples of six surface reconstructions are shown in Fig. 7.4, and the S_q values are the average values among 10 measurements of each surface. At each location, we record 21 quasi-monochromatic ($\lambda/\Delta\lambda > 1000$) speckle patterns from 700 nm to 800 nm with a 5 nm step size. Then we sum up monochromatic speckle patterns to obtain intensities of polychromatic speckle patterns, from which speckle contrast is calculated using Eq. 7.5.

In Fig. 7.5(a) and (b), we show the speckle pattern evolution for two rough surfaces as a function of illumination bandwidth $\Delta\lambda = 1, 20, 40, 60, 80, 100$ nm. The speckle patterns change faster for the rougher surface (Fig. 7.5(a)) with increasing bandwidths. Figure 7.5(c) and (d) show the full frames of two types of

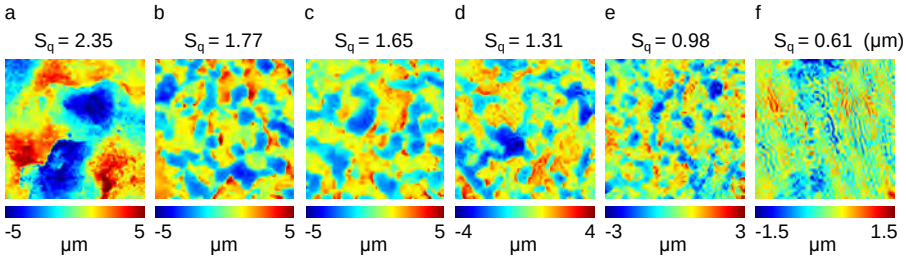

Figure 7.4: Surface height reconstructions of six different steel surfaces obtained with SSOCT, presented in order of descending S_q. The transverse scale of the height maps is 416×416 μm.

speckle patterns used to calculate the contrast curve, and the results are shown in Fig. 7.5(e), where W is the bandwidth in wavenumber.

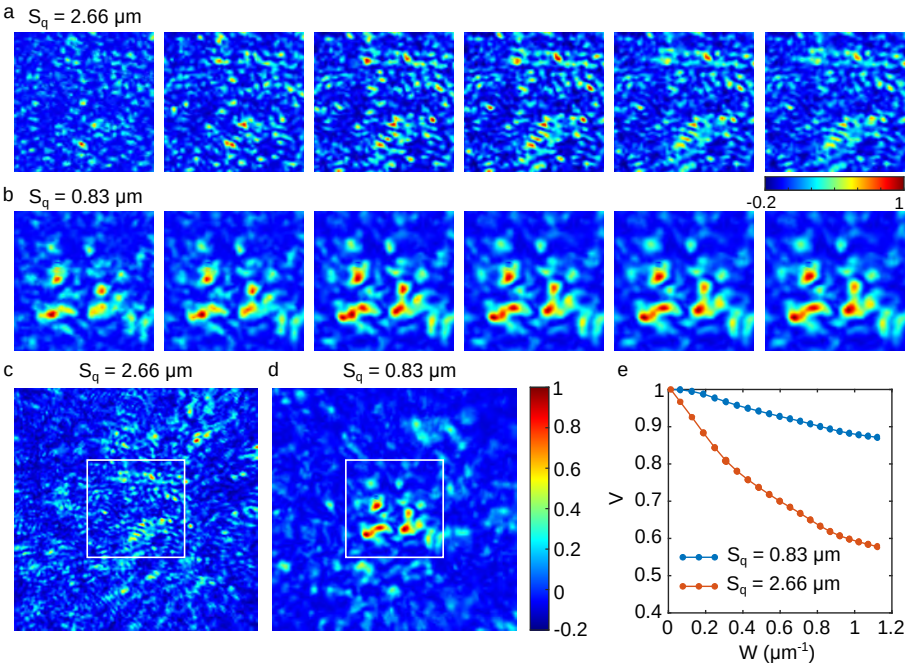

Figure 7.5: Polychromatic speckle patterns. (a),(b) Speckle pattern evolution as a function of illumination bandwidth ($\Delta\lambda = 1, 20, 40, 60, 80, 100$ nm) for two rough surfaces respectively. (c),(d) Full frames of speckle patterns used to calculated speckle contrast. The transverse scale is 3.3×3.3 mm.The center part marked with the white squares are the zoomed in parts in (a) and (b). (e) Calculated speckle contrast curves as a function of illumination bandwidth in wavenumber for two surfaces.

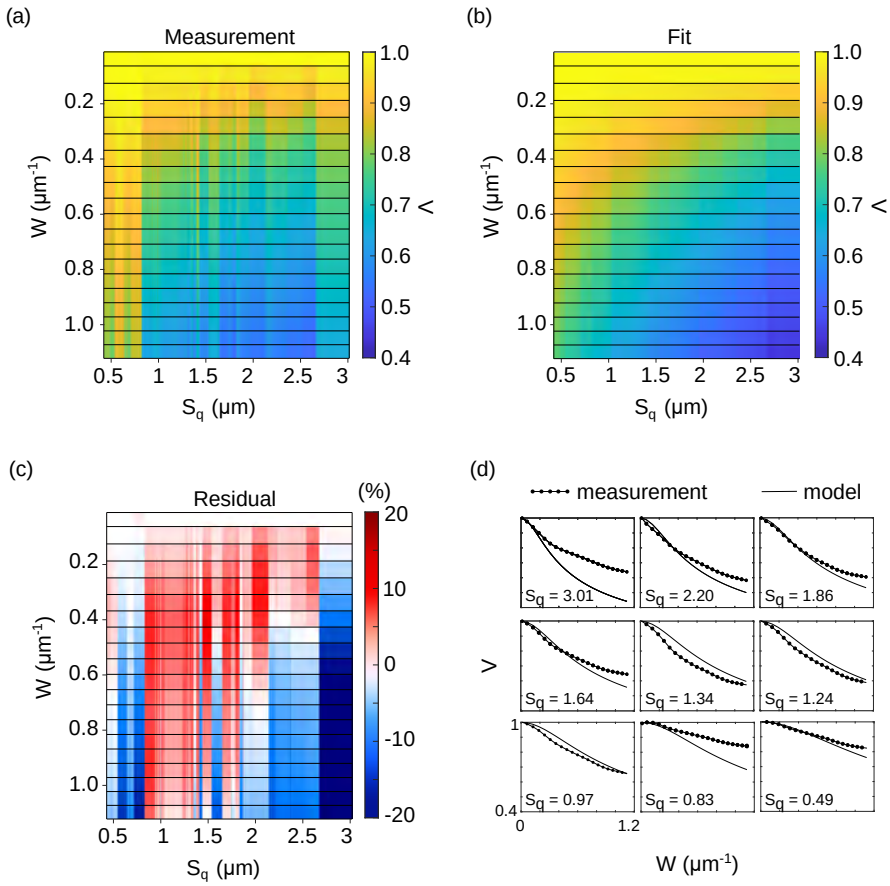

Figure 7.6: Model fit of polychromatic speckle contrast. (a) 51 speckle contrast measurements are shown. The x-axis is the S_q obtained from SSOCT measurements. The vertical lines shows the sampling in S_q. The y-axis is the bandwidth in wavenumber. The color represents the contrast values V. (b) The fit surface from the model in Eq. 7.9. (c) The residuals in percentage calculated from (Fit-Measurement)/Measurement. (d) Nine examples of measured and fit speckle contrast curves for different roughness values.

In total we obtain 51 speckle contrast curves, which are combined in Fig 7.6(a), and the contrast is shown as colors. We fit the model to the surface containing 51 curves (Eq. 7.9) using nonlinear least squares regression, and obtain the parameters $a = 0.63\,\mu\text{m}$ and $b = 1.28$ with an adjusted R^2 value of 0.89. With the fitted parameters, we calculate the expected speckle contrast shown in Fig. 7.6(b) according to the model (Eq. 7.9), and the residuals are plotted in Fig. 7.6(c). The general trend is that the speckle contrast monotonically decreases with increasing bandwidth, and decreases faster for rougher surfaces, which is captured by the fit. However, discrepancies between the measurement and the fit can be observed. For surfaces with roughness values at two edges of the measurements, below

1 µm and above 2.5 µm, the speckle contrast estimated from the model is mainly lower than the measurements, shown as blue in the residual plot (Fig. 7.6(c)). For S_q between 1 µm and 1.8 µm, the model tends to result in higher contrast values, shown as red in Fig. 7.6(c). This can also be observed in Fig. 7.6(d), where the fitted curves are above the measurement curves in this roughness region.

With the determined parameters a and b, we calculate the surface roughness S_q given the speckle contrast curves via a non-linear least squares fit to Eq. 7.9, and compare the resulting roughness with the value obtained from OCT measurements. The results are shown in Fig 7.7, where the error bars show the 95% confidence intervals. This shows that the model underestimate the surface roughness for values below 1 µm, which confirms that the model does not cover this regime very well. One explanation can be that for surfaces with such low roughness values, the measured spectral range is not wide enough. As can be seen in Fig. 7.6(d), for $S_q = 0.83$ µm and 0.49 µm the measured speckle contrast curves are very similar, both only showing a small decrease from 1 to 0.8. Thus by expanding the measurement bandwidth, differences may be captured to distinguish one from the other. For surface roughness in between 1 µm and 2.5 µm, the model tends to predict a higher roughness value than the OCT measurements, as data points above the red diagonal line are two times the ones below.

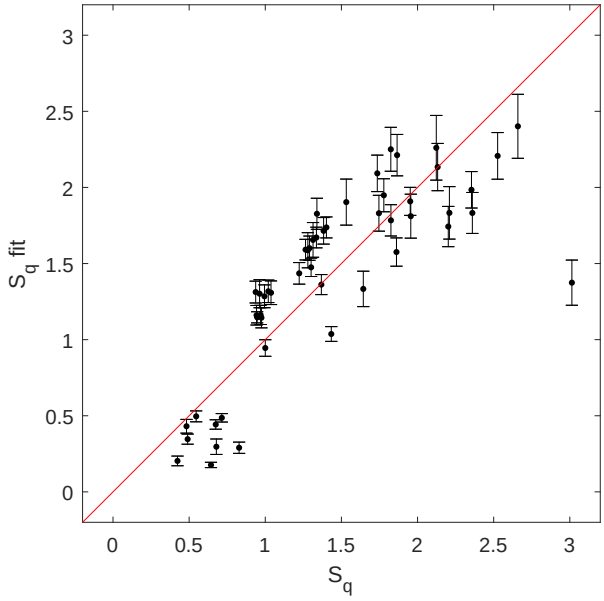

Figure 7.7: Comparison of surface roughness obtained from OCT and the model. Error bars indicate 95% confidence intervals.

To conclude, the model captures the general trend between the visibility of polychromatic speckles patterns and the surface roughness. However, it provides limited prediction power, which can be explained by the following reasons. On the experiment side, both OCT and speckle measurements show inconsistencies, possibly due to the small amount of sampling. More measurements with larger

measurement ranges in both illumination bandwidth and roughness values are needed to further verify the method. On the modeling side, as we have mentioned in Sec. 7.4.1, the model itself in Eq. 7.8 is derived under many assumptions, some of which are not fulfilled in our experiments. For example, the model assumes a normally distributed surface height variation. We measured industrial steel surfaces produced by deterministic processes, thus it is likely that the height fluctuations do not follow Gaussian distributions. Also, the model assumes a continuous Gaussian spectrum for the illumination, and we used discrete spectral lines. Furthermore, in our generalized model (Eq. 7.9), constant parameters a and b are assumed to relate the surface roughness to optical path length changes, which are possibly surface-dependent and therefore not constant. Additionally, multiple scattering, shadowing, and depolarization effects are all neglected in this model, and are often neglected in modeling speckle scattering. Overall, the preliminary results show that it is challenging to find a universal, applicable physical model to relate speckle contrast only to surface roughness. An alternative approach is to explore deep learning methods to circumvent the need for an analytical physical model. Advanced machine-learning algorithms, such as convolutional neural networks and linear discriminant analysis, have been successfully applied for scatterer recognitions from seemingly random speckle patterns [228]. The ability of machine learning techniques to retrieve statistical properties of the scattering object has, to the best of our knowledge, not yet been demonstrated.

Part III

APPENDIX

h

APPENDIX

H.1 LENS TRANSFORMATION

Derivations of wavefields propagating through a thin lens under paraxial approximation is presented. As shown in Fig. 2.4 in Sec. 2.1.4, an object $E(x^{'}, y^{'}, 0)$ is at a distance d_1 in front of a lens with a focal length of f. The detection plane is at a distance d_2 behind the lens. Using Fresnel propagation, we first propagate the object field $E(x^{'}, y^{'}, 0)$ to the lens plane:

$$E_l(x^l, y^l, z_1) = \frac{e^{ikd_1}}{i\lambda d_1} e^{i\frac{k}{2d_1}(x^{l2}+y^{l2})} \times \iint_{-\infty}^{\infty} \left\{E(x^{'}, y^{'}, 0) e^{i\frac{k}{2d_1}(x^{'2}+y^{'2})}\right\} e^{-i\frac{k}{d_1}(x^l x^{'}+y^l y^{'})} dx^{'} dy^{'}, \quad \text{(h.1)}$$

where $E_l(x^l, y^l, z_1)$ is the wavefield at the front side of the lens, and we assume the extent of E_l is small compared to the lens. Following the lens transformation rule (Eq. 2.27), the wavefield at the back side of the lens is given by:

$$\begin{aligned} E_l^{'}(x^l, y^l, z_1) &= E_l(x^l, y^l, z_1) t_l(x^l, y^l) \\ &= \frac{e^{ikd_1}}{i\lambda d_1} e^{i\frac{k}{2f}(\frac{f}{d_1}-1)(x^{l2}+y^{l2})} e^{ikn\Delta_0} \\ &\quad \times \iint_{-\infty}^{\infty} \left\{E(x^{'}, y^{'}, 0) e^{i\frac{k}{2d_1}(x^{'2}+y^{'2})}\right\} e^{-i\frac{k}{d_1}(x^l x^{'}+y^l y^{'})} dx^{'} dy^{'}. \end{aligned} \quad \text{(h.2)}$$

By propagating $E_l^{'}(x^l, y^l, z_1)$ over a distance d_2, we obtain the wavefield at the observation plane:

$$\begin{aligned} E(x, y, z_2) =& \frac{e^{ikd_2}}{i\lambda d_2} e^{i\frac{k}{2d_2}(x^2+y^2)} \\ &\times \iint_{-\infty}^{\infty} \left\{E_{l2}(x^l, y^l, z_1) e^{i\frac{k}{2d_2}(x^{l2}+y^{l2})}\right\} e^{-i\frac{k}{d_2}(x^l x+y^l y)} dx^l dy^l \\ =& A_0 \iint_{-\infty}^{\infty} E(x^{'}, y^{'}, 0) e^{i\frac{k}{2d_1}(x^{'2}+y^{'2})} dx^{'} dy^{'} \\ & \iint_{-\infty}^{\infty} e^{i\frac{k}{2f}(\frac{f}{d_1}+\frac{f}{d_2}-1)(x^{l2}+y^{l2})} e^{-i\frac{k}{d_2}(x^l x+y^l y)} e^{-i\frac{k}{d_1}(x^l x^{'}+y^l y^{'})} dx^l dy^l, \end{aligned} \quad \text{(h.3)}$$

where

$$A_0 = \frac{e^{ikd_2}}{i\lambda d_2} \frac{e^{ikd_1}}{i\lambda d_1} e^{ikn\Delta_0} e^{i\frac{k}{2d_2}(x^2+y^2)}. \quad \text{(h.4)}$$

We can simplify the integral over (x^l, y^l) using the Fourier transform relation:

$$\iint_{-\infty}^{\infty} e^{i\frac{k}{2f}(\frac{f}{d_1}+\frac{f}{d_2}-1)(x^{l2}+y^{l2})} e^{-i\frac{k}{d_2}(x^l x+y^l y)} e^{-i\frac{k}{d_1}(x^l x'+y^l y')} dx^l dy^l$$
$$= \frac{i2\pi}{k(\frac{1}{d_1}+\frac{1}{d_2}-\frac{1}{f})} e^{\frac{-ik}{2(\frac{1}{d_1}+\frac{1}{d_2}-\frac{1}{f})}[(\frac{x'}{d_1}+\frac{x}{d_2})^2+(\frac{y'}{d_1}+\frac{y}{d_2})^2]}. \tag{h.5}$$

Thus we obtain the final expression:

$$E(x,y,z_2) = A\iint_{-\infty}^{\infty} E(x',y',0) e^{ikB(x'^2+y'^2)} e^{\frac{-ikf}{fd_1+fd_2-d_1d_2}(xx'+yy')} dx'dy', \tag{h.6}$$

where

$$A = A_0 \frac{i2\pi}{k(\frac{1}{d_1}+\frac{1}{d_2}-\frac{1}{f})} e^{\frac{-ikfd_1}{2d_2(fd_1+fd_2-d_1d_2)}(x^2+y^2)}, \tag{h.7}$$

$$B = \frac{1}{2d_1} - \frac{fd_2}{2d_1(fd_1+fd_2-d_1d_2)}. \tag{h.8}$$

H.2 PRACTICAL CONSIDERATIONS FOR PTYCHOGRAPHY

Non-uniqueness

If $P(\mathbf{r})$ and $O(\mathbf{r})$ are solutions of the ptychographic reconstruction, then $cP(\mathbf{r})$ and $c^{-1}O(\mathbf{r})$ with a constant scaling factor or a flat phase offset are also solutions, and $P(\mathbf{r}-\mathbf{a})$ and $O(\mathbf{r}-\mathbf{a})$ with a constant lateral shift are also solutions.

Absorbed phase term

The Fresnel integral propagator used in ptychographic reconstruction is:

$$\tilde{\psi}(\mathbf{q}) = \iint_{-\infty}^{\infty} \left\{ O(\mathbf{r}) P(\mathbf{r}) e^{i\frac{k}{2z}(x^2+y^2)} \right\} e^{-i\frac{k}{z}(xq_x+yq_y)} dxdy. \tag{h.9}$$

Compared to the complete form of the Fresnel integral (see Eq. 2.14), the phase term outside the integral is neglected since only intensities are measured. For calculation efficiency, the quadratic phase term inside the integral in Eq. h.2 can be absorbed into the probe:

$$P_{new} = P(\mathbf{r}) e^{i\frac{k}{2z}(x^2+y^2)}. \tag{h.10}$$

Thus the Fresnel integral is simplified into a direct Fourier transform:

$$\tilde{\psi}(\mathbf{q}) = \mathcal{F}^2_{\mathbf{r}\to\mathbf{q}} \left\{ O(\mathbf{r}) P_{new}(\mathbf{r}) \right\}. \tag{h.11}$$

Note that the quadratic phase has to be corrected after the reconstruction to obtain the real quantitative information of the probe beam.

Initial guess

Although ptychography does not require a priori knowledge about the illumination beam, starting with a good initial guess can help to speed up the convergence rate. For a smooth beam, having a good estimate of the beam diameter is already advantageous, and for a structured beam, a good estimate of its global phase curvature can be very beneficial. For the object, the initial guess is normally filled with ones.

Scan grid

It has been shown that periodic scanning grids introduce artefacts in the reconstruction [229]. Thus aperiodic scan grids are often used with the advantage that they can be generated in a deterministic way. In the thesis, we used Fermat spiral scanning patterns. One example is shown in Fig. h.1(a). In order to save the total travel time of the scanning stage in a ptychography measurement, the order of the scan positions are optimized using a genetic algorithm for solving the traveling salesman problems [230]. The scan trajectory before and after the optimization is shown in Fig. h.1(b) and (c), respectively.

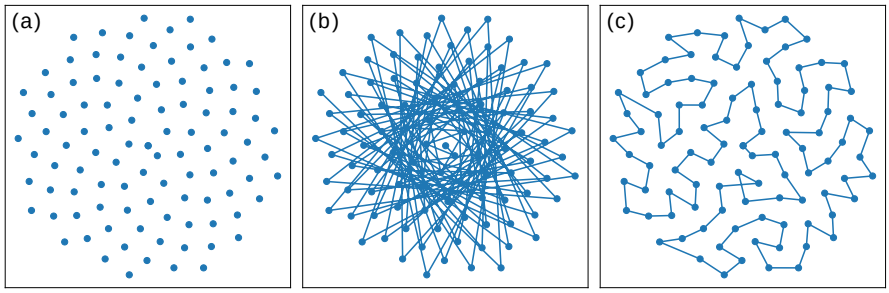

Figure h.1: Fermat spiral scanning pattern.

Fourier ring correlation

Fourier ring correlation (FRC) is often used to evaluate the reconstruction resolution in ptychography [134, 231]. In general, FRC [153, 232] compares two functions by calculating their cross-correlation coefficient on rings in Fourier space, finding the highest spatial frequency at which two functions are correlated[1]

$$FRC(r_i) = \frac{\sum_{r \in r_i} F_1(r) \cdot F_2(r)^*}{\sqrt{\sum_{r \in r_i} F_1(r)^2 \cdot \sum_{r \in r_i} F_2(r)^2}} \tag{h.12}$$

In ptychography, this is a very useful way to determine reproducible resolutions across multiple independent reconstructions. A proper threshold criteria for determining the cut-off frequency is discussed in [154], where noise statistics and number of pixels in rings are taken into consideration.

1 In the case of comparing two 3D functions, sub-correlations are calculated on shells in the 3D Fourier space, which is called Fourier shell correlation [233].

H.3 SAMPLE FABRICATION

Sample fabrication is carried out at AMOLF NanoLab Amsterdam (ISO class 5 cleanroom). Established recipes are described below:

- Substrate cleaning and preparation

Menzel glass coverslips (24*24*0.17 mm) are used as substrates for the samples. We clean glass substrates in two steps: 1) Sonication; 2) Base Piranha cleaning. Base Pirahna is a mixture of H_2O, 30% ammonium hydroxide (NH_4OH) and 30% hydrogen peroxide (H_2O_2) in a ratio of 5:1:1. We follow the standard procedure: First, mix H_2O and the NH_4OH solution and heat the mixture up to 75 °C, then add the H_2O_2 solution to the mixture and reheat up to 75 °C. Finally immerse the substrates in the mixture for 15 minutes, and afterwards rinse the substrates in H_2O and isopropanol. NH_4OH is a strong complexant for removing metal particles, while H_2O_2 is a powerful oxidant at high pH for removing organic residues.

- UV lithography

To prepare the photoresist we spincoat photoresist S1813 at 4000 rpm (with 1000 rpm/s acceleration, close lid) for 40 seconds, then bake the sample on a hotplate at 115 °C for 2 minutes. This results in a homogeneous resist layer of 680 nm thick, which is more than 5 times thicker than the final metal structure to ensure a successful liftoff. Secondly, the sample is exposed under 300 nm UV light (Suss MABA6 Mask aligner) for 4.5 seconds (total energy 112.5 mJ). In this way, the desired pattern is transfered from the mask to the resist layer by selectively changing the solubility of the resist layer. Lastly, the sample is developed in the developer solution (MF-319) for 45 seconds, then rinsed in water for 45 seconds. At this stage, physical structures are formed in the resist layer, which can be checked under an optical microscope with UV filters to prevent blue light from further exposing the resist.

- Thermal Deposition and lift-off

We use a home-built thin-film thermal evaporator Nanoontje to deposit different metals on the sample. The source metal is heated up and evaporates in a high vacuum environment (10^{-7}mbar). Due to the long distance (about one meter) between the source and the sample, the evaporated metal particles are deposited homogeneously on the sample surface. The final lift-off step is done in Acetone at room temperature. 15 to 20 seconds of sonication can speed up the lift-off process. After 10 to 15 minutes, we rinse the sample in isopropanol to remove the lift-off residuals and check the results under an optical microscope.

- Intermediate layers

In order to build up multiple layers, we use transparent (in visible and infrared) photo-resist as intermediate material. Two different negative photo-resists (SU-8 and Ormocomp) have been tested for this purpose. SU-8 is more rigid, resulting in cracks in about 40 µm thick layers, which can be seen in Fig. 3.7 (c,d) and (g,f). In contrast, Ormocomp results in more homogeneous intermediate layers (Fig. 3.8 (c-j)). Also, Ormocomp is less dispersive than SU-8 in the detection wave-

length range used in the experiments. In order to spincoat a homogeneous layer, we first dilute Ormocomp in OrmoThin with a ratio of 1:1 in a heated water bath at 35 °C. The mixing is assisted by magnetic stirring. Then we spincoat the resist solution at 1000 rpm (with 100 rpm/s acceleration) for 40 seconds. Afterwards, the sample is baked at 80 °C for 10 minutes. Finally, the sample is exposed using a UV lithography machine under the flood exposure mode for 60 seconds and baked at 130 °C for 10 minutes to form a solid layer, upon which a new layer of structures can be fabricated by repeating the aforementioned procedures.

One of the difficulties in the multi-layer sample fabrication is to control the alignment between different layers. Our solution is to design markers around the desired structures on the mask and utilize the built-in microscope of the UV lithography machine. The other difficulty we encountered is that due to the edge effect of the substrate, the intermediate layer is thinner in the center and thicker near the edges. Thus pre- and post-exposure baking becomes extremely important.

H.4 TILT CORRECTION

The problem of correcting for a linear tilt in a 2D height map belongs to a general problem called multivariate linear regression. Assume we have a $M \times M$ 2D height map, for each pixel i with coordinates of (x_1^i, x_2^i), we want to find the coefficients $(\theta_0, \theta_1, \theta_2)$ that give the estimated height:

$$\theta_0 + x_1^i \theta_1 + x_2^i \theta_2 = y_{est}^i. \tag{h.13}$$

We can arrange the indices of all pixels into a matrix X of shape $M^2 \times 3$, where the first column of X is ones, the second column of X is the first indices of all the pixels, and the third column is the second indices of the all the pixels. Thus the estimated height is expressed as:

$$X\theta = y_{est}. \tag{h.14}$$

We also arrange all the measured height values into a vector y. To minimize the residual between the measured height and the estimated height $y - X\theta$, assuming a Gaussian distribution, we use the least square minimization:

$$J(\theta) = (y - X\theta)^2 = (y - X\theta)(y - X\theta)^T. \tag{h.15}$$

Then we calculate the gradient of the residual $J(\theta)$ with respect to θ, and assign it to zero:

$$\Delta_\theta J(\theta) = 0, \tag{h.16}$$

which gives us the solution of θ:

$$\theta = (X^T X)^{-1} X^T y. \tag{h.17}$$

This is called the Normal equation. Thus the estimated tilt plane can be calculated from Eq. h.4. The height map after tilt correction is given by the residual term in Eq. h.4.

BIBLIOGRAPHY

1. Abbe, E. Beiträge zur Theorie des Mikroskops und der mikroskopischen Wahrnehmung. *Archiv für mikroskopische Anatomie* **9,** 413–468 (1873).
2. Huang, D., Swanson, E. A., Lin, C. P., Schuman, J. S., Stinson, W. G., Chang, W., Hee, M. R., Flotte, T., Gregory, K. & Puliafito, C. A. Optical coherence tomography. *Science* **254,** 1178 –1181 (1991).
3. Fercher, A. F. Optical coherence tomography. *Journal of Biomedical Optics* **1,** 157–173 (1996).
4. Wojtkowski, M. High-speed optical coherence tomography: basics and applications. *Applied Optics* **49,** D30–D61 (2010).
5. Assayag, O., Antoine, M., Sigal-Zafrani, B., Riben, M., Harms, F., Burcheri, A., Grieve, K., Dalimier, E., de Poly, B. L. C. & Boccara, C. Large Field, High Resolution Full-Field Optical Coherence Tomography: a Pre-Clinical Study of Human Breast Tissue and Cancer Assessment. *Technology in Cancer Research & Treatment* **13,** 455–468 (2014).
6. Spaide, R. F., Klancnik, J. M. & Cooney, M. J. Retinal vascular layers imaged by fluorescein angiography and optical coherence tomography. *JAMA Ophthalmology* **133,** 45–50 (2015).
7. Campbell, J. P., Zhang, M, Hwang, T. S., Bailey, S. T., Wilson, D. J., Jia, Y & Huang, D. Detailed Vascular Anatomy of the Human Retina by Projection-Resolved Optical Coherence Tomography Angiography. *Scientific Reports* **7,** 42201 (2017).
8. Hell, S. W. & Wichmann, J. Breaking the diffraction resolution limit by stimulated emission: stimulated-emission-depletion fluorescence microscopy. *Optics Letters* **19,** 780–782 (1994).
9. Hofmann, M., Eggeling, C., Jakobs, S. & Hell, S. W. Breaking the diffraction barrier in fluorescence microscopy at low light intensities by using reversibly photoswitchable proteins. *Proceedings of the National Academy of Sciences of the United States of America* **102,** 17565–17569 (2005).
10. Wicker, K., Mandula, O., Best, G., Fiolka, R. & Heintzmann, R. Phase optimisation for structured illumination microscopy. *Optics Express* **21,** 2032–2049 (2013).
11. Rust, M. J., Bates, M. & Zhuang, X. Sub-diffraction-limit imaging by stochastic optical reconstruction microscopy (STORM). *Nature Methods* **3,** 793–796 (2006).
12. Schmidt, R., Wurm, C. A., Jakobs, S., Engelhardt, J., Egner, A. & Hell, S. W. Spherical nanosized focal spot unravels the interior of cells. *Nature Methods* **5,** 539–544 (2008).
13. Shaevitz, J. W. Super-resolution for a 3D world. *Nature Methods* **5,** 471–472 (2008).
14. Schmidt, R., Wurm, C. A., Punge, A., Egner, A., Jakobs, S. & Hell, S. W. Mitochondrial cristae revealed with focused light. *Nano Letters* **9,** 2508–2510 (2009).
15. Xu, K., Babcock, H. P. & Zhuang, X. Dual-objective STORM reveals three-dimensional filament organization in the actin cytoskeleton. *Nature Methods* **9,** 185–188 (2012).
16. Jones, S. A., Shim, S. H., He, J. & Zhuang, X. Fast, three-dimensional super-resolution imaging of live cells. *Nature Methods* **8,** 499–505 (2011).
17. Berning, S., Willig, K. I., Steffens, H., Dibaj, P. & Hell, S. W. Nanoscopy in a living mouse brain. *Science* **335,** 551 (2012).

18. Masullo, L. A., Bodén, A., Pennacchietti, F., Coceano, G., Ratz, M. & Testa, I. Enhanced photon collection enables four dimensional fluorescence nanoscopy of living systems. *Nature Communications* **9,** 3281 (2018).
19. Carmignato, S., Dewulf, W. & Leach, R. *Industrial X-Ray Computed Tomography* (Cham: Springer International Publishing, 2018).
20. Dierolf, M., Menzel, A., Thibault, P., Schneider, P., Kewish, C. M., Wepf, R., Bunk, O. & Pfeiffer, F. Ptychographic X-ray computed tomography at the nanoscale. *Nature* **467,** 436–439 (2010).
21. Hegerl, R. & Hoppe, W. Dynamic theory of crystalline structure analysis by electron diffraction in inhomogeneous primary wave field. *Berichte der Bunsen-Gesellschaft für physikalische Chemie* **74,** 1148–1154 (1970).
22. Gerchberg, R. W. & Saxton, W. O. A practical algorithm for the determination of phase from image and diffraction plane pictures. *Optik* **35,** 237–246 (1972).
23. Ladd, M. & Palmer, R. *Structure Determination by X-ray Crystallography* 5th ed. (Springer, Boston, MA, 2013).
24. Miao, J., Charalambous, P., Kirz, J. & Sayre, D. Extending the methodology of X-ray crystallography to allow imaging of micrometre-sized non-crystalline specimens. *Nature* **400,** 342–344 (1999).
25. Miao, J., Ishikawa, T., Robinson, I. K. & Murnane, M. M. Beyond crystallography: Diffractive imaging using coherent X-ray light sources. *Science* **348,** 530–535 (2015).
26. Bates, R. H, T. Fourier phase problems are uniquely solvable in more than one dimension, 1. Underlying theory. *Optik* **61,** 247–262 (1982).
27. Fienup, J. R. Phase retrieval algorithms: a comparison. *Applied Optics* **21,** 2758–2769 (1982).
28. Abbey, B., Nugent, K. A., Williams, G. J., Clark, J. N., Peele, A. G., Pfeifer, M. A., de Jonge, M. & McNulty, I. Keyhole coherent diffractive imaging. *Nature Physics* **4,** 394–398 (2008).
29. Witte, S., Tenner, V. T., Noom, D. W. E. & Eikema, K. S. E. Lensless diffractive imaging with ultra-broadband table-top sources: From infrared to extreme-ultraviolet wavelengths. *Light: Science and Applications* **3,** e163 (2014).
30. Rodenburg, J. M. & Faulkner, H. M. L. A phase retrieval algorithm for shifting illumination. *Applied Physics Letters* **85,** 4795–4797 (2004).
31. Rodenburg, J. M. & Maiden, A. in *Springer Handbook of Microscopy* (eds Hawkes, P. W. & Spence, J. C. H.) 819–904 (Springer, 2019).
32. Zheng, G., Horstmeyer, R. & Yang, C. Wide-field, high-resolution Fourier ptychographic microscopy. *Nature Photonics* **7,** 739–745 (2013).
33. Liu, Y.-Z., South, F. A., Xu, Y., Carney, P. S. & Boppart, S. A. Computational optical coherence tomography [Invited]. *Biomedical Optics Express* **8,** 1549–1574 (2017).
34. Zhou, K. C., Qian, R., Degan, S., Farsiu, S. & Izatt, J. A. Optical coherence refraction tomography. *Nature Photonics* **13,** 794–802 (2019).
35. Zernike, F. Phase contrast, a new method for the microscopic observation of transparent objects. *Physica* **9,** 974–986 (1942).
36. Marrison, J., Räty, L., Marriott, P. & O'Toole, P. Ptychography–a label free, high-contrast imaging technique for live cells using quantitative phase information. *Scientific Reports* **3,** 2369 (2013).

37. McDermott, S. & Maiden, A. Near-field ptychographic microscope for quantitative phase imaging. *Optics Express* **26,** 25471–25480 (2018).

38. Goodman, J. W. *Introduction to Fourier optics* (Roberts and Company Publishers, 2005).

39. Matsushima, K. & Shimobaba, T. Band-limited angular spectrum method for numerical simulation of free-space propagation in far and near fields. *Optics Express* **17,** 19662 (2009).

40. Patorski, K. Fraunhofer Diffraction Patterns of Titled Planar Objects. *Optica Acta: International Journal of Optics* **30,** 673–679 (1983).

41. Leseberg, D. & Frère, C. Computer-generated holograms of 3-D objects composed of tilted planar segments. *Applied Optics* **27,** 3020 (1988).

42. Matsushima, K., Schimmel, H. & Wyrowski, F. Fast calculation method for optical diffraction on tilted planes by use of the angular spectrum of plane waves. *Journal of the Optical Society of America A* **20,** 1755 (2003).

43. Millane, R. P. Phase retrieval in crystallography and optics. *Journal of the Optical Society of America A* **7,** 394 (1990).

44. Gabor, D. A New Microscopic Principle. *Nature* **161,** 777–778 (1948).

45. Yamaguchi, I. & Zhang, T. Phase-shifting digital holography. *Opt. Lett.* **22,** 1268–1270 (1997).

46. Schnars, U. & Jüptner, W. Digital recording and numerical reconstruction of holograms. *Measurement Science and Technology* **13,** R85–R101 (2002).

47. Leith, E. N. & Upatnieks, J. Reconstructed Wavefronts and Communication Theory. *Journal of the Optical Society of America* **52,** 1123–1130 (1962).

48. Schnars, U. & Jüptner, W. Direct recording of holograms by a CCD target and numerical reconstruction. *Applied Optics* **33,** 179 (1994).

49. Schnars, U., Falldorf, C., Watson, J. & Jüptner, W. *Digital Holography and Wavefront Sensing* (Springer, Berlin, Heidelberg, 2015).

50. McNulty, I., Kirz, J., Jacobsen, C., Anderson, E. H., Howells, M. R. & Kern, D. P. High-resolution imaging by fourier transform X-ray holography. *Science* **256,** 1009–1012 (1992).

51. Guizar-Sicairos, M. & Fienup, J. R. Holography with extended reference by autocorrelation linear differential operation. *Optics Express* **15,** 17592 (2007).

52. Zhu, D., Guizar-Sicairos, M., Wu, B., Scherz, A., Acremann, Y., Tyliszczak, T., Fischer, P., Friedenberger, N., Ollefs, K., Farle, M., Fienup, J. R. & Stöhr, J. High-resolution X-ray lensless imaging by differential holographic encoding. *Physical Review Letters* **105,** 043901 (2010).

53. Tenner, V. T., Eikema, K. S. E. & Witte, S. Fourier transform holography with extended references using a coherent ultra-broadband light source. *Optics Express* **22,** 25397 (2014).

54. Fienup, J. R. Reconstruction of an object from the modulus of its Fourier transform. *Optics Letters* **3,** 27 (1978).

55. Sayre, D. in *Imaging Processes and Coherence in Physics. Springer, Berlin,* 229–235 (Springer, Berlin, Heidelberg, 1980).

56. Cederquist, J. N., Fienup, J. R., Marron, J. C. & Paxman, R. G. Phase retrieval from experimental far-field speckle data. *Optics Letters* **13,** 619 (1988).

57. Sandberg, R. L., Paul, A., Raymondson, D. A., Hädrich, S., Gaudiosi, D. M., Holtsnider, J., Tobey, R. I., Cohen, O., Murnane, M. M., Kapteyn, H. C., Song, C., Miao, J., Liu, Y. & Salmassi, F. Lensless diffractive imaging using tabletop coherent high-harmonic soft-X-ray beams. *Physical Review Letters* **99,** 098103 (2007).

58. Bates, R. H. Uniqueness of solutions to two-dimensional fourier phase problems for localized and positive images. *Computer Vision, Graphics and Image Processing* **25,** 205–217 (1984).

59. Shannon, C. E. Communication in the presence of noise. *Proceedings of the IEEE* **86,** 447–457 (1998).

60. Miao, J., Sayre, D. & Chapman, H. N. Phase retrieval from the magnitude of the Fourier transforms of nonperiodic objects. *Journal of the Optical Society of America A* **15,** 1662 (1998).

61. Miao, J. & Sayre, D. On possible extensions of X-ray crystallography through diffraction-pattern oversampling. *Acta Crystallographica Section A: Foundations of Crystallography* **56,** 596–605 (2000).

62. Fienup, J. R., Crimmins, T. R. & Holsztynski, W. Reconstruction of the Support of an Object From the Support of Its Autocorrelation. *Journal of the Optical Society of America* **72,** 610–624 (1982).

63. Fienup, J. R. & Wackerman, C. C. Phase-retrieval stagnation problems and solutions. *Journal of the Optical Society of America A* **3,** 1897 (1986).

64. Fienup, J. R. Reconstruction of a complex-valued object from the modulus of its Fourier transform using a support constraint. *Journal of the Optical Society of America A* **4,** 118 (1987).

65. Fienup, J. R. & Kowalczyk, A. M. Phase retrieval for a complex-valued object by using a low-resolution image. *Journal of the Optical Society of America A* **7,** 450 (1990).

66. Marchesini, S., He, H., Chapman, N., Hau-Riege, P., Noy, A., Howells, R., Weierstall, U. & Spence, H. X-ray image reconstruction from a diffraction pattern alone. *Physical Review B - Condensed Matter and Materials Physics* **68,** 140101 (2003).

67. Zhang, Y., Pedrini, G., Osten, W. & Tiziani, H. J. Whole optical wave field reconstruction from double or multi in-line holograms by phase retrieval algorithm. *Optics Express* **11,** 3234 (2003).

68. Pedrini, G., Osten, W. & Zhang, Y. Wave-front reconstruction from a sequence of interferograms recorded at different planes. *Optics Letters* **30,** 833 (2005).

69. Bao, P., Zhang, F., Pedrini, G. & Osten, W. Phase retrieval using multiple illumination wavelengths. *Optics Letters* **33,** 309 (2008).

70. Bao, P., Situ, G., Pedrini, G. & Osten, W. Lensless phase microscopy using phase retrieval with multiple illumination wavelengths. *Applied Optics* **51,** 5486–5494 (2012).

71. Noom, D. W. E., Boonzajer Flaes, D. E., Labordus, E., Eikema, K. S. E. & Witte, S. High-speed multi-wavelength Fresnel diffraction imaging. *Optics Express* **22,** 30504 (2014).

72. Noom, D. W. E., Eikema, K. S. E. & Witte, S. Lensless phase contrast microscopy based on multiwavelength Fresnel diffraction. *Optics Letters* **39,** 193 (2014).

73. Zhang, F., Pedrini, G. & Osten, W. Phase retrieval of arbitrary complex-valued fields through aperture-plane modulation. *Physical Review A - Atomic, Molecular, and Optical Physics* **75,** 043805 (2007).

74. Gao, P., Pedrini, G., Zuo, C. & Osten, W. Phase retrieval using spatially modulated illumination. *Optics Letters* **39,** 3615 (2014).

75. Nugent, K. A., Peele, A. G., Chapman, H. N. & Mancuso, A. P. Unique phase recovery for nonperiodic objects. *Physical Review Letters* **91,** 203902 (2003).

76. Williams, G. J., Quiney, H. M., Dhal, B. B., Tran, C. Q., Nugent, K. A., Peele, A. G., Paterson, D. & De Jonge, M. D. Fresnel coherent diffractive imaging. *Physical Review Letters* **97,** 025506 (2006).

77. Gao, P., Pedrini, G. & Osten, W. Phase retrieval with resolution enhancement by using structured illumination. *Optics letters* **38,** 5204–5207 (2013).

78. Thibault, P., Dierolf, M., Menzel, A., Bunk, O., David, C. & Pfeiffer, F. High-Resolution Scanning X-ray Diffraction Microscopy. *Science* **321,** 379–382 (2008).

79. Yang, H., Rutte, R. N., Jones, L., Simson, M., Sagawa, R., Ryll, H., Huth, M., Pennycook, T. J., Green, M. L., Soltau, H., Kondo, Y., Davis, B. G. & Nellist, P. D. Simultaneous atomic-resolution electron ptychography and Z-contrast imaging of light and heavy elements in complex nanostructures. *Nature Communications* **7,** 12532 (2016).

80. Yang, H., MacLaren, I., Jones, L., Martinez, G. T., Simson, M., Huth, M., Ryll, H., Soltau, H., Sagawa, R., Kondo, Y., Ophus, C., Ercius, P., Jin, L., Kovács, A. & Nellist, P. D. Electron ptychographic phase imaging of light elements in crystalline materials using Wigner distribution deconvolution. *Ultramicroscopy* **180,** 173–179 (2017).

81. Yeh, L.-H., Dong, J., Zhong, J., Tian, L., Chen, M., Tang, G., Soltanolkotabi, M. & Waller, L. Experimental robustness of Fourier ptychography phase retrieval algorithms. *Optics Express* **23,** 33214 (2015).

82. Horstmeyer, R., Chung, J., Ou, X., Zheng, G. & Yang, C. Diffraction tomography with Fourier ptychography. *Optica* **3,** 827 (2016).

83. Spangenberg, D., Neethling, P., Rohwer, E., Brügmann, M. H. & Feurer, T. Time-domain ptychography. *Physical Review A - Atomic, Molecular, and Optical Physics* **91,** 021803 (2015).

84. Claus, D., Robinson, D. J., Chetwynd, D. G., Shuo, Y., Pike, W. T., De J Toriz Garcia, J. J. & Rodenburg, J. M. Dual wavelength optical metrology using ptychography. *Journal of Optics (United Kingdom)* **15,** 035702 (2013).

85. Gardner, D. F., Tanksalvala, M., Shanblatt, E. R., Zhang, X., Galloway, B. R., Porter, C. L., Karl, R., Bevis, C., Adams, D. E., Kapteyn, H. C., Murnane, M. M. & Mancini, G. F. Subwavelength coherent imaging of periodic samples using a 13.5 nm tabletop high-harmonic light source. *Nature Photonics* **11,** 259–263 (2017).

86. Humphry, M., Kraus, B., Hurst, A., Maiden, A. & Rodenburg, J. Ptychographic electron microscopy using high-angle dark-field scattering for sub-nanometre resolution imaging. *Nature Communications* **3,** 730 (2012).

87. Jiang, Y., Chen, Z., Han, Y., Deb, P., Gao, H., Xie, S., Purohit, P., Tate, M. W., Park, J., Gruner, S. M., Elser, V. & Muller, D. A. Electron ptychography of 2D materials to deep sub-ångström resolution. *Nature* **559,** 343–349 (2018).

88. Maiden, A. M., Rodenburg, J. M. & Humphry, M. J. Optical ptychography: a practical implementation with useful resolution. *Optics Letters* **35,** 2585 (2010).

89. Maiden, A. M., Humphry, M. J. & Rodenburg, J. M. Ptychographic transmission microscopy in three dimensions using a multi-slice approach. *Journal of the Optical Society of America A* **29,** 1606 (2012).

90. Godden, T. M., Suman, R., Humphry, M. J., Rodenburg, J. M. & Maiden, A. M. Ptychographic microscope for three-dimensional imaging. *Optics Express* **22,** 12513 (2014).

91. Holler, M., Guizar-Sicairos, M., Tsai, E. H., Dinapoli, R., Müller, E., Bunk, O., Raabe, J. & Aeppli, G. High-resolution non-destructive three-dimensional imaging of integrated circuits. *Nature* **543,** 402–406 (2017).

92. Guizar-Sicairos, M., Diaz, A., Holler, M., Lucas, M. S., Menzel, A., Wepf, R. A. & Bunk, O. Phase tomography from x-ray coherent diffractive imaging projections. *Optics Express* **19,** 21345 (2011).

93. Maiden, A. M. & Rodenburg, J. M. An improved ptychographical phase retrieval algorithm for diffractive imaging. *Ultramicroscopy* **109,** 1256–1262 (2009).

94. Maiden, A., Johnson, D. & Li, P. Further improvements to the ptychographical iterative engine. *Optica* **4,** 736 (2017).

95. Thibault, P., Dierolf, M., Bunk, O., Menzel, A. & Pfeiffer, F. Probe retrieval in ptychographic coherent diffractive imaging. *Ultramicroscopy* **109,** 338–343 (2009).

96. Yang, C., Qian, J., Schirotzek, A., Maia, F. & Marchesini, S. Iterative Algorithms for Ptychographic Phase Retrieval. *arXiv preprint arXiv: 1105.5628* (2011).

97. Kreutz-Delgado, K. The complex gradient operator and the CR-calculus. *arXiv preprint arXiv: 0906.4835* (2009).

98. Drexler, W. & Fujimoto, J. G. *Optical coherence tomography: technology and applications* (Springer Science & Business Media, 2008).

99. De Boer, J. F., Cense, B., Park, B. H., Pierce, M. C., Tearney, G. J. & Bouma, B. E. Improved signal-to-noise ratio in spectral-domain compared with time-domain optical coherence tomography. *Opt. Lett.* **28,** 2067–2069 (2003).

100. Leitgeb, R, Hitzenberger, C. K. & Fercher, A. F. Performance of fourier domain vs. time domain optical coherence tomography. *Opt. Express* **11,** 889–894 (2003).

101. Choma, M., Sarunic, M., Yang, C. & Izatt, J. Sensitivity advantage of swept source and Fourier domain optical coherence tomography. *Optics Express* **11,** 2183 (2003).

102. Akcay, C., Parrein, P. & Rolland, J. P. Estimation of longitudinal resolution in optical coherence imaging. *Appl. Opt.* **41,** 5256–5262 (2002).

103. Wojtkowski, M., Kowalczyk, A., Leitgeb, R. & Fercher, A. F. Full range complex spectral optical coherence tomography technique in eye imaging. *Optics Letters* **27,** 1415 (2002).

104. Witte, S, Baclayon, M, Peterman, E. J. G., Toonen, R. F. G., Mansvelder, H. D. & Groot, M. L. Single-shot two-dimensional full-range optical coherence tomography achieved by dispersion control. *Opt. Express* **17,** 11335–11349 (2009).

105. Webb, A. *Introduction to biomedical imaging* (Wiley-IEEE Press, 2003).

106. Ralston, T. S., Marks, D. L., Scott Carney, P & Boppart, S. A. Interferometric synthetic aperture microscopy. *Nature Physics* **3,** 129 (2007).

107. Liu, Y., Liang, Y., Mu, G. & Zhu, X. Deconvolution methods for image deblurring in optical coherence tomography. *J. Opt. Soc. Am. A* **26,** 72–77 (2009).

108. Liu, Y.-Z., South, F. A., Xu, Y., Carney, P. S. & Boppart, S. A. Computational optical coherence tomography. *Biomed. Opt. Express* **8,** 1549–1574 (2017).

109. Miao, J., Charalambous, P., Kirz, J. & Sayre, D. Extending the methodology of X-ray crystallography to allow imaging of micrometre-sized non-crystalline specimens. *Nature* **400,** 342–344 (1999).

110. Chapman, H. N. & Nugent, K. A. Coherent lensless X-ray imaging. *Nature Photonics* **4,** 833 (2010).

111. Gabor, D. A new microscopic principle. *Nature* **161,** 777–778 (1948).

112. Lee, M., Yaglidere, O. & Ozcan, A. Field-portable reflection and transmission microscopy based on lensless holography. *Biomed. Opt. Express* **2,** 2721–2730 (2011).

113. Yu, L. & Kim, M. K. Wavelength-scanning digital interference holography for tomographic three-dimensional imaging by use of the angular spectrum method. *Opt. Lett.* **30,** 2092–2094 (2005).

114. Sheoran, G., Dubey, S., Anand, A., Mehta, D. S. & Shakher, C. Swept-source digital holography to reconstruct tomographic images. *Opt. Lett.* **34,** 1879–1881 (2009).

115. Hillmann, D., Lührs, C., Bonin, T., Koch, P. & Hüttmann, G. Holoscopy-holographic optical coherence tomography. *Opt. Lett.* **36,** 2390–2392 (2011).

116. Hillmann, D., Koch, P., Lührs, C., Franke, G. & Hüttmann, G. Efficient holoscopy image reconstruction. *Optics Express* **20,** 21247 (2012).

117. Bell, R. *Introductory Fourier transform spectroscopy* (Elsevier, 2012).

118. Marks, D. L., Ralston, T. S., Boppart, S. A. & Carney, P. S. Inverse scattering for frequency-scanned full-field optical coherence tomography. *J. Opt. Soc. Am. A* **24,** 1034–1041 (2007).

119. Akcay, A. C., Rolland, J. P. & Eichenholz, J. M. Spectral shaping to improve the point spread function in optical coherence tomography. *Opt. Lett.* **28,** 1921–1923 (2003).

120. Drexler, W. Ultrahigh-resolution optical coherence tomography. *Journal of biomedical optics* **9,** 47–75 (2004).

121. Smith, E. D. J., Moore, S. C., Wada, N, Chujo, W & Sampson, D. D. Spectral domain interferometry for OCDR using non-Gaussian broad-band sources. *IEEE Photonics Technology Letters* **13,** 64–66 (2001).

122. Tripathi, R., Nassif, N., Nelson, J. S., Park, B. H. & de Boer, J. F. Spectral shaping for non-Gaussian source spectra in optical coherence tomography. *Opt. Lett.* **27,** 406–408 (2002).

123. Marks, D. L., Carney, P. S. & Boppart, S. A. Adaptive spectral apodization for sidelobe reduction in optical coherence tomography images. *Journal of Biomedical Optics* **9,** 1281–1287 (2004).

124. Gong, J., Liu, B., Kim, Y. L., Liu, Y., Li, X. & Backman, V. Optimal spectral reshaping for resolution improvement in optical coherence tomography. *Opt. Express* **14,** 5909–5915 (2006).

125. Hitzenberger, C. K., Baumgartner, A., Drexler, W. & Fercher, A. F. Dispersion effects in partial coherence interferometry: implications for intraocular ranging. *Journal of Biomedical Optics* **4,** 144–152 (1999).

126. Vabre, L, Dubois, A & Boccara, A. C. Thermal-light full-field optical coherence tomography. *Opt. Lett.* **27,** 530–532 (2002).

127. Fercher, A. F., Drexler, W, Hitzenberger, C. K. & Lasser, T. Optical coherence tomography - principles and applications. *Reports on Progress in Physics* **66,** 239–303 (2003).

128. Federici, A. & Dubois, A. Full-field optical coherence microscopy with optimized ultrahigh spatial resolution. *Opt. Lett.* **40,** 5347–5350 (2015).

129. Marks, D. L., Oldenburg, A. L., Reynolds, J. J. & Boppart, S. A. Autofocus algorithm for dispersion correction in optical coherence tomography. *Appl. Opt.* **42,** 3038–3046 (2003).

130. Wojtkowski, M., Srinivasan, V. J., Ko, T. H., Fujimoto, J. G., Kowalczyk, A. & Duker, J. S. Ultrahigh-resolution, high-speed, Fourier domain optical coherence tomography and methods for dispersion compensation. *Opt. Express* **12,** 2404–2422 (2004).

131. Hofer, B., Považay, B., Hermann, B., Unterhuber, A., Matz, G. & Drexler, W. Dispersion encoded full range frequency domain optical coherence tomography. *Opt. Express* **17,** 7–24 (2009).

132. Weiner, A. *Ultrafast optics* (John Wiley & Sons, 2011).

133. Born, M. & Wolf, E. in. 7th ed. Chap. 13 (Elsevier, 2011).

134. Tsai, E. H. R., Usov, I., Diaz, A., Menzel, A. & Guizar-Sicairos, M. X-ray ptychography with extended depth of field. *Optics Express* **24,** 29089 (2016).

135. Suzuki, A., Furutaku, S., Shimomura, K., Yamauchi, K., Kohmura, Y., Ishikawa, T. & Takahashi, Y. High-resolution multislice X-ray ptychography of extended thick objects. *Physical Review Letters* **112,** 053903 (2014).

136. Gao, S., Wang, P., Zhang, F., Martinez, G. T., Nellist, P. D., Pan, X. & Kirkland, A. I. Electron ptychographic microscopy for three-dimensional imaging. *Nature Communications* **8,** 163 (2017).

137. Holler, M., Diaz, A., Guizar-Sicairos, M., Karvinen, P., Färm, E., Härkönen, E., Ritala, M., Menzel, A., Raabe, J. & Bunk, O. X-ray ptychographic computed tomography at 16 nm isotropic 3D resolution. *Scientific Reports* **4,** 3857 (2014).

138. Helfen, L., Myagotin, A., Rack, A., Pernot, P., Mikulík, P., Di Michiel, M. & Baumbach, T. Synchrotron-radiation computed laminography for high-resolution three-dimensional imaging of flat devices. *physica status solidi (a)* **204,** 2760–2765 (2007).

139. Holler, M., Odstrcil, M., Guizar-Sicairos, M., Lebugle, M., Müller, E., Finizio, S., Tinti, G., David, C., Zusman, J., Unglaub, W., Bunk, O., Raabe, J., Levi, A. F. J. & Aeppli, G. Three-dimensional imaging of integrated circuits with macro- to nanoscale zoom. *Nature Electronics* **2,** 464–470 (2019).

140. Li, P. & Maiden, A. Multi-slice ptychographic tomography. *Scientific Reports* **8,** 2049 (2018).

141. Boppart, S. A., Bouma, B. E., Pitris, C., Southern, J. F., Brezinski, M. E. & Fujimoto, J. G. In vivo cellular optical coherence tomography imaging. *Nature Medicine* **4,** 861–865 (1998).

142. Wojtkowski, M., Bajraszewski, T., Targowski, P. & Kowalczyk, A. Real-time in vivo imaging by high-speed spectral optical coherence tomography. *Optics Letters* **28,** 1745 (2003).

143. Drexler, W., Liu, M., Kumar, A., Kamali, T., Unterhuber, A. & Leitgeb, R. A. Optical coherence tomography today: speed, contrast, and multimodality. *Journal of Biomedical Optics* **19,** 071412 (2014).

144. Fercher, A. F., Hitzenberger, C. K., Kamp, G. & El-Zaiat, S. Y. Measurement of intraocular distances by backscattering spectral interferometry. *Optics Communications* **117,** 43–48 (1995).

145. De Boer, J. F., Leitgeb, R. & Wojtkowski, M. Twenty-five years of optical coherence tomography: the paradigm shift in sensitivity and speed provided by Fourier domain OCT [Invited]. *Biomedical Optics Express* **8,** 3248 (2017).

146. Shemonski, N. D., South, F. A., Liu, Y. Z., Adie, S. G., Scott Carney, P. & Boppart, S. A. Computational high-resolution optical imaging of the living human retina. *Nature Photonics* **9,** 440–443 (2015).

147. Huang, X., Yan, H., Harder, R., Hwu, Y., Robinson, I. K. & Chu, Y. S. Optimization of overlap uniformness for ptychography. *Optics Express* **22,** 12634 (2014).

148. Rodenburg, J. M. & Bates, R. H. T. The theory of super-resolution electron microscopy via Wigner-distribution deconvolution. *Philosophical Transactions of the Royal Society of London. Series A: Physical and Engineering Sciences* **339,** 521–553 (1992).

149. Seaberg, M. D., Zhang, B., Gardner, D. F., Shanblatt, E. R., Murnane, M. M., Kapteyn, H. C. & Adams, D. E. Tabletop nanometer extreme ultraviolet imaging in an extended reflection mode using coherent Fresnel ptychography. *Optica* **1,** 39–44 (2014).

150. Loetgering, L., Du, M., Eikema, K. S. E. & Witte, S. zPIE: an autofocusing algorithm for ptychography. *Optics Letters* **45,** 2030 (2020).

151. Guizar-Sicairos, M., Thurman, S. T. & Fienup, J. R. Efficient subpixel image registration algorithms. *Optics Letters* **33,** 156 (2008).

152. Sarunic, M. V., Weinberg, S. & Izatt, J. A. Full-field swept-source phase microscopy. *Optics letters* **31,** 1462–1464 (2006).

153. Van Heel, M. Similarity measures between images. *Ultramicroscopy* **21,** 95–100 (1987).

154. Van Heel, M. & Schatz, M. Fourier shell correlation threshold criteria. *Journal of Structural Biology* **151,** 250–262 (2005).

155. Du, M., Loetgering, L., Eikema, K. S. E. & Witte, S. Ptychographic optical coherence tomography. *Opt. Lett.* **46,** 1337–1340 (2021).

156. Binding, J., Ben Arous, J., Léger, J.-F., Gigan, S., Boccara, C. & Bourdieu, L. Brain refractive index measured in vivo with high-NA defocus-corrected full-field OCT and consequences for two-photon microscopy. *Optics Express* **19,** 4833 (2011).

157. Jansen, G. S. M., Rudolf, D, Freisem, L, Eikema, K. S. E. & Witte, S. Spatially resolved Fourier transform spectroscopy in the extreme ultraviolet. *Optica* **3,** 1122–1125 (2016).

158. Du, M., Eikema, K. S. E. & Witte, S. Computational-imaging-based optical coherence tomography in time- and frequency-domain. *OSA Continuum* **2,** 3141 (2019).

159. Thibault, P. & Menzel, A. Reconstructing state mixtures from diffraction measurements. *Nature* **494,** 68–71 (2013).

160. Batey, D. J., Claus, D. & Rodenburg, J. M. Information multiplexing in ptychography. *Ultramicroscopy* **138,** 13–21 (2014).

161. Ewald, P. P. X-ray diffraction by finite and imperfect crystal lattices. *Proceedings of the Physical Society* **52,** 167–174 (1940).

162. Roberts, B. A. & Kak, A. C. Reflection mode diffraction tomography. *Ultrasonic Imaging* **7,** 300–320 (1985).

163. Chu, T. H. & Lee, K. Y. Wide Band Microwave Diffraction Tomography Under Born Approximation. *IEEE Transactions on Antennas and Propagation* **37,** 515–519 (1989).

164. Dandliker, R. & Weiss, K. Reconstruction of the three-dimensional refractive index from scattered waves. *Optics Communications* **1,** 323–328 (1970).

165. Lim, J., Lee, K., Jin, K. H., Shin, S., Lee, S., Park, Y. & Ye, J. C. Comparative study of iterative reconstruction algorithms for missing cone problems in optical diffraction tomography. *Optics Express* **23,** 16933 (2015).

166. *https://www.mathworks.com/help/images/exploring-slices-from-a-3-dimensional-mri-data-set.html#MRISliceExample-1*

167. Gattass, R. R. & Mazur, E. Femtosecond laser micromachining in transparent materials. *Nature Photonics* **2,** 219–225 (2008).

168. Schupp, R, Torretti, F, Meijer, R. A., Bayraktar, M, Scheers, J, Kurilovich, D, Bayerle, A, Eikema, K. S. E., Witte, S, Ubachs, W, Hoekstra, R & Versolato, O. O. Efficient Generation of Extreme Ultraviolet Light From Nd:YAG-Driven Microdroplet-Tin Plasma. *Physical Review Applied* **12,** 14010 (2019).

169. Rothhardt, J., Krebs, M., Hädrich, S., Demmler, S., Limpert, J. & Tünnermann, A. Absorption-limited and phase-matched high harmonic generation in the tight focusing regime. *New Journal of Physics* **16,** 033022 (2014).

170. Siegman, A. E. New developments in laser resonators. *Proc. SPIE* **1224,** 2–14 (1990).

171. Siegman, A. E. Defining, measuring, and optimizing laser beam quality. *Proc. SPIE* **1868,** 2–12 (1993).

172. Nemes, G. & Siegman, A. E. Measurement of all ten second-order moments of an astigmatic beam by the use of rotating simple astigmatic (anamorphic) optics. *Journal of the Optical Society of America A* **11,** 2257 (1994).

173. Padgett, M. & Bowman, R. Tweezers with a twist. *Nature Photonics* **5,** 343–348 (2011).

174. Rodrigo, J. A. & Alieva, T. Polymorphic beams and Nature inspired circuits for optical current. *Scientific Reports* **6,** 35341 (2016).

175. Rubinsztein-Dunlop, H. *et al.* Roadmap on structured light. *Journal of Optics (United Kingdom)* **19,** 013001 (2016).

176. Platt, B. C. & Shack, R. History and Principles of Shack-Hartmann Wavefront Sensing. *Journal of Refractive Surgery* **17,** S573–S577 (2001).

177. Freisem, L., Jansen, G. S. M., Rudolf, D., Eikema, K. S. E. & Witte, S. Spectrally resolved single-shot wavefront sensing of broadband high-harmonic sources. *Optics Express* **26,** 6860 (2018).

178. Gbur, G. *Singular Optics* 1st ed. (CRC Press, 2016).

179. Schnars, U., Falldorf, C., Watson, J. & Jüptner, W. in *Digital Holography and Wavefront Sensing* (Springer-Verlag Berlin Heidelberg, 2015).

180. Allen, L. J. & Oxley, M. P. Phase retrieval from series of images obtained by defocus variation. *Optics Communications* **199,** 65–75 (2001).

181. Loetgering, L., Froese, H., Wilhein, T. & Rose, M. Phase retrieval via propagation-based interferometry. *Physical Review A* **95,** 033819 (2017).

182. Rodenburg, J. M., Hurst, A. C., Cullis, A. G., Dobson, B. R., Pfeiffer, F, Bunk, O, David, C, Jefimovs, K & Johnson, I. Hard-X-Ray Lensless Imaging of Extended Objects. *Physical Review Letters* **98,** 034801 (2007).

183. Pfeiffer, F. X-ray ptychography. *Nature Photonics* **12,** 9–17 (2018).

184. Guizar-Sicairos, M., Johnson, I., Diaz, A., Holler, M., Karvinen, P., Stadler, H.-C., Dinapoli, R., Bunk, O. & Menzel, A. High-throughput ptychography using Eiger-scanning X-ray nano-imaging of extended regions. *Optics Express* **22,** 14859 (2014).

185. Vila-Comamala, J., Sakdinawat, A & Guizar-Sicairos, M. Characterization of x-ray phase vortices by ptychographic coherent diffractive imaging. *Optics Letters* **39,** 5281 (2014).

186. Rose, M., Senkbeil, T., von Gundlach, A. R., Stuhr, S., Rumancev, C., Dzhigaev, D., Besedin, I., Skopintsev, P., Loetgering, L., Viefhaus, J., Rosenhahn, A. & Vartanyants, I. A. Quantitative ptychographic bio-imaging in the water window. *Optics Express* **26,** 1237 (2018).

187. Loetgering, L., Rose, M., Keskinbora, K., Baluktsian, M., Dogan, G., Sanli, U., Bykova, I., Weigand, M., Schütz, G. & Wilhein, T. Correction of axial position uncertainty and systematic detector errors in ptychographic diffraction imaging. *Optical Engineering* **57,** 084106 (2018).

188. Enders, B., Dierolf, M., Cloetens, P., Stockmar, M., Pfeiffer, F. & Thibault, P. Ptychography with broad-bandwidth radiation. *Applied Physics Letters* **104,** 171104 (2014).

189. Esashi, Y., Liao, C.-T., Wang, B., Brooks, N., Dorney, K. M., Hernández-García, C., Kapteyn, H., Adams, D. & Murnane, M. Ptychographic amplitude and phase reconstruction of bichromatic vortex beams. *Optics Express* **26,** 34007 (2018).

190. Bastiaans, M. J. The Wigner distribution function applied to optical signals and systems. *Optics Communications* **25,** 26–30 (1978).

191. Bastiaans, M. J. Wigner distribution function and its application to first-order optics. *Journal of the Optical Society of America* **69,** 1710 (1979).

192. Bastiaans, M. J. Application of the Wigner distribution function in optics. *The Wigner Distribution—Theory and Applications in Signal Processing*, 375–426 (1997).

193. Cámara, A. & Bastiaans, M. Wigner Distribution Moments for Beam Characterization. *Mathematical Optics*, 13–51 (2012).

194. ISO 11146-1. Lasers and laser-related equipment — Test methods for laser beam widths, divergence angles and beam propagation ratios — Part 1: Stigmatic and simple astigmatic beams (2005).

195. ISO 11146-2. Lasers and laser-related equipment — Test methods for laser beam widths, divergence angles and beam propagation ratios — Part 2: General astigmatic beams (2005).

196. ISO 11146-3. Lasers and laser-related equipment — Test methods for laser beam widths, divergence angles and beam propagation ratios — Part 3: Intrinsic and geometrical laser beam classification, propagation and details of test methods (2004).

197. Martínez-Herrero, R., Mejías, P. M., Sánchez, M. & Neira, J. L. Third- and fourth-order parametric characterization of partially coherent beams propagating through ABCD optical systems. *Optical and Quantum Electronics* **24,** S1021–S1026 (1992).

198. Nemes, G. Intrinsic and geometrical beam classification, and the beam identification after measurement. *Proc. SPIE* **4932,** 624–636 (2003).

199. Letsch, A. & Giesen, A. Characterization of general astigmatic beams. *Proc. SPIE* **6101,** 610117 (2006).

200. Serna, J., Encinas-Sanz, F. & Nemes, G. Complete spatial characterization of a pulsed doughnut-type beam by use of spherical optics and a cylindrical lens. *J. Opt. Soc. Am. A* **18,** 1726–1733 (2001).

201. Siegman, A. E. *How to (Maybe) Measure Laser Beam Quality* in *Diode Pumped Solid State Lasers: Applications and Issues* (ed Dowley, M.) **17** (OSA, 1998).

202. Nemes, G. Correlation between geometrical and intrinsic classification of general astigmatic laser beams. *Proc. SPIE* **6101,** 610118 (2006).

203. Noll, R. J. Zernike polynomials and atmospheric turbulence. *Journal of the Optical Society of America* **66,** 207 (1976).

204. Stockmar, M., Cloetens, P., Zanette, I., Enders, B., Dierolf, M., Pfeiffer, F. & Thibault, P. Near-field ptychography: phase retrieval for inline holography using a structured illumination. *Scientific reports* **3,** 1927 (2013).

205. Loetgering, L., Rose, M., Treffer, D., Vartanyants, I. A., Rosenhahn, A. & Wilhein, T. Data compression strategies for ptychographic diffraction imaging. *Advanced Optical Technologies* **6,** 475–483 (2017).

206. Goodman, J. W. *Statistical Optics* 2nd (Wiley, New York, 2015).

207. Gawhary, O. E. On a propagation-invariant, orthogonal modal expansion on the unit disk: going beyond Nijboer-Zernike theory of aberrations. *Opt. Lett.* **40,** 2626–2629 (2015).

208. Bruzzone, A. A., Costa, H. L., Lonardo, P. M. & Lucca, D. A. Advances in engineered surfaces for functional performance. *CIRP Annals - Manufacturing Technology* **57,** 750–769 (2008).

209. Jacobs, T. D., Junge, T. & Pastewka, L. Quantitative characterization of surface topography using spectral analysis. *Surface Topography: Metrology and Properties* **5,** 013001 (2017).

210. Meyer, E., Hug, H. J. & Roland, B. *Scanning probe microscopy: the lab on a tip* (Springer-Verlag Berlin Heidelberg, 2004).

211. Vorburger, T. V. & Teague, E. C. Optical techniques for on-line measurement of surface topography. *Precision Engineering* **3,** 61–83 (1981).

212. Udupa, G., Singaperumal, M., Sirohi, R. S. & Kothiyal, M. P. Characterization of surface topography by confocal microscopy: I. Principles and the measurement system. *Measurement Science and Technology* **11,** 305–314 (2000).

213. Tiziani, H. J. Confocal principle for macro- and microscopic surface and defect analysis. *Optical Engineering* **39,** 32 (2000).

214. ISO 25178-709. Geometrical product specifications (GPS) — Surface texture: Areal — Part 607: Nominal characteristics of non-contact (confocal microscopy) instruments (2019).

215. Gobi, G., Ganesh, A. B., Radhakrishnan, T. K. & Sastikumar, D. An Optical Approach to Estimate the Surface Roughness of Metals. *J. Am. Sci* **3,** 49–53 (2007).

216. ISO 25178-2. Geometrical product specifications (GPS) — Surface texture: Areal —Part 2: Terms, definitions and surface texture parameters (2012).

217. Goodman, J. W. *Speckle Phenomena in Optics: Theory and Applications* (2007).

218. Maiden, A. M., Humphry, M. J., Zhang, F. & Rodenburg, J. M. Superresolution imaging via ptychography. *Journal of the Optical Society of America A* **28,** 604 (2011).

219. Fujii, H and Asakura, T. Effect of surface roughness on the statistical distribution of image speckle intensity. *Optics communications* **11,** 35–38 (1974).

220. Fujii, H., Asakura, T. & Shindo, Y. Measurement of surface roughness properties by using image speckle contrast. *J. Opt. Soc. Am.* **66,** 1217–1222 (1976).

221. Goodman, J. W. Statistical properties of laser speckle patterns. *Technical Report No. 2303-1* (1963).

222. Sprague, R. A. Surface Roughness Measurement Using White Light Speckle. *Applied Optics* **11,** 2811 (1972).

223. Elbaum, M., Greenebaum, M. & King, M. *A wavelength diversity technique for reduction of speckle size* 1972.

224. Parry, G. The scattering of polychromatic light from rough surfaces: first order statistics. *Optical and Quantum Electronics* **7,** 311–318 (1975).

225. Pedersen, H. M. On the contrast of polychromatic speckle patterns and its dependence on surface roughness. *Optica Acta* **22,** 15–24 (1975).

226. Pedersen, H. M. Second-order statistics of light diffracted from gaussian, rough surfaces with applications to the roughness dependence of speckles. *Optica Acta* **22,** 523–535 (1975).

227. Parry, G. in *Laser speckle and related phenomena* (ed Dainty, J. C.) 77–121 (1975).

228. Valent, E. & Silberberg, Y. Scatterer recognition via analysis of speckle patterns. *Optica* **5,** 204 (2018).

229. Dierolf, M., Thibault, P., Menzel, A., Kewish, C. M., Jefimovs, K., Schlichting, U., Von König, K., Bunk, O. & Pfeiffer, F. Ptychographic coherent diffractive imaging of weakly scattering specimens. *New Journal of Physics* **12,** 035017 (2010).

230. *Joseph Kirk (2021). Traveling Salesman Problem - Genetic Algorithm (https://www.mathworks.com/matlabcentral/fileexchange/13680-traveling-salesman-problem-genetic-algorithm), MATLAB Central File Exchange. Retrieved January 27, 2021.*

231. Guizar-Sicairos, M., Holler, M., Diaz, A., Vila-Comamala, J., Bunk, O. & Menzel, A. Role of the illumination spatial-frequency spectrum for ptychography. *Physical Review B - Condensed Matter and Materials Physics* **86,** 100103 (2012).

232. Saxton, W. O. & Baumeister, W. The correlation averaging of a regularly arranged bacterial cell envelope protein. *Journal of Microscopy* **127,** 127–138 (1982).

233. Harauz, George and van Heel, M. Exact filters for general geometry three dimensional reconstruction. *Optik (Stuttgart)* **73,** 146–156 (1986).

LIST OF PUBLICATIONS

This thesis is based on the following publications:

Chapter 3
Du, M., Eikema, K.S.E & Witte, S. Computational-imaging-based optical coherence tomography in time-and frequency-domain. *OSA Continuum* **2**, 3141-3152 (2019).

Chapter 4
Du, M., Loetgering, L., Eikema, K.S.E. & Witte, S. Ptychographic optical coherence tomography. *Optics Letters* **46**, 1337-1340 (2021).

Chapter 6
Du, M., Loetgering, L., Eikema, K.S.E. & Witte, S. Measuring laser beam quality, wavefronts, and lens aberrations using ptychography. *Optics Express* **28**, 5022-5034 (2020).

Other publications by the author:

Loetgering, L., Liu, X., De Beurs, A.C., Du, M., Kuijper, G., Eikema, K.S.E, & Witte, S. Tailoring spatial entropy in extreme ultraviolet focused beams for multispectral ptychography. *Optica* **8**, 130-138 (2021).

Loetgering, L., Du, M., Eikema, K.S.E., & Witte, S. zPIE: an autofocusing algorithm for ptychography. *Optics letters* **45**, 2030-2033 (2020).

Guo K., Du M., Osorio C.I., and Koenderink A.F. Broadband light scattering and photoluminescence enhancement from plasmonic vogel's golden spirals. *Laser Photonics Rev.* **11**, 1600235 (2017).

SUMMARY

In this thesis, the main research challenge boils down to extracting 3D spatial information of an object from 2D measurements using light. Our goal is to achieve depth-resolved tomographic imaging of transparent or semi-transparent 3D objects, and to perform topography characterization of rough surfaces. The essential tool we used is computational imaging, where depending on the experimental scheme, often indirect measurements are taken, and tailored algorithms are employed to perform image reconstructions. The computational imaging approach enables us to relax the hardware requirement of an imaging system, which is essential when using light in the EUV and x-ray regimes, where high-quality optics are not readily available. In this thesis, visible and infrared light sources are used, where computational imaging also offers several advantages. First of all, it often leads to a simple, flexible imaging system with low cost. In the case of a lensless configuration, where no lenses are involved in the final image-forming stage between the object and the detector, aberration-free image reconstructions can be obtained. More importantly, computational imaging provides quantitative reconstructions of scalar electric fields, enabling phase imaging, numerical refocus, as well as 3D imaging.

The first part of this thesis focuses on depth-resolved imaging. One important element that we used to achieve 3D imaging is broadband laser light. Inspired by optical coherence tomography, we take advantage of the short temporal coherence of broadband light. When light is back-scattered from a 3D object, the wavelength-dependent phase delay encodes the depth information. However, photoelectric detectors are only able to directly measure the intensity of a complex-valued electric field. Therefore, to obtain the 3D distribution of an object, the main task is to recover the lost phase information. The problem we try to solve can be simplified mathematically as $I = |\mathcal{P}\{E_o\}|^2$, where E_o denotes the electric field modified by an object, which is what we try to solve for. $\mathcal{P}$ represents a linear operator for free-space propagation, for example the Fourier transform or angular spectrum propagator, for which we know the mathematical expression and we know how to invert. I represents the intensity of the propagated electric field that we can measure. The non-linear operation, i.e. taking the absolute squared value, makes the inversion problem challenging.

In Chapter 3, the approach we take is to 'linearize' the problem by adding a reference and using interferometric detection. Thus the problem becomes $I = |E_f + \mathcal{P}\{E_o\}|^2 = \bar{I} + E_f^*\mathcal{P}\{E_o\} + c.c.$, where $\bar{I}$ is the autocorrelation term and $c.c$ denotes the complex conjugate term. Thanks to the interferometric detection, it is possible to filter out the linear term $E_1 = E_f^*\mathcal{P}\{E_o\}$, from which we obtain the solution $E_o = \mathcal{P}^{-1}\{E_f E_1\}$. Often plane waves are used as the reference, which can further simplify the solution. Note that in practice, this requires a precisely calibrated reference wave, which can be inconvenient or in some cases very challenging.

In Chapter 4, a different approach has been taken, namely phase retrieval, which uses iterative optimization algorithms to directly search for solutions to the non-linear inversion problem. Since it is a nondeterministic approach, it is generally not guaranteed a solution can be found. Phase retrieval often requires prior knowledge of the imaging object, which is used as constraints to limit the search space of the solution and steer the algorithm towards the correct solution. Among all phase retrieval methods, ptychography stands out as it offers fast, robust convergence to quantitative reconstructions without the need for prior knowledge. In ptychography, the problem is rearranged as $I = |\mathcal{P}\{PO\}|^2$, where the object modified electric field E_o is factorized as a product of the illumination (or often referred to as the probe) denoted by P, and the object function denoted by O. Ptychography is able to separate the illumination from the object function, and delivers complex-valued reconstruction of both simultaneously.

Once we solve the phase problem at each individual wavelength, 2D reconstructions at different wavelengths can be combined together to retrieve the depth information. Chapter 3 takes the conventional OCT approach where the interferometric detector sets a global phase reference for all the wavelengths, thus a Fourier transform from the frequency to the time domain reveals the depth distribution. Chapter 4 shows that it is possible to obtain depth information from polychromatic reconstructions without relying on an external reference. Given single-wavelength quantitative phase reconstructions, a synthetic reference signal can be selected from the object itself. This further simplifies the experimental arrangement and offers a step closer to possible implementation of depth-resolved imaging with broadband EUV sources.

Chapter 5 investigates the possibility of single-wavelength, single-view tomographic imaging using ptychography. Considering 3D weakly-scattering objects, we modify the forward model in ptychography using the first Born approximation. Reconstruction results based on simulated data show clear depth-separation, which may lead to a new direction of diffraction tomography.

In the second part of the thesis, we explore the application of computational imaging in optical metrology. Chapter 6 applies ptychography as a high-resolution wavefront sensing tool. Although originally intended for solving the phase problem in coherence diffractive imaging, ptychography produces quantitative reconstruction of the illumination beam as a 'byproduct'. This offers an excellent start for characterizing laser beam quality, wavefront and lens aberrations. We show that compared to existing metrology tools, e.g. the Shack-Hartmann sensor and conventional M^2 measurement devices, ptychography offers superior performance in terms of spatial resolution and flexibility. In Chapter 7, we apply computational imaging to characterize surface roughness. Both ptychography and computational OCT are used to directly image steel surfaces with a roughness parameter S_q comparable to, or larger than the optical wavelength, where we show that it is challenging to obtain quantitative reconstructions of rough surfaces with low-numerical-aperture systems. Apart from the direct imaging approach, we also explore the possibility of extracting surface roughness parameters from speckle measurements of rough surfaces. The relation between the visibility of polychromatic speckle patterns and the surface roughness is investigated, a generalized model is presented, and preliminary results are discussed.

SAMENVATTING

De primaire onderzoeksuitdaging van dit proefschrift is het achterhalen van 3D ruimtelijke informatie van een object door middel van 2D metingen met licht. Ons doel is om tomografische beelden te vormen van transparante of semi-transparante 3D objecten, waarin de structuur van het object transversaal en ook in de diepte wordt vastgesteld, én om de topografie van oneffen oppervlaktes te karakteriseren. Hiervoor maken we gebruik van *computationele beeldvorming*¸ waarbij met (in)directe metingen en afgestemde algoritmes beelden worden gevormd met behulp van computers. Door gebruik te maken van deze computationele beeldvorming kunnen de eisen voor de hardware van een beeldvormingssysteem versoepeld worden. Dit is essentieel wanneer gebruik wordt gemaakt van EUV of röntgenstraling, waarvoor optische componenten van hoge kwaliteit niet makkelijk verkrijgbaar zijn. In dit proefschrift wordt gebruik gemaakt van bronnen van zichtbaar en infrarood licht, waarbij computationele beeldvorming ook enkele voordelen biedt. Allereerst leidt het vaak tot een eenvoudig, flexibel, en relatief goedkoop beeldvormingssysteem. Maar, nog belangrijker is dat met computationele beeldvorming de scalaire elektrische velden worden gereconstrueerd, wat fasebeeldvorming, numeriek herfocusseren, en 3D-beeldvorming mogelijk maakt.

Het eerste deel van dit proefschrift richt zich op beeldvorming door de diepte van een object heen. Een belangrijk element dat we hebben gebruikt om 3D-beeldvorming te realiseren, is breedbandig laserlicht. Geïnspireerd door optische coherentietomografie maken we gebruik van de korte temporele coherentie van breedbandig licht. Wanneer licht wordt terugverstrooid door een 3D-object, bevat de golflengte afhankelijke fasevertraging de diepte-informatie van het object. Echter zijn foto-elektrisch detectoren alleen in staat om de intensiteit van een elektrisch veld te meten en is de fase dus onbekend. Daarom is de voornaamste taak voor het verkrijgen van de 3D-distributie van een object het reconstrueren van de "verloren" fase-informatie. Het probleem dat we proberen op te lossen kan wiskundig worden vereenvoudigd in de vorm $I = |\mathcal{P}\{E_o\}|^2$, met E_o het te achterhalen elektrisch veld dat is aangepast door een object. P vertegenwoordigd een lineaire operator voor voortplanting van een elektrisch veld in de vrije ruimte, bijvoorbeeld de Fouriertransformatie of hoekspectrum propagatoren waarvan we de wiskundige uitdrukking kennen en weten hoe we ze moeten inverteren. I vertegenwoordigt de intensiteit van het meetbare, gepropageerde elektrisch veld. De niet-lineaire operatie, d.w.z. het nemen van de absolute waarde in het kwadraat, maakt dit inversieprobleem uitdagend.

In hoofdstuk 3 'lineariseren' we het probleem door gebruik te maken van interferometrische detectie met een referentie. In dat geval kan het probleem worden herschreven als $I = |E_f + \mathcal{P}\{E_o\}|^2 = \bar{I} + E_f^* \mathcal{P}\{E_o\} + c.c.$, met $\bar{I}$ de autocorrelatie term en c.c. de complex-geconjugeerde term. Dankzij de interferometrische detectie kan de lineaire term $E_1 = E_f^* \mathcal{P}\{E_o\}$ eruit gefilterd worden en verkrijgen we de oplossing $E_o = \mathcal{P}^{-1}\{E_f E_1\}$. Vaak worden vlakke golven als referentie gebruikt, dit kan de oplossing verder vereenvoudigen. In de praktijk is hier echter een exact

gekalibreerde referentiegolf voor nodig, wat onhandig en in sommige gevallen erg uitdagend kan zijn.

In Hoofdstuk 4 is gekozen voor een andere benadering, namelijk *fasereconstructie*, waarbij iteratieve optimalisatie-algoritmes worden gebruikt om rechtstreeks naar de oplossingen te zoeken van het niet-lineaire inversieprobleem. Omdat het een niet-deterministische benadering is, is het over het algemeen niet gegarandeerd dat er een oplossing kan worden gevonden. Fasereconstructie vereist vaak voorkennis van het object, dat wordt gebruikt als begrenzing van de zoekruimte van de oplossing en stuurt het algoritme daarmee naar de juiste oplossing. Tussen alle fasereconstructiemethodes valt *ptychography* op, omdat het, zonder voorkennis van het object, snelle en robuuste convergentie naar kwantitatieve oplossingen biedt. In ptychography wordt het probleem herschikt als $I = |\mathcal{P}\{PO\}|^2$, waarbij het object-gemodificeerde elektrische veld E_o wordt ontbonden als een product van de belichting aangeduid met P, en de objectfunctie aangegeven door O. Ptychography is in staat om de belichting te scheiden van de objectfunctie, en levert reconstructies van de intensiteit en fase van beide tegelijk.

Zodra we het faseprobleem bij elke individuele golflengte hebben opgelost kunnen 2D-reconstructies met de verschillende golflengtes worden gecombineerd om de diepte informatie te achterhalen. Hoofdstuk 3 neemt de conventionele OCT-benadering, waarbij door middel van interferometrische detectie een globale fasereferentie voor alle golflengten wordt gezet. Zodoende onthult een Fourier-transformatie van het frequentiedomein naar het tijdsdomein de diepte distributie van het object. Hoofdstuk 4 laat zien dat het ook mogelijk is om diepte-informatie te verkrijgen van polychromatische reconstructies zonder een externe referentie. Gegeven monochromatische kwantitatieve fasereconstructies, kan een synthetisch referentiesignaal worden geselecteerd uit het object zelf. Dit vereenvoudigt de experimentele opstelling verder en brengt ons een stap dichter bij een implementatie van diepte-beeldvorming met breedbandige EUV-bronnen.

Hoofdstuk 5 onderzoekt de mogelijkheid van tomografische beeldvorming met een enkele golflengte en een enkele weergave met behulp van ptychography. Uitgaande van zwak verstrooiende 3D objecten modificeren we het voorwaartse model in ptychography met behulp van de eerste Born-benadering, Reconstructieresultaten op basis van gesimuleerde data laten een duidelijke diepte-scheiding zien, wat kan leiden tot een nieuwe richting van diffractietomografie.

In het tweede deel van het proefschrift onderzoeken we de toepassing van computationele beeldvorming in optische metrologie. Hoofdstuk 6 past ptychography toe als een hoge resolutie golffront-detectietool. Hoewel oorspronkelijk bedoeld om het faseprobleem op te lossen in coherentie-diffractie beeldvorming, produceert ptychography kwantitatieve reconstructie van de verlichtingsstraal als 'bijproduct'. Dit biedt een uitstekende start voor het karakteriseren van laserstraal kwaliteit, en golffront en lens aberraties. Wij laten zien dat in vergelijking met bestaande metrologie methodes, b.v. de Shack-Hartmann-sensor en conventionele M2-meetapparatuur, ptychography superieure prestatie biedt in termen van ruimtelijke resolutie en flexibiliteit. In hoofdstuk 7 passen we computationele beeldvorming toe om oppervlakteruwheid te karakteriseren. Zowel ptychography als computationele OCT worden gebruikt om beelden te vormen van stalen oppervlaktes met een ruwheid parameter S_q vergelijkbaar met, of groter dan de optische

golflengte. We laten zien dat het een uitdaging is om kwantitatieve reconstructies van ruwe oppervlakken te verkrijgen wanneer systemen met een laag numeriek apertuur worden gebruikt. Afgezien van de directe beeldvormingsaanpak, onderzoeken wij ook de mogelijkheid om parameters voor oppervlakteruwheid uit gemeten spikkelpatronen te halen. De relatie tussen de zichtbaarheid van polychromatische spikkelpatronen en de oppervlakteruwheid wordt onderzocht, een gegeneraliseerd model wordt gepresenteerd, en voorlopige resultaten worden besproken.

ACKNOWLEDGMENTS

The PhD student journey has finally come to an end with the completion of this thesis. I would like to give my sincere acknowledgments to people who helped and accompanied me through this journey.

Stefan, my supervisor, I feel very lucky working in your group under your supervision. Thank you for all the discussions, feedback, encouragement, and trust. I truly appreciate the bright, positive attitude and energy you bring to work and to the group. Kjeld, thank you for setting up the group with Stefan. Your guidance in the beginning was very valuable. I enjoyed your humorous, witty way of explaining things and thank you for all the feedback.

Lars L., before you started at ARCNL, I was working alone, and you came holding a bright torch marked ptychography. Working together was not easy in the beginning, but I am glad we could work it out and gain understanding for and trust in each other. Thank you for all the discussions from which I learned a ton. Your passion for research and your persistence inspire me. Now you have left ARCNL, but I do not feel like I lost a collaborator nor a friend.

Nik, I want to thank you for the help in the Lab. Whenever I needed something for my setup, I could always count on you and quickly get a perfect solution. Jorijn, thank you for making 'The bright side of life' and 'Vocational Guidance' software for our experiments. I appreciated all the discussions, quick responses, and support.

Dirk, you always think out of the box and it was really fun to have you around. Thank you for introducing me to the Nerd night event, letting me experience sailing, and for inviting me to fun parties. I also very much enjoyed coding together during the pandemic. I learned a lot and definitely admire your Python skills.

Zeudi and Amelie, we naturally formed some kind of EUV-GENIM girl group, although every now and then I would feel left out, maybe because I didn't work on high-power lasers. Guess what, I am catching up now ;). Jan, we shared the same lab in both the old and new buildings. Yelling across the safety curtain to each other had become the norm. Thank you for all the small help in the lab. Guido, thank you for sharing the GPU/computer with me during your internship. Although it was a short period of time, I appreciate the collaboration as well as the friendship.

Tiago, Lars F., Aneta, Faisal and Thijs, although you have already left the group for a while, the memories we had in the old ARCNL offices, meeting rooms, the lab, and the canteen are always something that makes me happy to look back on.

I would like to thank Ale, Hao, Kevin, Anne, Denis, Matthijs, Patrick, as well as all the former and current members of the EUV-GENIM group, for creating a wonderful working atmosphere, for all the group lunches and coffee breaks.

The PhD was a whole package, from the research work to the daily life that wrapped around it, all the ups and downs, challenges and survival. Many friends

popped out the package unexpected, to whom I would like to express my sincere gratitude.

Vanessa, I used to drop by your office in the old building whenever I wanted to take a short break. In the new building we got to share the most awesome office. Thank you for all the fun and bizarre coffee break chats. I also had a great time planning fun activities with you in the PV. Outside ARCNL, you became my Italian sis that I feel like hanging out all the time. Thank you for asking me to be your paranymph and for being mine.

Ale A, you are literally the person I have known the longest in Amsterdam. You became the senior whose footsteps I coincidentally followed, from the internship in AMOLF to the PhD with Stefan. The funny part is that I became the only person in our dutch class who could understand whatever you were trying to say, a mixture of English and Dutch plus your Italian accent ;). I am really happy to have you around and have you as a close friend.

Görsel and Victor, our trip to Greece was amazing for me. Driving around in AVTs, delicious food, ouzo and raki, a lot of "sun's cream" (according to Görsel), and a lot of fun. Stephen, John and Lianjia, our roadtrip to California came at the very right moment, just before the pandemic hit. There are many fun and incredible memories, being attacked by a sand tornado in Death valley was definitely a once-in-a-lifetime experience. Stephen, you are such a fun character and a game sabotager. I very much appreciate having you as my foosball partner and a trustworthy friend. John, a conversation with you is never boring and thank you for your awesomeness. Zoey and Neha, thank you for being sweet friends. Fengchun, my Amazing Oriental supermarket buddy. Ruben, the feuerzangenbowle was awesome. Reinout, thank you for being unique and amazing.

Thanks to a broad range of ARCNL social activities: the foosball tournament, borrels, potlocks, pub quizzes, and outings, I had a lot of fun together with ARCNLers: Cristina, Najmeh, Robbert, Bruno, Vasco, Perry, Ale T., Fiona, Felix, Lucas, Filippo, Camila, Daan, Zazo, Thomas, Zoi, Christos, Sylvianne, Maarten, Marjan and Joost.

Jin, through the years, many Chinese friends have gone back to china, or drifted away. You stayed, your friendship stayed. Thank you for all the fun and sharing.

Maaike, mijn Nederlands docent. Nederlands leren was zo moeilijk voor mij in het begin. Ik kon geen manier vinden die bij mij paste. Maar dankzij jou heb ik niet alleen van de taal leren genieten, maar ook van de nederlandse cultuur, geschiedenis, en zelfs de politiek.

Randy, if it were not because of you, this whole Amsterdam life would not exist. We have accompanied each other for the whole Master and PhD journey. Thank you for everything. I would like to include our cats, Nacho and Huihui, who have made the pandemic life a lot easier for me.

Lastly, I would like to thank my parents and my family in China. It is always a difficult choice for me to be away from everyone. Thank you for understanding and encouraging me for pursuing what I want. You are always my strongest support.